AD A115724

NAVAL AIR ENGINEERING CENTER

REPORT NAEC-92-157

LAKEHURST, N.J.
08733

AEROSTRUCTURE NONDESTRUCTIVE EVALUATION
BY THERMAL FIELD DETECTION
PHASE I: FUNDAMENTAL INFORMATION AND
BASIC TECHNIQUE DEVELOPMENT

Advanced Technology Office
Support Equipment Engineering Department
Naval Air Engineering Center
Lakehurst, New Jersey 08733

25 MAY 1982

Final Report
AIRTASK A3400000/051B/8F41461406

DTIC
SELECTED
JUN 18 1982
H

Prepared for

Commander, Naval Air Systems Command
AIR-340E
Washington, D.C. 20361

82 06 18 004

Prepared by: _____
Dr. A. ....
Villanova University

Reviewed by: _____
A.V. .... , P.E.
Advanced Technology Office

Approved by: _____
....
Superintendent, Support Equipment Engineering
Department

NOTICE

REPORT DOCUMENTATION PAGE		READ INSTRUCTIONS BEFORE COMPLETING FORM
1. REPORT NUMBER NAEC-92-157	2. GOVT ACCESSION NO. AD-A115 724	3. RECIPIENT'S CATALOG NUMBER
4. TITLE (and Subtitle) AEROSTRUCTURE NDE BY THERMAL FIELD DETECTION PHASE I - FUNDAMENTAL INFORMATION AND BASIC TECHNIQUE DEVELOPMENT		5. TYPE OF REPORT & PERIOD COVERED TECHNICAL
		6. PERFORMING ORG. REPORT NUMBER
7. AUTHOR(s) P.V. McLAUGHLIN D.N. KOERT E.V. McASSEY J.M. SPITZER V.R. EMANY		8. CONTRACT OR GRANT NUMBER(s) N68335-79-C-1084
9. PERFORMING ORGANIZATION NAME AND ADDRESS VILLANOVA UNIVERSITY VILLANOVA, PA 19085		10. PROGRAM ELEMENT, PROJECT, TASK AREA & WORK UNIT NUMBERS
11. CONTROLLING OFFICE NAME AND ADDRESS NAVAL AIR SYSTEMS COMMAND WASHINGTON, DC 20361		12. REPORT DATE 25 MAY 1982
		13. NUMBER OF PAGES 122
14. MONITORING AGENCY NAME & ADDRESS(if different from Controlling Office) NAVAL AIR ENGINEERING CENTER SUPPORT EQUIPMENT ENGINEERING DEPT. LAKEHURST, NJ 08733		15. SECURITY CLASS. (of this report) UNCLAS
		15a. DECLASSIFICATION/DOWNGRADING SCHEDULE

16. DISTRIBUTION STATEMENT (of this Report)

APPROVED FOR PUBLIC RELEASE; DISTRIBUTION UNLIMITED

17. DISTRIBUTION STATEMENT (of the abstract entered in Block 20, if different from Report)

DTIC
ELECTE
JUN 1 8 1982
S   D
H

18. SUPPLEMENTARY NOTES

19. KEY WORDS (Continue on reverse side if necessary and identify by block number)

NONDESTRUCTIVE TESTING
COMPOSITE MATERIALS
THERMOGRAPHICS

20. ABSTRACT (Continue on reverse side if necessary and identify by block number)

This report describes the results of efforts to evaluate and develop methods of flaw detection in laminated fiber composite aerovehicle structures using infrared radiation detection techniques.

While not exhibiting the quantitative detection capabilities of other nondestructive evaluation (NDE) methods such as ultrasonics or neutron radiography, infrared thermography promises to provide a rapid method of damage detection in large structural surfaces. Two methods are described:

externally applied thermal field (EATF) flaw detection where surface "hot spots" due to subsurface flaws are created by heating with a radiant heat source; and stress-generated thermal field (SGTF) flaw detection where "hot spots" in viscoelastic composites are created at stress concentrations near structural flaws during high frequency, low magnitude cyclic loading.

Analytical and experimental studies were performed on 8- to 32-ply graphite/epoxy laminates and 8- to 16-ply S2-glass/epoxy laminates containing delaminations and partial through-holes to evaluate and develop EATF thermography. Results show that the conduction method of heat application is unsatisfactory for NDE purposes, and that a radiant energy source in excess of one solar constant will be required for best results. Flaws are detectable by this method up to 7/8 through the thickness of 32 ply graphite/epoxy and 16 ply S2-glass/epoxy laminates, and it does not appear that limits of flaw detection have yet been found. Surface finish (paint thickness, abrasions, and soil) have been found to affect results in certain cases, and methods of eliminating their undesirable effects are presented.

SGTF evaluation was conducted on both graphite/epoxy and S2-glass/epoxy laminates using a closely coordinated program of analysis and experiment. A semi-empirical method of determining heat generated in composites under cyclic loading has been developed, and results indicate that the magnitude of heat generated by viscoelastic material behavior may be marginal for SGTF flaw detection. Heat generated by frictional rubbing of crack or delamination surfaces has been shown to be several orders of magnitude larger than heat due to material viscoelasticity, and ultrasonic excitation methods suggested by other researchers may prove to be the most fruitful SGTF technique.

PREFACE

Accession For

NTIS GRA&I	☑
DTIC TAB	☐
Unannounced	☐
Justification	

By

Distribution/

Availability Codes

Dist	Avail and/or Special
A	

DTIC COPY INSPECTED

1

This page left blank
intentionally.

TABLE OF CONTENTS

LIST OF ILLUSTRATIONS

LIST OF ILLUSTRATIONS (CONT'D)

LIST OF ILLUSTRATIONS (CONT'D)

LIST OF TABLES

This page left blank
intentionally.

I. INTRODUCTION

A. One of the important missions of aerovehicle ground support personnel is to locate structural damage sites or flaws which, if not repaired, would in time lead to structural failure. Several nondestructive evaluation (NDE) methods are currently available or are under development for this purpose; among them are X-ray, neutron radiography, sonic or ultrasonic transmission or reflection, eddy current, etc. Each of these methods currently requires sophisticated equipment and highly skilled technicians for operation and data interpretation. Several methods (for example, C-scan) are not at this time suited for examining large areas of aircraft components, and other methods also have their limitations.

B. The use of fiber composite materials in present and future generation Navy aircraft requires that NDE techniques be developed to handle aero-structures made of composites as well as conventional metals such as aluminum and titanium. This poses specific problems, since composite structures fail in a different manner than metal structures. For example, impact damage to composite skins may consist of delaminations between plies, or subsurface shattering of the composite laminate; and both generally occur without visible damage to the top surface.

C. A relatively new nondestructive evaluation method has undergone extensive examination at Villanova University laboratories following the initial feasibility study presented in reference (a)*. This method consists of using an infrared camera to identify perturbations in structural surface temperatures that may be caused by the presence of a defect or damage zone. The surface temperature differences can be caused by applying heat externally with a radiant heat source or hot air heat gun (externally applied thermal field (EATF)) or by applying multiple cycles of loading to a part and allowing viscoelastic behavior or internal friction to cause "hot spots" in the vicinity of stress concentrations caused by flaws (stress generated thermal field (SGTF)). These studies have shown that NDE by thermal detection can be used for both composite and metal structures, and has the potential for large surface area examinations using ground support personnel who are not highly trained.

---

*Please see the list of references presented on page 56 of this report.

D. A closely coordinated analytical/experimental program was conducted
to evaluate thermography as an NDE tool for Navy aircraft. For the ex-
perimental portion of the program, temperature gradients were induced in
flawed specimens of graphite/epoxy, S2-glass/epoxy, Kevlar/epoxy and
aluminum by applying heat externally (EATF) or by stress-cycling (SGTF).
The resulting transient surface temperatures were monitored by an AGA
Thermovision System 680/102B infrared camera with both black and white
and color isotherm video readout. The color television screen, which was
used for the majority of the studies, breaks a given range of temperature
down into ten subranges, and shows each 1/10 of the total temperature
range as a different color. For example, a $10^{\circ}C$ gradient from $20^{\circ}C$ to
$30^{\circ}C$ would show up on the color screen at $10^{\circ}C$ sensitivity as (see Table
1):

TEMPERATURE ($^{\circ}C$)	COLOR	TEMPERATURE ($^{\circ}C$)	COLOR
Above 29	White	23-24	Light Blue
28-29	Yellow	22-23	Green
27-28	Orange	21-22	Blue Green
26-27	Red	20-21	Dark Blue
25-26	Lavender	Below 20	Black
24-25	Purple		

As a result, borders between colors represent isotherms (for example: the
border between orange and red indicates surface temperatures of $27^{\circ}C$).
Perturbations in otherwise smooth isotherms, or "hot spots" (concentric
closed isotherms), indicate flaws interrupting otherwise uniform heat flow
or uniform temperature fields. Figures 1, 5, 9, and 33 are typical
examples. Exact temperatures are not necessary for identifying defects by
perturbed isotherms, only a temperature difference from the surrounding
region need be identified.

E. This report first describes the heat transfer analysis which was
used to analytically predict specimen surface temperatures, then presents
results of studies to evaluate surface finish effects, EATF thermal field
application methods, and EATF flaw detection capabilities. Next, the SGTF
heat generation analysis and test program is described, and a feasibility
assessment of SGTF methods (including ultrasonics as a heat generation tool)
is made. Conclusions are presented for both EATF and SGTF methods, and
recommendations are made for work necessary to develop thermographic NDT
into a workable Navy aerostructure test method.

II. EXTERNALLY APPLIED THERMAL FIELD METHOD

A. __OBJECTIVE AND OUTLINE OF THE EATF STUDY__. The externally applied
thermal field research had as its objectives to develop and evaluate heat
application techniques, to generate a data base for sizes and types of
flaws that can be detected by EATF techniques, to make a determination of
the effects of surface finish, and to present preliminary conclusions con-
cerning equipment procedures. In order to accomplish these objectives, it
was necessary to develop a numerical heat transfer analysis procedure and
codify it on the digital computer. This heat transfer analysis is briefly
described in the next paragraph. It is followed by the surface finish
effects results, including evaluation of thickness and color of Navy
aviation paint on aluminum and epoxy matrix composites, and the effects of
abrasions and foreign substances on thermovideograph infrared camera out-
put. Next, thermal field application methods are discussed, and the ad-
vantages and disadvantages of a heat gun, heat lamp, local strip heaters,
and radiant heat sources are presented. Finally, an evaluation of flaw
detection capabilities for graphite/epoxy and glass/epoxy composite lami-
nates is made, including size, type, and location limits to the EATF
technique.

B. __HEAT TRANSFER ANALYSIS__. Analytical studies were required to support
the experimental phases of the present study. In particular, a multi-
dimensional transient computer program was developed to calculate the
transient thermal response of samples exposed to both externally applied
and stress generated thermal fields. The transient thermal response pro-
gram was developed using a finite difference model. In this model, the
sample is divided into a series of isothermal nodes. The transient response
of the ith node is given by the following expression:

$$T_i' = \left\{ \frac{m_c c_i T_i}{\Delta\theta} - \sum_{j=1}^{M} k_{ji} T_i + Q_i + \sum_{j=1}^{M} k_{ji} T_j \right\} / \frac{(m_i c_i)}{\Delta\theta}$$

where:

T'_i = temperature of ith node at end of time step $\Delta\theta$

T_i = temperature of ith node at the beginning of time step

Q_i = heat dissipated in the ith node

m_i = mass of ith node

c_i = specific heat of ith node

k_{ji} = thermal coupling between j^{th} and i^{th} node

In this procedure, the convective heat transfer to the ambient environment is included as a thermal coupling to a known temperature. The above equation is solved for each node at each time step from the initial time to the final time. The program adjusts the time step used in the calculation to insure that stability is maintained.

C. EVALUATION OF SURFACE FINISH EFFECTS

1. NAVAL AVIATION PAINT ON ALUMINUM

a. The Naval Air Engineering Center (NAVAIRENGCEN) provided aluminum samples with Navy aviation paint for the first phase of the surface finish evaluation. The samples are 10 cm. x 30.5 cm. aluminum substrates which were painted, one-half one color and one-half another. Since the purpose of the test was surface finish, no defects were put into the aluminum. Table 2 presents the various paint finishes examined. All the finishes were glossy polyurethane paint which will be used on all Navy aircraft in the future. Each sample was suspended vertically and heated with a hot-air gun. After being heated uniformly, the sample was allowed to cool by free convection and infrared thermovideograph pictures were taken. To check the effect of reflections from external sources, a 60-watt incandescent bulb was positioned 1.2 metres from the sample and at an angle of approximately 15 degrees from the camera optical axis.

b. The surface finish tests yielded a number of interesting results. Figure 1 presents the results for Sample A which was a black/white sample. Figure 1a shows the sample in the hot condition. The light color on the left is the black finish, which is hotter than the white portion. The sensitivity is set at 20°C from black to white. The unevenness along the interface between the color is attributed to paint thickness variation. Figure 1b shows the same sample but at a later time so that the sample is cooler than in Figure 1a. The sensitivity for this figure is 5°C.

12

Figure 1c shows Sample A under the influence of the light bulb, whose image appears in the upper part of the figure.

    c. Figure 2 presents results for Sample C which was white/orange. In Figure 2a, the effect of color and paint thickness can be seen. The nonuniform pattern can be attributed to different emissivities or uneven paint thickness. Figure 3a shows a similar pattern for a white/white sample (Sample E). Since the white/white sample has uniform emissivity, it would appear that the unevenness in Figures 2a and 3a is due to paint thickness variations. This is reinforced by the fact that the horizontal streaking patterns are similar. In Figure 1b, the effect of emissivity is more obvious because the sample is of uniform intensity but slightly different shading.

    d. The effect of emissivity differences between the different color finishes would be to raise or lower the local temperature and, therefore, change the shade of the picture. In general, emissivity is independent of color and depends upon the chemical composition of the paint. However, the shading differences in Figure 1b are equivalent to only $1^{\circ}C$ to $2^{\circ}C$, which could be related to slight color effects. Differences in paint thickness, on the other hand, would cause local hot spots due to the thermal resistance of the paint. These hot spots would tend to follow thickness variations rather than color changes.

    e. The effect of the light bulb can be seen in Figures 1c, 2b, and 3b. In all cases, the effect is very pronounced and would overshadow all other inputs. The sample surface which is glossy tends to reflect the heat of external sources. Since the finish used by Navy aircraft will be glossy, the technician using an infrared camera for NDT will be required to reduce the background of high energy external sources. Lower energy or more diffuse sources such as a hot runway are not expected to be a problem.

  2. NAVY AVIATION PAINT ON EPOXY MATRIX COMPOSITES

    a. The appearance of streaks in infrared camera pictures due to uneven paint thickness on aluminum samples led to the concern that paint thickness variations might be picked up by Navy technicians as structural flaws in composite aircraft during inspection. The polymeric Navy aviation paint has a relatively low conductivity, as do all plastics, while

the aluminum sample has a very high conductivity. It was reasoned that the streaks or hot spots on painted aluminum were caused by heat being conducted away from the surface of thinly painted regions by the aluminum, while the thicker paint regions remained hotter due to the larger thickness of low conductivity material. If this were true, then the spotting or streaking seen on painted aluminum would not be seen on painted epoxy matrix composites, since the conductivity of the paint and the transverse (through-the-thickness) conductivities of the composites are nearly equal.

b. To test this hypothesis and to see if paint thickness variations on composite materials could result in hot spots similar to those generated by structural flaws, 12 plate samples (6 each of unidirectional graphite/epoxy and Kevlar 49/epoxy) of epoxy matrix composites, each approximately 6 cm wide x 28 cm long x 0.2 cm thick, were sent to NAVAIRENGCEN facilities where they were unevenly painted with black, white, and orange Navy aviation paint. Single thicknesses and double thicknesses of the paints were applied side-by-side and on top of one another according to the scheme shown in Table 3. Each sample was photographed at room temperature and at an elevated temperature after being heated by a radiant heat source. Like the painted aluminum samples, the painted composite samples, as expected, exhibited an infrared response which varied with color due to paint pigment emissivity differences. However, also as expected, the large paint thickness variations did not appear to be detected by the infrared camera.

c. Figure 4 shows infrared camera thermovideographs of graphite/epoxy (sample Gr-A) and Kevlar/epoxy (sample K-A) plates with single and double thicknesses of white paint. Both the graphite and Kevlar samples show vertically uniform temperature distribution in the region of the change from single to double paint thickness. Figure 5 shows thermovideographs for single adjacent (nonuniform) coats of white and black paints. There is no discernable difference in heat emission of the two paints at room temperature (Figure 5a). At elevated temperatures created by heating with a radiant heat source, however, there is considerable difference in Thermovision output between the black and white paints, with the black paint appearing as much as $2^{\circ}C$ hotter than the white paint (Figure 5b-c). There is not any evidence, however, of spotting or streaking due

14

to uneven paint thicknesses. (Spots in Figure 5b are caused by uneven heat distribution-the spotting is not reproducible.). Figure 6 shows similar results for orange/white paint combinations. Note that the emissivity effects due to color are not as evident between the orange and white paints (a few tenths of a degree C) as they are between black and white paints. Figure 7 presents thermovideographs of one (uneven) coat of white paint on Kevlar/and graphite/epoxy samples. Note that streaks or spots do not exist due to uneven paint thicknesses.

3. ABRADED PAINTED SURFACES

   a. During a preliminary study (reference (a)), it was observed that dull or non-reflecting areas in an otherwise shiny surface could be identified in the infrared camera video picture. Navy aircraft are likely to receive non-damaging surface abrasions from support or flight personnel or as the result of a mission, etc. It was therefore deemed important to determine the effect of abrasions on infrared camera video readout. The graphite/epoxy with a single coat of white paint (sample Gr-D) was first cleaned, then abraded on two 2.5 cm square areas with No. 120 grit sandpaper. The abrasions were complete; no gloss was left inside the designated areas, but the paint was not penetrated through to the graphite/epoxy substrate.

   b. Thermovideographs of the abraded surface are shown in Figure 8. At room temperature (Figure 8a), the abrasions appear slightly cooler (about $0.2^{\circ}C$) than the surrounding glossy surface. When heated one minute by a radiant heat source and allowed to cool for 30 seconds, there is no visible difference between abraded and glossy painted surfaces at $5^{\circ}C$ infrared sensitivity (Figure 8b). After cooling for 7 minutes, however, the same sample shows the abrasions appearing about $0.2^{\circ}C$ lower in temperature than the surrounding glossy area (Figure 8c). It is noted that $0.2^{\circ}C$ is very small, and is near the instrument's lower limit on resolution.

4. FOREIGN SUBSTANCES ON PAINTED SURFACES

   a. In addition to abrasions, it is likely that portions of an aircraft surface may contain foreign substances such as lubricating oil, fuel, hydraulic fluid, etc. To see if such substances could cause thermovideo-

graph anomalies that might be interpreted as flaws, clean lubricating oil
and soiled machine grease were applied to the abraded Gr-D sample on 2.5
cm square areas. At room temperature (Figure 9a), a clean abrasion
appears about $0.2^{\circ}C$ cooler than unabraded glossy surface as usual, while
clean lubricating oil does not change surface emissivity characteristics
from those of the glossy paint. In fact, the oil appears to "cover up"
the slight apparent temperature effect of the abrasion. Heating for one
minute with a radiant heat source and cooling for three minutes yields a
thermovideograph where no apparent difference can be seen between glossy
paint, abrasion, and abrasion coated with clean lubricating oil (Figure 9b).
Continued cooling for a total of 6.5 minutes gives different results
(Figure 9c): both the clean abrasion and the oil coated abrasion appear
0.1 to $0.2^{\circ}C$ cooler than surrounding glossy paint. These differences
are extremely small, however, and could even have been caused by nonuniform
heating or cooling of the sample.

b. A photograph of sample Gr-D containing a clean abrasion, an
abrasion with a heavy coat of soiled machine grease, and a light 2.5 cm
x 2.5 cm coat of the same soiled grease on virgin painted surface is
shown in Figure 10. Thermovideographs are shown in Figure 11. At room
temperature (Figure 11a) there is little difference from the surrounding
area. When heated one minute and cooled for 30 seconds, however, the heavy
coat of soiled grease shows a minimum of $2^{\circ}C$ apparent temperature difference,
and the light coat of soiled grease appears nearly $1.4^{\circ}C$ higher in temperature
than the clean, painted surface (Figure 11b).

5. DISCUSSION. Surfaces coated with glossy Navy aviation paint can
appear thermographically different than virgin aluminum and epoxy matrix
composites. Paint thickness variations are clearly delineated on aluminum
surfaces, but are not thermographically visible on epoxy matrix surfaces.
The high gloss of the Navy aviation paint reflects concentrated heat
sources such as light bulbs, and surfaces to be inspected must be shielded
from such heat sources. Heavy clean abrasions on painted surfaces can
appear a few tenths of a degree centigrade cooler than virgin painted
areas, but should not be mistaken for flaws because the difference is so
slight. Clean lubricating oil does not appear differently from clean,

painted surfaces, and in fact seems to reduce the slight effect of abrasions. Soiled grease, on the other hand, can appear several degrees centigrade higher than clean, painted surfaces.

D. THERMAL FIELD APPLICATION METHODS

1. HEAT GUN. As a result of the preliminary studies (reference (a)), it became apparent that a heat gun method of applying energy to the sample would not be effective. For the inspection of large surface areas, the heat gun was too small a source. In addition, this method provided limited heat input into the sample. The following other methods were examined:

- Heat Lamp
- Local application of strip heaters
- Radiative thermal source

2. HEAT LAMP. Heat lamps have the potential to be relatively inexpensive and easy to maintain in the naval aviation maintenance environment. Ideally, banks of heat lamps could comprise a hand-held heater; burn-outs could be easily replaced from a stock of spares. For this study, one 250-watt heat lamp was used to heat selected samples of graphite/ epoxy. The resulting heat pattern was circular since there was only one bulb. The heat lamp, although providing adequate heat for certain NDE purposes, was judged not to have high enough heat output for detection of flaws existing deep within a structure. Perhaps this might be overcome by using higher wattage bulbs. The largest drawback to the use of the heat lamp is the tendency of examined surfaces to reflect the heat from the bulb. If heat lamps are to be used, they must be carefully shielded from surfaces under examination to avoid unwanted spurious thermographic output.

3. LOCAL STRIP HEATERS

a. The use of local surface heaters was considered because of the simplicity and economy of the method. A technician could apply the heaters over the surface to be inspected and then examine the temperature profiles with the thermovision camera as the energy was conducted through the sample. The results could then be compared with known unflawed standards. The technique would be based upon steady-state conditions and require only one

technician. (A radiative source method would examine transient response
and therefore would require two technicians, one applying the thermal
field and the second operating the camera. The advantages of this method
are no surface contact is required, and the thermal field application
would be uniform.)

   b. To examine the effectiveness of the local field application
method, a 15-cm x 13-cm x .24-cm sample of graphite/epoxy was used.
Figure 12 presents a sketch of the sample which included a 0.65-cm diameter
partial through-hole. The sample was 8-ply unidirectional laminate and
was not, therefore, isotropic. The sample was mounted in a manner similar
to the surface finish samples. Heat was applied by a heat gun in one case
and by Minco surface heaters mounted directly to the surface. For the
test using the heat gun, the sample was heated uniformly and then allowed
to cool by free convection. In the case of the surface heater, power was
applied to the heater to establish a given steady-state condition. The
energy was conducted along the sample and then was removed by free convec-
tion. A simplified analytical model, which considered the sample to be a
heated fin, was also examined so that comparisons with the experiments
could be made.

   c. Analytical prediction of the thermal response of the graphite/
epoxy sample with the heater applied to the surface was obtained using a
quasi one-dimensional fin approximation. In this approach, the sample is
assumed to have temperature gradients in the vertical direction only. The
sample was then divided into two regions; a heated region and an unheated
region. The governing equations for each region are given below (reference
(b)):

   Region A (Heated)

$$\frac{d^2 T_A}{dx^2} = \frac{hP}{kA}(T_A - T_\infty) - \frac{Q}{k} \tag{II-1}$$

where:

   T_A = Temperature in Region A

   Q = Heat dissipated by heater per unit cross sectional area

   h = Convective heat transfer coefficient

P = Perimeter of fin

A = Cross sectional area of fin

T_∞ = Ambient temperature

k = Thermal conductivity

x = Position along sample

Region B (Unheated)

$$\frac{d^2 T_B}{dx^2} = \frac{hP}{kA}(T_B - T_\infty) \tag{II-2}$$

where:

T_B = Temperature in Region B

The boundary conditions are:

x = 0: $dT_A/dx = 0$

x_r = a: $T_A = T_B$, $\dfrac{dT_A}{dx} = \dfrac{dT_B}{dx}$

x = b: $\dfrac{dT_B}{dx} = 0$

Solving these equations simultaneously and applying the boundary conditions, equations (II-3) and (II-4) are obtained.

$$T_B = T_\infty + \frac{QA}{hP}\left[\sinh ma \; \frac{\cosh mx}{\tanh mb} - \sinh mx\right] \tag{II-3}$$

$$T_A = T_\infty + \frac{QA}{hP}\left[1 + \frac{\sinh m(a-b)}{\sinh mb}\cosh mx\right] \tag{II-4}$$

$$0 \leq x \leq a$$

where: $m = (hP/kA)^{\frac{1}{2}}$

Using equations (II-3) and (II-4), the temperature distribution in the fin (sample) as a function of position for different values of h, k, and Q can be obtained.

d. Figure 13 presents the results for the case of the graphite/epoxy sample exposed to an external thermal field applied by a heat gun. In Figure 13a, the heat input was applied vertically, and in Figure 13b, the heat input was horizontal. It should be noted that the thermal conductivity was much greater in the horizontal direction than in the vertical direction. The white lines in the figures are particular isotherms which the camera

19

identifies. In both Figures 13a and 13b, the isotherm is distorted in the middle of the picture where the non-through hole defect is located. In addition, the thermal pattern is distorted at the top of the picture where an edge delamination has been introduced into the sample. Figure 13c presents results for the same case as 13a and 13b but with sensitivity set at 20°C from black to white rather than 50°C. The center defect is more pronounced because of the small range between shades.

e. The results for the case in which the heat was applied by means of a surface heater are entirely different. Figures 14a, 14b, and 14c present results for the cases of heat inputs of 1, 4, and 10 watts respectively. Heat flows from beneath the heater by conduction, and the flow pattern is altered when a defect is encountered. For each case in Figure 14, the temperature gradient is so steep that no discernible temperature effects reach the defect in the sample. In Figure 14a, the nonuniformities near the top of the picture are due to heater nonuniformities. The steep gradients are due to the low thermal conductivity in the vertical direction. Use of this approach for anisotropic laminates would require heater application near the defect. Since in the NDT situations the flaw location is not known, this approach would not be acceptable.

f. Theoretical results for the anisotropic case are shown in Figure 15. They agree with the experimental evidence that heat flow in the vertical direction is negligible. In Figure 14, the sensitivity is 5°C, meaning that the temperature range from black to white is 5°C. During the test, the black level was maintained at room temperature so that the middle of the picture in Figure 14a is about 1°C above room temperature. This is the approximate value at X/L = 0.5 and a heat input of 1 watt in Figure 15. Similar agreement exists at 10 watts. Unfortunately, a quasi-isotropic laminate of graphite/epoxy was not available at the time of these tests. However, a computer run for an isotropic sample indicated that the gradient is reduced considerably.

4. RADIANT HEAT SOURCE

a. Quasi-isotropic [0/±45/90]_s graphite/epoxy samples were obtained for the radiative field application evaluation. Initially, the 1320-watt space heater shown in Figure 16 was used. The samples used were 8-ply and

32-ply quasi-isotropic graphite/epoxy. Each sample was 30.8 cm x 46 cm and contained six manufactured delaminations. The delaminations were 6.4 mm x 6.4 mm, 12.7 mm x 12.7 mm, and 25.4 mm x 25.4 mm and were located at two different depths through the sample. This arrangement allowed for both size and depth detection studies. The samples were mounted vertically as shown in Figure 17.

b. Initial studies with the space heater and 8-ply sample were very encouraging. This method was preferable to the heat gun method which has some bias because defect location was known. However, with the thicker 32-ply sample, the commercial space heater proved to be an inadequate source. For the 8-ply sample, the defect was clearly visible for 2 minutes. At 32 plies, there was disagreement between experimenters if the defect was visible at all. Those who contended that the defect was visible, however, agreed that it was only for 1 or 2 seconds. For field use, this was minimally satisfactory. These results indicated that the heat source was not large enough to cause significant thermal effect at the defect. Quasi-isotropic graphite/epoxy has a large lateral conductivity (40 W/m^{o}C) compared to the thermal conductivity normal to the sample (0.5 W/m^{o}C). To cause significant effects through the sample thickness, a large thermal flux normal to the surface must be provided.

c. To determine the required heat input to the sample, a numerical model of the sample was created using 50 nodes, and was analyzed by the heat transfer code described earlier. The physical size of the model was 12.7 cm x 12.7 cm. There were 25 surface nodes exposed to the flux and 25 rear nodes. The conductive couplings between nodes accounted for the difference in normal and lateral thermal conductivity of graphite/epoxy. A delamination was simulated by varying the coupling between the center surface node and the rear node. Figure 18 presents results for the 32-ply graphite/epoxy laminate with 25.4-mm and 12.7-mm delaminations at the center node. The results show temperature of the sample 3 minutes after exposure to a 0.363 W/cm^2 flux. Depending upon the size of the delamination, a temperature distortion of 0.25 to 1.0^{o}C will exist for this flux. This magnitude is considered within the capability of the thermovision camera. A flux of 0.363 W/cm^2 is very large and is equivalent to approximately 3 earth solar constants. Using this data, a new radiative heat source was designed.

21

   d. Initially, the design considered a line source located a fixed
distance from the surface. Figure 19 presents the geometry examined in the
design. The parameters in the design were the diameter of the source, dis-
tance from the surface, and temperature of the source. The goal of the
design was to maintain the required flux at a distance of 15 cm of the
source centerline. Figure 20 presents a comparison of source temperature
versus source diameter for different distances from the surface at a flux
of 0.363 W/cm^2. From this figure, it is apparent that a single source
requires excessive temperatures for a reasonable size. An alternate
approach is to use multiple sources each providing a lower flux. For
instance, two sources providing 0.187 W/cm^2 each would operate at a
significantly lower temperature and provide the same input to the surface.
The final design was based upon a two-source configuration. Figure 21
presents the geometry of the final radiative heat source design. Figure
22 is a photograph of the actual heater. The heating elements consist
of 1.25-cm glass tubes around which nichrome wire is wound. The wire
spacing is adjusted to maintain a uniform temperature field on the rod.
The sides of the heater box are lined with polished aluminum to reflect
more radiant energy onto the sample surface. The use of reflected energy
reduces the required power of the heater and wire temperatures.

   e. The high powered radiative source was used on the 32-ply samples
with excellent results. These results are presented in the next section.

E. EVALUATION OF FLAW DETECTION CAPABILITIES. It has already been
established that thermography can detect flaws in composite materials
(reference (a)). The purpose of this section is to describe the size,
range, and types of flaws which can be located with the AGA thermovision
system.

   1. GRAPHITE/EPOXY LAMINATES. Graphite/epoxy was used for the first
portion of the flaw detection studies. Two thicknesses were considered:
8 ply, 1.19 mm.; and 32 ply, 5.26 mm. The laminates tested were a quasi-
isotropic $[0/\pm45/90]_s$ composite with approximately an 80:1 ratio between
the in-plane and normal-to-the-plane thermal conductivities; and a
$[0_2/\pm45]_s$ anisotropic layup with a 4:1 ratio of major to minor in-plane
conductivities; and approximately 160:1 ratio between major in-plane and

normal-to-the-plane conductivities. Two types of flaws were examined, namely simulated delaminations and non-through holes.

a. 8-Ply Graphite/Epoxy Laminates

(1) The simulated delaminations consisted of rectangular bags of hollow glass beads introduced into the sample during manufacturing. These square delaminations varied in size from 6.35 mm to 25 mm square. The flaws were located 1/8 of the thickness into the sample and 1/2 of the thickness. Figure 17 shows the 8-ply sample mounted in the test fixture.

(2) The non-through hole defects which simulate subsurface shattering due to impact damage were introduced into undamaged samples by drilling various size holes. Both the diameter and depth of the holes were varied. Hole diameters ranged from 12.7 mm to 6.4 mm. These tests were conducted only in the 32-ply samples and hole depth did not exceed one half of the sample thickness.

(3) The samples were mounted vertically as shown in Figure 23. Figure 24 shows the arrangement of the camera and the labelling of the test panels. Because of optical limitations, the camera's field of view could not cover the entire sample. The tests were, therefore, arranged to examine two flaws at a time.

(4) Figure 25 presents results for the 8-ply sample with the external field applied by the space heater. The delaminations are clearly visible in the photograph. The ten-color scale along the bottom of the picture shows the temperature range of the sample. This scale can be adjusted from $1^{o}C$ black to white to $1000^{o}C$ black to white. The most effective range used in the present study was between 2 and $20^{o}C$.

b. 32-Ply Graphite/Epoxy Laminates

(1) As discussed earlier, the space heater was ineffective on the 32-ply sample. The heater shown in Figure 22 was used on the 32-ply samples. For all the tests, the heater was operated at 1.0 KW and exposed to the sample for 60 seconds. The infrared camera lens was positioned approximately 2 meters from the sample.

(2) Figure 26 presents results showing flaws B2 and C2 approximately 60 seconds after the heat source was removed. The camera sensitivity level is $10^{o}C$ black to white. It should be noted that for this

23

32-ply sample the defects are not visible to the naked eye. At the moment
of removal of the heater, the camera indicated that the sample had been
uniformly heated. The sample then cools by free convection uniformly
except in the vicinity of the defects. Figure 27 presents the same results
for the case in which flaws A2 and B2 are illuminated. Flaw A2 is the 6.4
mm square located half way through the sample. It is located at the large
white spot in Figure 27a. Flaw B2 is the smaller white spot to the right
of the picture. Figure 27b was taken sometime later in the cooling cycle.
The white line outlining the colored region is an isotherm. Flaw A2 is
located at the light orange spot in the center of Figure 27b.

(3) Figure 28 presents a sequence of pictures with the sample
inverted so that the flaws, located 1/8 of the way through the sample, are
in the field of view of the camera. In Figure 28a, flaw B1 is clearly
visible at the right of the picture. Flaw C1 is masked in the hot area
at the center of the picture. It is difficult to get both flaws (C1 and B1)
at the same temperature so that they might be visible early in the cooling
process. Views b, c, and d of Figure 28 present other attempts to capture
both flaws by waiting longer in the cooling period. Figure 28c represents
the best results clearly showing both flaws although C1 is still hotter.

(4) Views a, b, and c of Figure 29 present a sequence of pic-
tures of flaws A2, B2, and C2 which, because they are at the midplane of
the sample, have the same relative position to the surface as Figures 26
and 27. Figure 29a shows defect C2 at the center of the picture. Figure
29b shows C2 as a bright spot at the center and B2 at the right. Figure
29c presents the smallest defect A2 at the right side of the picture.

(5) Following these tests, the sample was reversed so that
flaws A1, B1, and C1 were 7/8 of the sample thickness from the heated
surface. This represents the most severe test of the flaw detection
capable of the sample. Figure 30a and b shows flaws A1 and B1 clearly.
The camera sensitivity was set at $10^{\circ}C$ for these pictures. Figure 30b
shows the smallest defect A1 to the left outlined by an isotherm. Figure
31 presents, for the same sample orientation, defects B1 and C1. Flaw C1
appears to the right side. Figure 31a is for a sensitivity of $10^{\circ}C$ while
for Figure 31b, the setting was $5^{\circ}C$. These results show that if a higher
power heat source is used, flaws in thicker samples can be located. Un-
fortunately, the 32 ply was the thickest specimen available.

24

(6) All of the preceding results were obtained on the quasi-isotropic $[0/\pm45/90]_s$ graphite/epoxy samples. In order to test the effects of in-plane thermal anisotropy, partial through-holes were drilled in an anisotropic $[0_2/\pm45]_s$ graphite/epoxy laminate composed of 32 plies, and having in-plane principal thermal conductivities of 80W/m deg C and 20 W/m deg C. Hole diameters were small (6 to 11 mm) and ranged from 25% to 87% through the thickness. The anisotropic specimen was heated and observed from the intact surface; no evidence of the partial through-holes could be seen with the unaided eye. Figure 32 presents the defect map for the specimen as seen from the intact side. Note the existence of an unintentional delamination in the sample, at an unknown depth, which was identified by the manufacturer's C-scan.

(7) Defects were examined two or three at a time since the Thermovision could not accommodate the entire sample in its field of view. Figure 33 presents typical thermovideograph results after heating with a radiant heat source for 10 to 30 seconds, and cooling for 5 to 10 seconds. In Figure 33a, a 6-mm-dia, 87% through-hole shows as a large bright spot to the left, and an 11-mm-dia, 65% through-hole can be seen to the right. An 11-mm-dia, 25% through-hole centrally located above the two bright spots, at the apex of an equilateral triangle, cannot be observed. In fact, neither of the 25% through-holes could be identified in this sample. Figure 33b shows an 11-mm-dia, 65% through-hole to the left, and an 11-mm-dia, 50% through-hole to the right, at an infrared camera sensitivity of 2°C. The defect nearer the observed surface appears more clearly, as expected. Note that the infrared camera also shows a hot spot between the two man-made flaws, corresponding to the size and location of the aforementioned unintentional delamination. Figure 33c shows the same three flaws at a 5°C camera setting. Finally, it is noted that the laminate's thermal anisotropy did not appear to affect the detectability of the defects; the only difference between the $[0_2/\pm45]_s$ and $[0/\pm45/90]_s$ results is a slight elongation of the "hot spots" in the direction of greatest conductivity for the anisotropic sample.

25

2. S2-GLASS/EPOXY LAMINATES

a. Glass/epoxy composites are common in several different types of aircraft. Since the in-plane thermal conductivities of glass/epoxies are usually an order of magnitude or two less than graphite/epoxies (about $0.5 \ W/m^{\circ}C$ versus $40 \ W/m^{\circ}C$ for quasi-isotropic laminates), it was judged necessary to test a typical glass/epoxy material for flaw detection ability. An S2-glass/epoxy, 3M SP-250-S2, was chosen. Panels up to 16 ply having a thickness of about 4 mm were fabricated with plastic bags (empty) to simulate flaws. Unfortunately, the bags bonded during the curing process and did not provide a thermal image when heated. Therefore, the laminates were impacted by a blunt object several times at a velocity of about 3 m/sec to open the delaminations. Only the 2.5 cm square delaminations were able to be opened in the 32-ply sample. In addition to the simulated delaminations, partial-through-holes from 6 mm to 13 mm in diameter and up to 80% through the thickness were drilled in the samples. Figure 34 is a defect map for the 16-ply [0/±45/90] panel.

b. Results of testing the 16-ply panel are shown in Figure 35. Two partial-through-holes, one 20 mm dia, 15% through (left) and one 11 mm dia, 60% through (right) are seen above a 25-mm-square delamination one ply from the top, 10 seconds after heating, in Figure 35a. Figure 35b shows the same section of panel after cooling for six minutes. Note that the free convection cooling has reversed the temperature of the surface over the holes, and that the delamination is no longer visible. A 25 mm square delamination located halfway through the thickness was heated for 10 seconds and cooled for 10 seconds, and resulted in the thermovideograph of Figure 35c. The delamination is visible by its $0.3^{\circ}C$ temperature rise above surrounding area. In Figure 35d, three partial-through-holes are visible as hot spots (left-to-right: 20 mm dia, 15% through; 11 mm dia, 60% through; and 11 mm dia, 30% through).

c. Four other delamination-type defects could not be detected; these were two (0.5 cm square) implanted one ply and 8 plies down from the surface, respectively, and two others induced by repeated impact with a blunt object. The two implanted delaminations were not true separations, as previously indicated. The type and extent of the blunt object-induced damage sites is not known. Therefore, it is impossible at this time to draw meaningful conclusions from these four defects.

NAEC-92-157

3. <u>DISCUSSION</u>. The flaw detection capability studies have shown
that delaminations and partial-through holes can be detected in quasi-
isotropic and anisotropic laminates of graphite/epoxy and S2-glass/epoxy.
Sizes ranged from 0.6 cm to 2.5 cm across, located as far as 7/8 through
the thickness of up to 32 plies thick graphite/epoxy and 16 plies thick
S2-glass/epoxy. The infrared camera was even able to detect an uninten-
tional flaw induced during manufacturing. Anisotropy does not seem to have
any significant effect on the detection of flaws. The thickest laminates
available were 5-mm 32-ply graphite/epoxy and 4-mm 16-ply S2-glass/epoxy
samples; it does not appear that the limits of size and location on
delamination detection capability have yet been found.

III. STRESS-GENERATED THERMAL FIELD METHOD

A. OBJECTIVES AND OUTLINE OF THE SGTF STUDY

1. The SGTF study had as its primary objective the determination of the feasibility of detecting flaws in composite and metal structures by generating heat near the flaws with high-frequency, low-stress cyclic loading. It had been known that partial-through holes, notches, and delaminations can be detected by SGTF methods in glass/epoxy, boron/ epoxy, and graphite/epoxy structures. It is not known, however, whether composite structures can be damaged by the levels of cyclic stress application necessary to generate heat for thermal flaw detection. Also, SGTF techniques have not been successful for metal structures. The planned SGTF study was to first determine the levels of stress and frequency which can be applied to structural composites and metals without causing structural damage and still obtain a thermal image allowing flaw detection.

2. The study begins by first performing a semi-empirical analysis of the heat generated in cyclically loaded composites, and experimentally calibrating two materials--a graphite/epoxy and an S2-glass/epoxy composite. The results of the semi-empirical heat generation analysis are then used in conjunction with a finite element stress analysis to predict heat generated near a 6-mm- dia hole in graphite/epoxy and glass/epoxy tensile specimens. The analytical results are compared to the results of tests run on these specimens. Aluminum specimens were also tested and their results are also described. Finally, a feasibility assessment of SGTF techniques in composites and metals is made, and the results of a preliminary investigation into ultrasonic SGTF methods is presented.

B. ANALYSIS OF HEAT GENERATION IN CYCLICALLY LOADED COMPOSITES

1. APPROACH TO THE PROBLEM

a. Determination of heat generation in composite materials under cyclic loading can be approached in several ways. At the one extreme, a detailed analysis of viscoelastic stresses in a unidirectional composite could be made, and the heat energy per unit time dissipated due to viscoelastic behavior could be calculated. This would necessitate knowing the in situ viscoelastic properties of the epoxy matrix material. Even if

an extensive testing program could be undertaken to determine these prop-
erties, it is likely that the average in situ matrix properties would not
be the same due to curing differences and the existence of voids, imper-
fections, disbonds between fiber and matrix, etc. At the other extreme
lies a purely empirical approach which, through cyclic thermomechanical
testing, could experimentally determine the viscoelastic heat generated
for a wide range of composite laminates, combined stress states, and
cyclic frequencies. This totally empirical approach is unrealistic be-
cause of the vast number of specimens and tests which would be required.

b, The approach adopted for this study chose appropriate elements
from both extremes combined into a semi-empirical analysis. First, elastic
stresses were determined in a representative volume element of unidirectional
composite under a general state of in-plane combined stress. Next, a
suitable viscoelastic material model was chosen, and the form of an
equation for viscoelastic point heat energy generated was developed from
this model. It was assumed that the elastic and viscoelastic stress states
were not significantly different, and the elastic stress distribution was
combined with the viscoelastic point heat energy model to give an equation
for average heat energy dissipated in a unidirectional layer of composite.
The equation contains two constants which can be determined for a given
composite material system from a limited number of tests on simple laminates.

c. With this semi-empirical equation for heat generated in a uni-
directional composite, the procedure for determining heat generated and
temperatures in a laminated structural composite is as follows: First,
a global structural elastic stress analysis is performed under the cyclic
loads using any conventional method (such as finite element analysis).
Next, the structure is divided into convenient subregions, and stresses in
each layer are calculated using laminate analysis techniques. The semi-
empirical heat generation equation is then used for each layer of each
subregion to determine rate of heat generation. Finally, a heat transfer
analysis is performed on the discretized structure, and temperature distri-
butions are calculated. Figure 36 illustrates this procedure.

2. <u>STRESSES IN UNIDIRECTIONAL COMPOSITES</u>

a. In order to develop a semi-empirical equation for heat generated under cyclic loading in composites, it is desirable to know the detailed state of stress and strain in the fiber and matrix phases due to cyclically applied unidirectional layer average stresses. The heat energy generated due to viscoelastic behavior can then be calculated by integrating stress times differential strain over one cycle of applied layer average stresses and dividing by the time for one load cycle. The exact determination of viscoelastic stresses and strains in the fiber and matrix phases of a composite layer is a very difficult task, and requires knowledge of fiber and matrix viscoelastic properties. Nearly all high strength fibers can be considered elastic compared to epoxy matrix materials. Hence, nearly all heat generated in epoxy matrix composites will be due to the visco-elasticity of the matrix material. Therefore, it is assumed herein that fibers are purely elastic, and that all heat generated will be in the matrix. Even with this assumption, however, exact solution to the visco-elastic stresses and strains is very difficult. In composites, in the part of the stress-strain range which is below the point where damage to either fiber or matrix can occur, the matrix is elastic enough to calculate stresses for engineering purposes using a linear elastic analysis. It will there-fore be assumed in this study that stresses (not strains) in the epoxy matrix of a unidirectional layer can be determined in terms of the applied average layer stresses by an elastic analysis. Resulting strains can then be determined from the viscoelastic constitutive relations. It is noted that stress equilibrium will be satisfied by this procedure, but not necessarily compatibility.

b. Determination of matrix stresses in a unidirectional composite layer requires choice of fiber and matrix phase geometry. Actual distribu-tion of fibers in the matrix is statistical in nature, with some regions approximated by a rectangular array and others approximated by an (irregular) hexagonal array (Figure 37). These deterministic, regular fiber/matrix geometries, however, make it difficult to obtain analytical stress distri-butions by other than numerical analyses (references (c) and (d)). The randomness of fiber distribution which exists in a composite layer can be

approximated by the Hashin-Rosen composite cylinder assemblage (CCA)
(reference (e)) which assumes that the composite consists of composite
cylinders; each composite cylinder consisting of an inner fiber cylindri-
cal core surrounded by a matrix annulus (Figure 37c). Each composite
cylinder may have a different outer diameter, but all have the same ratio
of fiber radius to composite cylinder outer radius, a/b. The volume
fraction of fibers in the composite is therefore always spacewise constant
on an average basis. Use of the CCA geometry approximation has several
advantages: It has been demonstrated that average elastic composite prop-
erties determined using CCA geometry are very close to experimental results
and numerical results using rectangular or hexagonal arrays. In addition,
closed form equations for displacements have been determined by Hashin and
Rosen (reference (e) and (f)) from which matrix stresses can readily be
determined for all but one case of average layer stresses. Therefore, the
CCA phase geometry approximation is adopted here.

    c. Consider a unidirectional layer of composite material under
in-plane loading (Figure 38). The axial (1) direction is parallel to the
fibers, the transverse (2) direction is perpendicular to fibers in the
plane of the layer, and the normal (3) direction is perpendicular to the
plane of the layer. Average in-plane composite layer stresses are axial
normal stress, $\overline{\sigma}_{11}$; transverse normal stress, $\overline{\sigma}_{22}$; and axial shear stress,
$\overline{\sigma}_{12}$. The matrix material is assumed to be isotropic, and the fibers are
assumed to be transversely isotropic with principal elastic axis along
fiber axis. Hashin (reference (f)) gives displacements for the cases of
axial normal straining, axial shearing, and plane strain isotropic
straining in the 2-3 plane. He also gives displacement and stress fields
for calculating upper and lower bounds to composite shearing modulus in
the 2-3 plane, but these latter displacement fields are not exact solutions.
There are no closed form exact solutions to transverse normal straining of
a composite.

    (1) Axial Normal Stress. Stresses in matrix material due to
axial straining of a unidirectional composite are given in cylindrical
polar coordinates (Figure 37d) as:

31

$$\sigma_{rr}^{m} = L_m \epsilon^o + 2K_m B_1 - \frac{2G_m C_1}{r^2} \qquad \text{(III-1a)}$$

$$\sigma_{\theta\theta}^{m} = L_m \epsilon^o + 2K_m B_1 + \frac{2G_m C_1}{r^2} \qquad \text{(III-1b)}$$

$$\sigma_{zz}^{m} = N_m \epsilon^o + 2L_1 B_1 \qquad \text{(III-1c)}$$

$$\sigma_{r\theta}^{m} = \sigma_{\theta z}^{m} = \sigma_{rz}^{m} = 0 \qquad \text{(III-1d,e,f)}$$

Where σ denotes stress, r is radial coordinate, θ is hoop coordinate, z is axial coordinate, superscript and subscript m denotes matrix, K and G are bulk and shearing modulus, respectively, ϵ^o is applied layer axial straining, L_m and N_m are constants which are functions of matrix elastic constants, and B_1 and C_1 are constants of integration which are found from interface and boundary conditions (see reference (f) for more detail). Since the composite is in uniaxial straining, the average axial normal composite stress $\overline{\sigma}_{11}$ is related to the applied axial strain ϵ^o by

$$\overline{\sigma}_{11} = E_A^{*} \epsilon^o \qquad \text{(III-2)}$$

where E_A^{*} is the effective axial modulus of the unidirectional layer. Using (III-2) and the boundary/continuity conditions, the following equations are obtained for matrix stresses due to average axial normal composite layer stress (reference (g)):

$$\sigma_{rr}^{m} = \overline{\sigma}_{11} \left(H_1 - \frac{H_2}{r^2} \right) \qquad \text{(III-3a)}$$

$$\sigma_{\theta\theta}^{m} = \overline{\sigma}_{11} \left(H_1 + \frac{H_2}{r^2} \right) \qquad \text{(III-3b)}$$

$$\sigma_{zz}^{m} = \overline{\sigma}_{11} H_3 \qquad \text{(III-3c)}$$

with remaining stresses equal to zero (see eq.(III-1d,e,f), and

$$H_1 = \frac{2G_m}{E_A^{*}} \; \frac{(\nu_m - \nu_f)V_f}{(G_m V_f / K_m + G_f V_m / K_f + 1)} \qquad \text{(III-3d)}$$

32

$$H_2 = \frac{2G_m}{E_A^*} \frac{(\nu_m - \nu_f)a^2}{(G_m V_f/K_m + G_f V_m/K_f + 1)} \tag{III-3e}$$

$$H_3 = \frac{E_m}{E_A^*} \left[1 + \frac{4G_m V_f}{E_m} \cdot \frac{\nu_m(\nu_m - \nu_f)}{G_m V_f/K_m + G_f V_m/K_f + 1}\right] \tag{III-3f}$$

Here, E is Young's modulus, ν is Poisson's ratio, V is volume fraction, subscript f refers to fiber quantities, and remaining symbols are as before.

(2) Axial Shear. If u_1, u_2, u_3 represent displacements in the layer coordinate system (Figure 38), then applying the following displacements to the lateral composite cylinder surface is equivalent to macroscopic shear straining:

$$u_1 = \epsilon_{12}^o X_2$$
$$u_2 = \epsilon_{12}^o X_1 \qquad \text{on lateral surface} \tag{III-4a,b,c}$$
$$u_3 = 0$$

with ϵ_{12}^o being the macroscopic tensorial shear strain (a constant). These displacements give rise to matrix stresses of (see reference (g)):

$$\sigma_{rz}^m = \bar{\sigma}_{12} (J_5 + J_6 a^2/r^2)\cos\theta \tag{III-5a}$$

$$\sigma_{\theta z}^m = \bar{\sigma}_{12}(J_5 - J_6 a^2/r^2)\sin\theta \tag{III-5b}$$

$$\sigma_{rr}^m = \sigma_{\theta\theta}^m = \sigma_{zz}^m = \sigma_{r\theta}^m = 0 \tag{III-5c,d,e,f}$$

where $\bar{\sigma}_{12}$ is the composite layer average shear stress given by

$$\bar{\sigma}_{12} = 2G_A^* \epsilon_{12}^o, \tag{III-5g}$$

G_A^* is the effective shearing modulus of the unidirectional layer, and

$$J_5 = \frac{G_m(\gamma+1)}{G_A^*(\gamma V_m + 1 + V_f)} \tag{III-5h}$$

$$J_6 = \frac{G_m(\gamma-1)}{G_A^*(\gamma V_m + 1 + V_f)} \tag{III-5i}$$

$$\gamma = G_f/G_m . \tag{III-5j}$$

(3) **Transverse Normal Stress.** As previously stated, no exact
solution exists for matrix stresses in a unidirectional composite layer
under transverse normal straining or stressing. Hashin (reference (f)),
however, has presented the displacement field solution for plane isotropic
straining. He also presents a displacement field and a stress field used
to obtain upper and lower bounds, respectively, to the effective composite
transverse shear modulus. While neither of these "upper and lower bound"
solutions has been shown to be an exact solution to the problem of applied
composite transverse shear stress, it is believed that the displacement
field used for the upper bound on effective transverse shear modulus is
closer to the exact solution. Therefore, the "upper bound" displacement
field is used here to obtain matrix stresses for plane strain shear
straining of a composite cylinder. Determination of matrix stresses due
to applied composite transverse normal stress is obtained from the plane
strain isotropic and transverse shear straining solutions by superposition
in the following manner (see Figure 39 and reference (g)): First, the "upper
bound" solution for a transverse shear stress of $\bar{\sigma}'_{22}/2$ (Figure 39a) is
transformed to axes at 45° to the 2-3 axes giving a tensile and compressive
plane strain biaxial stress state (Figure 39b). Next, the plane isotropic
straining solution corresponding to a stress of $\bar{\sigma}'_{22}/2$ (Figure 39c) is
added to the transverse shear solution, giving the plane strain transverse
stress solution (Figure 39d). The resultant composite axial stress $\bar{\sigma}'_{11}$
required to maintain plane strain is determined by integrating σ_{11} over
the X_1 = constant end surfaces of the element, and the solution to an
axial compressive stress of $\bar{\sigma}'_{11}$ (Figure 39e) is superimposed in the plane
strain transverse stress solution to yield the desired plane stress trans-
verse stress solution (Figure 39f). Reference (g) gives more detail. The
final solution for the transverse normal stress problem is

$$\sigma_{rr}^m = \bar{\sigma}_{22} [(D_1+D_3/r^4-2D_4/r^2)\cos 2\theta + I_1 + I_2/r^2] \tag{III-6a}$$

$$\sigma_{\theta\theta}^m = \bar{\sigma}_{22} [-(D_1+2D_2r^2+D_3/r^4)\cos 2\theta + I_1 - I_2/r^2] \tag{III-6b}$$

34

$$\sigma_{zz}^{m} = \bar{\sigma}_{22} \left[-2\nu_m (D_2 r^2 + D_4/r^2)\cos 2\theta + I_3 - H_3 I_8 \right] \qquad \text{(III-6c)}$$

$$\sigma_{r\theta}^{m} = \bar{\sigma}_{22} \left[D_1 + D_2 r^2 - D_3/r^4 + D_4/r^2 \right] \sin 2\theta \qquad \text{(III-6d)}$$

where

$$D_1 = G\, A_1^{\varepsilon}/2G_T^* \qquad \text{(III-6e)}$$

$$D_2 = 3G_m A_2^{\varepsilon}/2G_T^* (3-2\nu_m) a^2 \qquad \text{(III-6f)}$$

$$D_3 = 3G_m A_3^{\varepsilon} a^4/2G_T^* \qquad \text{(III-6g)}$$

$$D_4 = G_m A_4^{\varepsilon} a^2/2G_T^* (1-2\nu_m) \qquad \text{(III-6h)}$$

$$I_1 = K_m(K_f + G_m)/2K^*[K_f + G_m - (K_f - K_m)(a/b)^2] \qquad \text{(III-6i)}$$

$$I_2 = G_m a^2 (K_f - K_m)/2K^*[K_f + G_m - (K_f - K_m)(a/b)^2] \qquad \text{(III-6j)}$$

$$I_3 = L_m(K_f + G_m)/2K^*[K_f + G_m - (K_f - K_m)(a/b)^2] \qquad \text{(III-6k)}$$

$$I_8 = I_3 V_m + \frac{V_f L_f (K_m + G_m)}{2K^*[K_f + G_m - (K_f - K_m)(a/b)^2]} \quad , \qquad \text{(III-6l)}$$

K^* is composite layer effective bulk modulus, L is phase elastic Lamé parameter, and the A_1^{ε} are constants found from the equations

$$C_{kl}^{\varepsilon} A_l^{\varepsilon} = d^{\varepsilon} \qquad \text{(III-6m)}$$

where C_{kl}^{ε} and d_k^{ε} are given in Table 4.

(4) Solution for General In-Plane Composite Stress. Equations (III-3), (III-5), (III-6), and Table 4 give stresses in matrix material of a unidirectional composite subjected to average composite axial normal stress, axial shear stress, and transverse normal stress, respectively. Since the equations are linear, they may be superimposed to give the matrix stresses due to any general combination of in-plane composite stresses. The final result will be of the form

$$\sigma_{ij}^{m} = A_{ij\alpha\beta}\bar{\sigma}_{\alpha\beta} \qquad \text{(III-7)}$$

where the usual index notation is used; i and j can take on values of r, θ, or z; α and β are 1 or 2; $\bar{\sigma}$ is applied composite layer stress; σ^m is matrix stress; and the $A_{ij\alpha\beta}$ are functions of position coordinates r and θ, elastic constants of fiber and matrix, composite layer elastic constants, and phase volume fractions. The $A_{ij\alpha\beta}$ are determined readily from equations (III-3, 5, and 6) and Table 4.

3. <u>VISCOELASTIC CYCLIC HEAT GENERATION MODELS</u>. It is assumed that all mechanical energy dissipated during cyclic stressing of a visco-elastic matrix composite material goes into heat. In order to determine the energy dissipated in cyclic loading, and hence heat generation, several models were considered.

a. First, a purely empirical exponential relation for energy dissipated per unit cycle of stressing was considered:

$$D_c = C\sigma_0^m \omega^n \qquad \text{(III-7)}$$

where D_c is energy dissipated per unit volume of composite, σ_0 is a measure of stress amplitude, ω is cyclic frequency, and c, m, n are empirical constants which can be determined from experimental data. This specific form was chosen since it is physically obvious that D_c must be zero whenever σ_0 or ω go to zero; hence, m and n must both be positive. The primary drawback of this model is that it does not predict a maximum level of energy dissipated per unit time as cyclic frequency goes to infinity. Since this is a property of all linear viscoelastic materials, the exponential form (III-7) was judged unfit for the present analysis.

b. An analysis of a general linear viscoelastic material under cyclic stresses was then made. The differential viscoelastic stress-strain relation for linear viscoelastic materials is of the form (reference (h))

$$P\sigma = Q\epsilon \qquad \text{(III-8a)}$$

where σ and ε are stress and strain measures, and P and Q are linear differential operators with constant coefficients

$$P = \sum_{i=0}^{m} P_i \frac{d^i}{dt^i} \qquad \text{(III-8b)}$$

$$Q = \sum_{i=0}^{m} q_i \frac{d^i}{dt^i} \qquad \text{(III-8c)}$$

36

Here, m and n are any integer numbers, p_i and q_i are material (visco-
elastic) constants, and t is time. It is known that epoxy matrix materials
behave like viscoelastic solids over moderate time intervals. The
simplest of these is the three-parameter solid modeled by a Kelvin-Voigt
parallel spring-dashpot element in series with another spring, for which
equation (III-8) becomes

$$\sigma + p_1\dot{\sigma} = q_o\epsilon + q_1\dot{\epsilon} \tag{III-9}$$

where the overdot denotes time differentiation. Although higher order
parameter solids were considered, the three-parameter solid has all of the
basic behavior desired in a viscoelastic solid, and, because of its
simplicity, will be easier to work with empirically. It is also felt that
use of a higher order model would result in "overkill" and could not be
justified.

    c. With the fundamental form (III-9) chosen, it is necessary to
select the form of the stress and strain measures, σ and ϵ. Although in
general most polymeric materials exhibit viscoelastic volume change, this
volumetric viscoelastic behavior is generally considerably less than that
due to pure distortion, especially for low stress and strain levels.
Accordingly, the stress and strain measures chosen for the analysis were
the stress and strain deviators, S_{ij} and e_{ij}, respectively, given by

$$S_{ij} = \sigma_{ij} - \frac{\sigma_{kk}}{3}\delta_{ij} \tag{III-10}$$

$$e_{ij} = \epsilon_{ij} - \frac{\epsilon_{kk}}{3}\delta_{ij} \tag{III-11}$$

where ϵ_{ij} and σ_{ij} are strain and stress tensors, and δ_{ij} is the Kronecker
delta. The usual subscript notation convention is employed. The assumed
constitutive relation for the matrix material is, therefore, the isotropic
form

$$S_{ij} + p_1\dot{S}_{ij} = q_1e_{ij} + q_2\dot{e}_{ij} \tag{III-11}$$

In order to obtain energy dissipated per unit cycle, it is assumed that the
applied deviatoric stresses are in the form of a cyclic component S_{ij}^o super-
imposed on a constant level S_{ij}^*:

$$S_{ij} = S_{ij}^* + S_{ij}^o \sin \omega t \tag{III-12}$$

The resulting strain deviator can be found by using (III-12) and solving (III-11) to give

$$e_{ij} = A_{ij} \sin \omega t + B_{ij} \cos \omega t + e_{ij}^* \tag{III-13a}$$

where

$$A_{ij} = S_{ij}^o [1 + (p_1 q_1 - q_2) \omega^2 / (q_1^2 + q_2^2 \omega^2)] \tag{III-13b}$$

$$B_{ij} = S_{ij}^o (p_1 q_1 - q_2) \omega / (q_1^2 + q_2^2 \omega^2) \tag{III-13c}$$

$$e_{ij}^* = S_{ij}^* / q_1 \tag{III-13d}$$

Energy dissipated per unit cycle per unit volume of matrix D_c^m is given by

$$D_c^m = \int_{cycle} S_{ij} de_{ij} = \frac{1}{\omega} \int_{\omega t = 0}^{\omega t = \omega T_1} S_{ij} \dot{e}_{ij} d(\omega t) \tag{III-14}$$

which, upon substitution of equations (III-12,13) into (III-14), becomes

$$D_c^m = \frac{\pi \omega (q_2 - p_1 q_1)}{q_1^2 + q_2^2 \omega^2} S_{ij}^o S_{ij}^o \tag{III-15}$$

Equation (III-15) gives the energy dissipated per unit volume in one cycle of stressing for the matrix material. The composite material, treated as an "average" material, heats up by an amount equal to the energy dissipated per unit composite volume multiplied by the volume of composite under cyclic stress. The energy dissipated in a cycle of loading per unit composite volume, $\overline{D}_c$, can be found by averaging the matrix energy dissipated over the composite volume V:

$$\overline{D}_c = \frac{1}{V} \int_V D_c^m \, dV = \frac{\pi \omega (q_2 - p_1 q_1)}{q_1^2 + q_2^2 \omega^2} \cdot \frac{1}{V} \int_V S_{ij}^o S_{ij}^o \, dV \tag{III-16}$$

$$= \frac{\pi \omega (q_2 - p_1 q_1)}{q_1^2 + q_2^2 \omega^2} \overline{S_{ij}^o S_{ij}^o} \tag{III-16}$$

where the overbar denotes volume average. The energy dissipated per unit composite volume per unit time (energy dissipation rate density) is found by dividing $\overline{D}_c$ by the time for one cycle, $2\pi/\omega$, to give

$$\dot{\overline{D}} = \overline{D}_c/(2\pi/\omega) = \frac{(q_2 - p_1 q_1)\omega^2}{2(q_1^2 + q_2^2 \omega^2)} \overline{s_{ij}^o s_{ij}^o} \qquad \text{(III-17)}$$

    d. The problem of determining either energy dissipation density per cycle, $\overline{D}_c$, or energy dissipation rate density, $\dot{\overline{D}}$, is seen to reduce to one of determining the composite volume average of the inner product of the stress deviator amplitudes, $\overline{s_{ij}^o s_{ij}^o}$, and the material viscoelastic parameters q_1 and p_1. As mentioned previously, epoxy materials are only weakly viscoelastic at low stresses and moderate time spans. Therefore, an extremely good approximation to the viscoelastic matrix stress amplitudes, σ_{ij}^{mo}, in terms of applied composite layer stress amplitudes, $\overline{\sigma}_{\alpha\beta}^o$ will be given by the elastic stress amplitudes found from equations (III-3,5,6, and 7) and Table 4 of the preceding section. Equation (III-10) is then used to determine the matrix stress deviator amplitude s_{ij}^o. Finally, the composite volume averaged $\overline{s_{ij}^o s_{ij}^o}$ is determined. Results will be of the form

$$\overline{s_{ij}^o s_{ij}^o} = E_{\alpha\beta\gamma\delta}\sigma_{\alpha\beta}^o \sigma_{\gamma\delta}^o \qquad \text{(III-18)}$$

where the constants $E_{\alpha\beta\gamma\delta}$ depend upon fiber and matrix elastic constants and phase geometry. The remaining task, that of finding matrix viscoelastic properties, is handled empirically as follows.

    e. Equations (III-15 and 17) can be rewritten in the form

$$\overline{D}_c = \frac{\omega \overline{s_{ij}^o s_{ij}^o}}{A + B\omega^2} \qquad \text{(III-16a)}$$

$$\dot{\overline{D}} = \frac{\omega^2 \overline{s_{ij}^o s_{ij}^o}}{2\pi(A+B\omega^2)} \qquad \text{(III-17a)}$$

where

$$A = q_1^2/\pi(q_2 - p_1 q_1)$$

$$B = q_2^2/\pi(q_2 - p_1 q_1)$$

It is clear that if the only quantity of interest is heat energy generated and not the general viscoelastic behavior, then only the two constants A and B need be determined instead of the three p's and q's. The constants A and B can be found from mechancial cyclic tests on specimens of a given material system by determining the energy dissipated per cycle from the composite stress-strain curve hysteresis loop at several cyclic stress amplitudes and frequencies. The next section describes such cyclic tests performed on graphite/epoxy and S2-glass/epoxy.

4. **CALIBRATION TEST PROGRAM AND MODEL EVALUATION**

a. The empirical viscoelastic matrix constants A and B in the energy dissipation equations (III-16a, 17a) have been experimentally determined for the graphite/epoxy and S2-glass/epoxy composites described previously. Cyclic tests were attempted on unidirectional and $[\pm45]_s$ laminates of both materials. Specimens were strain gaged and tested on a cyclic tensile testing apparatus specially built for this purpose. Load cell and strain gage outputs were amplified and fed into an x-y oscilloscope. The resulting hysteresis loops were photographed and energy dissipation density per cycle calculated for several levels of applied composite load and cyclic frequency. A linear regression analysis was performed on the data and the constants A and B determined.

b. Tensile specimens were cut from panels of [0] and [±45] laminates to provide axial tensile (fibers in load direction), transverse tensile (fibers perpendicular to load direction) and primarily axial shear ([±45] angle ply) specimens. It was found early on that the axial tensile specimens did not provide a measurable hysteresis loop and were dropped from the testing program. Difficulty with breaking the relatively fragile transverse specimens eliminated them from providing meaningful results. Nearly all results, therefore, were obtained from 8-ply graphite/ and 4-ply S2-glass/epoxy $[\pm45]_s$ tensile specimens in which the layers are in a stress state dominated by axial shear. All specimens were appropriately end-tabbed with glass/epoxy strips. Dimensions of the specimens are shown in Table 5.

c. The cyclic tensile testing apparatus used was designed and built specifically for this program. The apparatus consists of a 350-kg vibra-

tion isolation platform constructed of bolted plywood and railroad ties and supported at four corners by helical springs (Figure 40). The highest natural frequency of the platform and machine is 2 Hz. A stiff support structure fabricated from welded 25-mm steel plate is bolted to the isolation platform and holds a hardened steel fulcrum. Resting on the fulcrum is a hardened steel lever arm, one end of which is attached to the specimen grip and load cell hardware, and the other end of which is pinned to a load actuating rod. The load actuating rod is driven by a 65-mm dia shaft with a 9-mm eccentric. The drive shaft is in turn driven through a belt-and stepped-pulley arrangement by either a 1-hp or a 3-hp electric motor. (It had been initially planned to actuate the lever arm by an electronic shaker with a 75-kg exciting force and frequency capability in excess of 10,000 Hz, but untimely failure of the shaker forced the motor-and-pulley design.) The lever arm position is variable and provides lever arm ratios of 30:1 to less than 1:1 in order to control the applied specimen displacement and hence load. The specimen gripping arrangement consists of orthogonal pinned joints hung from the lever arm to prevent transmitting bending loads, and hardened steel bolted grips at the specimen upper end. The specimen's lower end is bolted directly to two strain-gaged aluminum plates which are in turn pinned to a threaded collar and bolt configuration used for applying preload to the specimen. The preload mechanism is secured to a 32-mm plate which is welded to the bottom of the fulcrum support structure and bolted to the isolation platform.

     d. Tests on graphite/epoxy and S2-glass/epoxy specimens were performed at cyclic frequencies ranging from 28 to 80 Hz (an underdesigned connecting bolt prevented higher frequencies) and specimen average composite tensile stress amplitudes σ_x^o ranging from about 7.5 MPa to about 25 MPa. Prestresses were kept at about 1.5 times the amplitude stress to avoid compressive loading. Stresses in the composite were kept well below levels which could cause matrix cracking in the specimens. Each specimen was allowed to cycle for a short time at the predetermined stress and frequency to allow grip setting and thermal equilibrium to be reached. Load cell output and specimen strain were fed to the ordinate and abscissa, respec-

41

tively, of an oscilloscope, and the resulting hysteresis loop photographed. Figure 41 shows typical hysteresis loops obtained. Note that the areas contained in the loops are relatively small. The area contained in each hysteresis loop was measured using a planimeter and the mechanical energy density per unit cycle was calculated. In addition, the composite volume-averaged stress deviator amplitude inner product, $\overline{S^o_{ij}S^o_{ij}}$, was calculated from equations (III-3,5,6,7) and Table 4. Fiber and matrix phase properties and composite properties used in the calculations are shown in Table 5. Test and calculation results are shown in Table 6.

    e. In order to determine material viscoelastic constants A and B for both graphite/epoxy and S2-glass/epoxy material systems, the energy dissipation density per cycle equation (III-16a) is written in the form

$$\frac{\overline{\omega S^o_{ij}S^o_{ij}}}{\overline{D}_c} = A + B\omega^2 \qquad (16b)$$

The quantity $\overline{S^o_{ij}S^o_{ij}}/\overline{D}_c$ was treated as the dependent variable and ω as the independent variable, and a linear regression analysis (reference (1)) was performed on the data. The result is a determination of A and B by a least-squares curve fit to the data and calculation of the correlation coefficient, an estimate of the "goodness of fit". It is noted that the least-squares curve fit is unaffected by the way the variables are structured; however, strictly speaking, one should not combine dependent with independent variables for a regression analysis as was done with $\overline{D}_c$ and $S^o_{ij}S^o_{ij}$. Therefore, the correlation coefficients obtained for the equation (III-16b) are not valid, and are not presented here.

    f. Results of the least-squares curve fit to the data and resulting values of A and B are shown in Figure 42 for graphite/epoxy and Figure 43 for S2-glass/epoxy. Measured values of $\overline{D}_c$ from hysteresis loops are plotted against least-squares curve fit predictions. The 45° line represents perfect correlation. Note that there is considerable scatter to the data, most likely caused by the difficulty in obtaining accurate planimeter measurements of the areas. The errors are estimated to be as high as +100% and -50%. Even with this high probable error, the correlation is good.

g. With the viscoelastic constants A and B determined from the experimental data, an analysis can be performed which determines the maximum energy dissipation rate density, $\dot{D}$, for a given value of applied composite stress. From equation (III-17a), it can be seen that as the cyclic frequency ω approaches infinity, the energy dissipation rate density approaches an upper limit given by

$$\dot{D}_{max} = \overline{S^o_{ij}S^o_{ij}}/2\pi B \qquad (III-19)$$

Values for this maximum energy dissipation rate density are shown in Table 7 for the two materials tested. Obviously, there will be an optimum finite frequency where most of $\dot{D}_{max}$ will be obtained (it is impossible to cycle at $\omega = \infty$). If the desired dissipation rate density is arbitrarily chosen to be 90% of $\dot{D}_{max}$, the cyclic frequency ω_{90} at which this dissipation rate density will occur is found from

$$0.9\dot{D}_{max} = 0.9 \ \overline{S^o_{ij}S^o_{ij}}/2\pi B = \omega_{90}^2 \ \overline{S^o_{ij}S^o_{ij}}/2\pi(A+B\omega_{90}^2)$$

to be

$$\omega_{90} = 3(A/B)^{\frac{1}{2}}$$

Values of $0.9\dot{D}_{max}$ and corresponding cyclic frequencies are shown in Table 7 compared to typical values obtained from a test machine capable of 35-Hz frequency. It is seen that the higher levels of energy dissipation rate density are much larger than those obtained from a typical cyclic test machine. This has implications for SGTF thermographic NDT as will be seen later.

C. EVALUATION OF CYCLICALLY LOADED GRAPHITE/EPOXY AND GLASS/EPOXY

1. SCOPE OF THE EVALUATION. It was necessary to determine whether or not heat generation in composites due to viscoelastic matrix behavior is adequate for thermal imaging, and to insure that the heat generated near flaws is not due to material damage. To accomplish this task, one each of 2.5-cm-wide x 150-cm gage length samples of 8-ply [0/±45/90] graphite/epoxy and S2-glass/epoxy were drilled with a 6-mm through-hole. The samples were cycled at 34 Hz at loads below those which would cause any composite damage. Thermovideographs were taken of the resulting temperature increase

43

of the specimens. Concurrently, the viscoelastic heat energy generated
was calculated for both specimens using the equations previously presented
and the general procedure outlined in Figure 36. If analysis agrees well
with experiment, then the heat generated is due mainly to viscoelasticity
and not to material damage. If experimental specimen surface temperatures
are higher than predicted near the hole, then material damage may be
creating significant heat, thus rendering SGTF methods unsuitable for
Naval aerostructure thermographic NDT.

2. **FINITE ELEMENT STRESS ANALYSIS**. The 8 ply $[0/\pm45/90]_s$ layup is
elastically and thermally isotropic. Elastic and thermal properties of
the $[0/\pm45/90]_s$ graphite/epoxy and S2-glass/epoxy laminates were calculated
using laminate analysis techniques (the laminate analysis computer program
ELAN was used). Table 8 presents layer and laminate thermoelastic proper-
ties for the materials used. Note that the Poisson's ratios for the quasi-
isotropic graphite/epoxy and S2-glass/epoxy are the same. As a result,
the stress distribution in the test specimens containing the 6-mm through
hole will be similar and will differ only by a constant which is the ratio
of the applied stress on the two specimens. Only one specimen, therefore,
need be analyzed for stress distribution. The tensile specimen containing
the hole was analyzed by the SAP4 finite element computer code. A relatively
coarse grid was utilized since the object is to obtain temperature dis-
tributions, not peak stresses. The finite element grid representing one
quarter of the specimen due to double symmetry is presented in Figure 44.
The analysis was performed for a one MPa applied laminate far-field stress,
and results are presented in Figure 45 averaged over adjacent triangular
elements. Since the applied laminate stress amplitudes in the actual tests
were 13.4 MPa for graphite/epoxy and 10.7 MPa for the S2-glass/epoxy, the
results in Figure 45 were multiplied by 13.4 and 10.7, respectively, to
obtain average laminate stresses.

3. **LAMINATE ANALYSIS FOR LAYER STRESSES**. The laminate stress analysis
results needed to be analyzed for layer stresses in order that the heat
generation/energy dissipation density equations could be used. Therefore,
a constant strain laminate analysis was performed on all averaged square
element stress results for both materials. Again, the ELAN computer code

44

was used; this time, to obtain composite stresses in each layer of the $[0/\pm45/90]_s$ laminates.

4. **HEAT GENERATION PREDICTION.** The layer stresses were used in equations III-3,5,6,7 and Table 4 to obtain $S_{ij}^o S_{ij}^o$ for each layer of each element. The computed values of $S_{ij}^o S_{ij}^o$ were then substituted, with values of A and B found during the material calibration tests and a cyclic frequency of 34 Hz (corresponding to the test frequency), into the energy dissipation rate density equation (III-17a). The results were heat energy generation rate density (equal to energy dissipation rate density) for each layer of each element in the cyclically loaded laminate. In order to provide input to the heat transfer analysis used to predict surface temperatures, heating rate density was averaged over layers of a given element. Results are shown in Figure 46 for graphite/epoxy and S2-glass/epoxy.

5. **SURFACE TEMPERATURE PREDICTION.** For both the graphite/epoxy and S2-glass/epoxy samples, a 51 node model was created for one quarter of the sample. This grid system was possible because of the symmetry in the sample. Figure 47 presents the nodal pattern and significant dimensions of the model. Heat generation density rates from Figure 46 were used with the thermal properties in Table 8 in the heat transfer analysis to predict surface temperatures. Results show that although the S2-glass/epoxy and graphite/epoxy samples are predicted to heat 0.9°C and 0.1°C above room temperature, respectively, less than 0.1°C temperature rise is predicted in the vicinity of the hole for both materials. Thus, a detectable hot spot due to the stress concentration effect is not likely to be seen in the thermovideographs of these particular cyclically loaded specimens.

6. **EXPERIMENTAL RESULTS**

a. The graphite/epoxy and S2-glass/epoxy samples containing the 6-mm dia through-hole were cycled for 30 minutes each at 34 Hz and tensile stress amplitudes $\bar{\sigma}_x$ equal to 13.1 MPa and 10.7 MPa, respectively. Figure 48a is a thermovideograph of the S2-glass/epoxy specimen at room temperature. Black dot in the center is the 6-mm hole. Note that the specimen temperature appears about 0.1°C cooler around the hole than the background. Figure 48b is a thermovideograph of the same specimen after cycling

45

for 30 minutes. Two aspects of the figure are noteworthy. First, the lavender/red region in the center is about 0.6°C higher than the background, showing that the specimen as a whole has increased about 0.7°C during the cyclic loading. Second, there is no measurable temperature difference between the area immediately around the hole and the surrounding region. The graphite/epoxy tests showed similar results (Figures 48c, d). Before cycling, the region surrounding the hole appears about 0.2°C cooler than the control strip to the right; after cycling, the specimen appears about 0.1°C cooler than the control. This indicates that the specimen has heated about 0.1°C. In the immediate vicinity of the hole, there is slight evidence of a hot ring, but its magnitude is less than 0.1°C and is therefore below the resolution of the infrared camera. These results agree well with the predictions of the heat transfer analysis, indicating that the heat being generated is due to viscoelastic behavior only, and not to continued material damage due to cyclic loading.

b. It is recognized that through-holes and partial through-holes are only approximations to the damage which typically occurs in composite laminates due to impact loading. Actual nonvisible damage (reference (j)) consists of delaminations and possible fiber breakage. To see if such damage could generate hot spots visible in thermovideographs, both the S2-glass/epoxy and the graphite/epoxy sample were impacted by a blunt object several times directly around the hole. Visible delaminations resulted in the hole region. The samples were cycled for 30 minutes at the previous load levels, and thermovideographs taken. Figures 49a and b present the results. There is a readily visible set of hot spots around the hole in S2-glass/epoxy, with temperatures as high as 0.2°C above the surrounding area. For graphite/epoxy, the result is less dramatic, but present nevertheless, with a temperature difference of about 0.1°C.

7. DISCUSSION

a. The results of the SGTF study show that at cyclic stress levels below those which can cause damage in composite laminates, the heat generated is caused by viscoelastic behavior and not by continuing material damage due to cyclic loading. However, temperatures were not significantly

higher during cyclic loading around a 6-mm-dia hole drilled in 25-mm-wide tensile specimens of S2-glass/epoxy and graphite/epoxy. This is probably due to the relatively low levels of heat generated during the tests, and would most likely be different if the cyclic frequency were high enough to produce heat energy close to the maximum $\overline{D}_{max}$. In fact, as seen in Table 7, the value of $0.9D_{max}$ is eleven times D_{35} for graphite/epoxy, and more than three times larger for S2-glass/epoxy. It remains to be seen whether this heat is at a high enough level to produce a hot spot where there is no delamination.

b. The preceding discussion concerning magnitude of heat generation required for defects not containing cracks or delaminations may be entirely academic, because nearly all nonvisible impact type damage does create cracks or delaminations. As illustrated by the SGTF tests performed on impacted specimens with holes, the surface temperature near holes is considerably higher than without delaminations. The reason for the higher heat generation is probably frictional heat generated between delaminated and cracked surfaces. This is reinforced by the preliminary study in reference (a) which showed no visible heat in a slowly cycled unidirectional specimen of graphite/epoxy containing a 6-mm through-hole, until two large axial cracks developed. There was considerable heat generated by rubbing of the cracks long after the cracks occurred. (Figure 50). It is also noted that Reifsnider and co-workers (reference (k)) have been able to generate heat in delaminations by applying very low level ultrasonic excitation. The heat occurs only at a specific (high) frequency, and at such low load levels, that it cannot be viscoelastic heat. Friction between interfaces is therefore concluded to be the source of heat for their tests.

D. FEASIBILITY ASSESSMENT OF THE SGTF METHOD. The present study has shown that detectable heat is generated in composite materials due to viscoelastic matrix behavior and frictional rubbing of interfaces during cyclic loading. This heat is generated at load levels which should not cause material damage in the composites. Therefore the SGTF method is a safe one for structural composites. Through-holes without delaminations cannot be detected at 35-Hz cyclic frequency, but considerably more heat can be generated at a few hundred Hz, and it is possible that such defects

can be detected at the higher frequencies. In any event, composite defects caused by impact have cracks or delaminations associated with them; and cracks and delaminations can produce large amounts of heat due to relative motion of frictional interfaces. It is concluded that the SGTF method is feasible, but determination of the range of types and sizes of defects is necessary before a final decision can be made concerning its advantages and disadvantages compared to the EATF method. At present, the EATF appears to have the advantage of simplicity of heat source and application technique, but it is not known if SGTF methods can detect flaws which are not detectable by EATF methods and vice-versa.

E. ULTRASONIC STRESS GENERATION METHODS

1. A brief investigation was conducted into the use of ultrasonic exciters as a stress generated heat method. There are two ways that the ultrasonic exciter can be used: as a high frequency stress applicator, and as a flaw natural frequency exciter.

2. The only known work to date using ultrasonic devices to generate visible heat patterns in composites has been performed by Henneke, Reifsnide., and co-workers at VPI (reference (k)). They report the use of an ultrasonic exciter to which is attached a panel of composite material containing delaminations. When certain ultrasonic frequencies are reached, heat is generated at the delamination site. Thermovideographs of the area clearly show the presence of the delamination and its shape. A heat transfer analysis was conducted on the composite assuming that the delamination interface is a heat source. Results show that the surface temperatures predicted agree well with the thermovideographs. This outcome is consistent with frictional surface heat generation: If it were due to viscoelastic behavior, only the edges of the delamination would heat up, not the whole interface. In addition, the heat generated would increase to a maximum at several hundred to 1000 Hz, then remain nearly constant with increase in cyclic frequency. Since the heat was generated at only certain high frequencies, it is probably due to excitation of a delamination natural frequency.

3. Since cyclic stress frequency for 90% of maximum viscoelastic heat generation is in the sonic range, going to ultrasonic frequencies for

viscoelastic heat generation is not warranted. Also, considerably larger energy inputs would be required to ultrasonically generate stresses high enough for thermographically visible viscoelastic heat generation.

4. The only viable way to use ultrasonic methods for SGTF flaw detection, then, is to excite natural frequencies of vibration of delaminated regions in composites. Since the units tested at VPI were used on a sample not greater than 30 cm square, it appears that a unit capable of testing large areas of aerostructural composite surface may need to be of considerably greater size. Further investigation into the ultrasonic SGTF technique is warranted in order to fully determine its limitations.

IV. SUMMARY AND CONCLUSIONS

A. The present Phase I study was critical, as it decided whether or not SGTF techniques can be used for thermographic NDE, made a definitive assessment of the suitability of EATF methods to detect different types of flaws in the most important aerostructural materials, and evaluated the effects of surface reflectivity and emissivity.

B. EXTERNALLY APPLIED THERMAL FIELD (EATF) DEVELOPMENT AND EVALUATION

1. The developmental effort performed in Phase I was to determine the size and location of flaws that can be detected in various thicknesses of structural materials, and to evaluate different methods and magnitudes of external heat application. In addition, limitations on infrared camera sensitivities were examined; and the effects of surface reflectivity and emissivity caused by paints, abrasions, etc., were evaluated. The work was performed using a closely coordinated experimental/analytical approach where a test program was conducted on selected samples of flawed and un-flawed graphite/epoxy, glass/epoxy, Kevlar 49/epoxy, and aluminum, and correlated with a heat transfer/thermal analysis that can be run with any size and type of basic structural material or flaw.

2. The test program consisted of applying external heat to test samples containing flaws not visible to the naked eye, and observing and photographically recording thermal surface temperature perturbations with the Navy's IGA Thermovision infrared camera. Material thicknesses were varied up to 5 mm, and flaw types included delaminations and partial through-holes which simulate manufacturing and impact-induced defects. Several types of heat sources were evaluated, including forced hot air, radiation heating, and conductive heating with thermal blankets.

3. Conclusions from the test and analysis program are as follows:

a. Simulated delaminations and partial-through-holes can be detected in sizes as small as 6 mm across and located more than halfway through 32-ply samples of graphite/epoxy and 16-ply samples of glass/epoxy mater-ials. As yet, the upper limit on sample thickness has not been found. There appears to be no upper limit on detectable flaw size, but there is probably a lower limit on flaw size.

50

b. Laminate anisotropy appears to be unimportant to quality and duration of thermal images: virtually identical results have been obtained with radiative heat sources on [0/±45/90] (thermally isotropic) and [0_2/±45] (thermally anisotropic) graphite/epoxy structural composites.

c. EATF heat generation using variable energy radiant heat sources has been found to be the best method for flaw detection. Use of thermal blankets in the form of electrical resistance strip heaters produced poor results. It has been concluded that the so-called "conduction" method of heat application (heating a remote section of structure and allowing heat to conduct along the surface to be examined) is inappropriate for detection of delaminations and partial-through-holes (impact damage).

d. Radiant heat source application times of up to one minute, and radiant energy of up to one watt per square centimeter may be required to detect flaws in typical Navy aerostructures made from composites.

e. The effects of Navy aviation structural surfaces on reliability of results can be significant:

(1) Aluminum surfaces painted with polymeric Navy aviation paint show "hot spots" under infrared thermography which are due to uneven paint thickness, and which could be misinterpreted as a delamination or flaw in a graphite/aluminum structure. Painted aluminum matrix composite structures, therefore, are probably not good candidates for thermographic NDE. Paint thickness variations do not cause hot spots when applied to polymeric matrix composites such as graphite/epoxy or Kevlar/epoxy.

(2) Tests have shown that reflection of a spurious heat source from a naval aviation painted surface can also be misinterpreted as a flaw by the infrared camera. Structural surfaces to be examined must therefore be shielded from sources of possible heat reflection such as sun, light bulbs, and engine exhausts.

(3) Black, orange, and white Navy aviation paint appear to be at different surface temperatures, probably due to different emissivities. Black appears significantly hotter than orange or white. Orange and white appear very close in temperature, but the effect is still visible. Paint color borders may therefore be visible on the thermovision screen while examining surfaces for flaws. However, since they are

easily seen by the examiner, they should provide no source of error in the examining process. Even the least qualified sailor will recognize that flaws do not come in the shape of "NO STEP".

(4) Abraded or soiled surfaces can appear as cool or hot spots even in the absence of thermal gradients. These effects can be eliminated or reduced by making sure that surfaces to be examined are clean and unroughened prior to examination.

C. STRESS GENERATED THERMAL FIELD (SGTF) DEVELOPMENT AND EVALUATION

1. It was known that partial-through-holes, notches, and delaminations can be detected by SGTF methods in glass/epoxy, boron/epoxy, and graphite/epoxy structures. However, it was not known whether composite structures can be damaged by the levels of cyclic stress application necessary to generate heat for thermal flaw detection. Further, the range of stress amplitude versus cyclic frequency necessary to get a visible stress-generated thermal image for different types of materials was not known. As a result, Phase I developmental activity determined the levels of stress and frequency which can be applied to structural materials without causing structural damage.

2. An analysis was performed which determined stresses in matrix material for a given set of in-plane composite laminate stresses. This analysis was used with a semi-empirical equation derived from linear viscoelasticity to determine energy dissipated in the composite matrix material for different values of applied composite stress and cyclic frequency. The empirical equation was calibrated by cyclic frequency tests run on unflawed [±45] specimens of graphite/epoxy and glass/epoxy. Hysteresis loops formed during the cyclic stress tests were due only to matrix viscoelastic behavior, and not to damage propagation or fracture. The area contained in these hysteresis loops represents the energy dissipated as heat during cycling, and was used to determine the empirical constants in the equation of heat generation as a function of applied cyclic stress level and cyclic frequency.

3. With the experimentally determined equation for heat generation in composites, it was possible to calculate the heat generated near structural flaws due to viscoelastic behavior only (no damage). Cyclic stress

52

tests were run on specimens of [0/±45/90] graphite/epoxy and glass/epoxy containing 6-mm through-holes, and measured surface temperatures were compared to those which would be caused by viscoelastic behavior only (no damage). Cyclic tests were also run on graphite/epoxy and glass/epoxy samples where delaminations had been induced around the holes by impacting with a blunt object.

4. Conclusions drawn from the analytical and experimental studies are as follows:

a. In all tests performed, load levels were maintained less than those required to cause breakage of fibers or cracking of matrix material. The measured heat agreed reasonably closely with the calculated values, indicating that viscoelastic behavior of the material, and not material damage, was causing the heat generated in the composites.

b. Temperatures around the holes, however, were not significantly higher than the surrounding regions of the specimens. This is probably due to the relatively low levels of heat generated during the tests which were performed at a cyclic frequency of 35 Hz. Calculations show that three to ten times more heat would be generated at frequencies of 160 to 350 Hz for S2-glass/epoxy and graphite/epoxy, respectively. These higher levels of heat may be adequate to produce a thermographically visible heat pattern.

c. Considerably higher heat is generated by frictional interplay between delamination or crack surfaces than is generated by material viscoelastic response. Since nearly all impact-type damage results in delaminations and/or matrix cracks, viscoelastic heat may not be required to generate visible heat patterns.

d. SGTF techniques appear viable to develop detectable "hot spots" in flawed composites without degrading material or reducing structural lifetime; however, further tests on actual damage sites at frequencies of several hundred Hz are required to resolve the situation.

e. Investigations into the use of ultrasonics as an EATF or SGTF heat generation technique indicate that ultrasound methods may not be fruitful due to the size and complexity of the unit necessary to generate sufficient energy to cover a large surface area; however, further study is warranted.

C. <u>GENERAL</u>

1. Due to conductivity effects, graphite/epoxy is a more difficult material than S2-glass/epoxy in which to develop visible thermal patterns by both EATF and SGTF techniques. For graphite/epoxy with EATF techniques, visibility times on the order of a fraction of a second to one minute have been observed. However, flaws can be detected provided that the operator utilizes a high heat input and is familiar with the type of thermal images to be expected. S2-glass/epoxy has longer image visibility with several seconds to more than a minute for EATF heating.

2. Infrared camera sensitivities required for flaw detection by EATF methods range from $2^{\circ}C$ full scale to $50^{\circ}C$ (detectable temperature rises of $0.2^{\circ}C$ to $5^{\circ}C$). Sensitivities for SGTF methods range from $1^{\circ}C$ to $5^{\circ}C$ (detectable temperature rises of $0.1^{\circ}C$ to $0.5^{\circ}C$).

V. CURRENT STATUS AND RECOMMENDATIONS

It has been demonstrated that EATF radiation heating techniques can detect delaminations and partial-through-holes in structural composites, and that SGTF heat generation may produce significant thermal patterns to allow flaw detection without creating material damage or reducing component lifetime. While considerable knowledge has been gained concerning capabilities, limitations, and test techniques required for EATF thermographic NDE, it still remains to establish limits on detection capabilities and flaw resolution for actual defects rather than simulations; and to investigate the effects of backup structures such as honeycomb, spars, and/or ribs. For the SGTF technique, it is now necessary to determine levels of stress and cyclic frequency required to generate detectable thermal patterns near impact damage sites and delaminations, and to investigate methods of safely applying high frequency cyclic loading to aerostructural components. Radiant heat source and infrared detector equipment guidelines also need to be developed further to enable equipment development if thermographic NDE is adopted for Navy aviation ground support usage.

VI. REFERENCES

(a) McLaughlin, P.V., Jr., McAssey, E.V., Jr., and Deitrich, R.C., "Non-Destructive Examination of Fiber Composite Structures by Thermal Field Techniques", NDT International, Vol. 13, Apr 1980, p. 56.
See also: same authors, "Aerostructure Nondestructive Evaluation by Thermal Field Techniques", Report NAEC-92-131, 1 Nov 1979.

(b) Holman, J.P., Heat Transfer, 4th Ed., McGraw-Hill, 1976.

(c) Adams, D.F., Dones, D.R., and Thomas, R.L., "Mechanical Behavior of Fiber-Reinforced Composite Materials", AFML-TR-67-96, 1967.

(d) Pickett, G., "Elastic Moduli of Fiber Reinforced Plastic Composites", Chapter 2 in Fundamental Aspects of Fiber Reinforced Plastic Composites, R.T. Schwartz and H.S. Schwartz, eds., Interscience, 1968.

(e) Hashin, Z., and Rosen, B.W., "The Elastic Moduli of Fiber Reinforced Materials", Journal of Applied Mechanics, Vol. 31, 1964, p. 223.

(f) Hashin, Z., "Theory of Fiber Reinforced Materials", NASA CR-1974, Mar 1972.

(g) Emany, V.R., "Heat Generated in Fiber Composites Under Cyclic Loading", Thesis submitted in partial fulfillment of the requirements for the degree of Master of Mechanical Engineering, Department of Mechanical Engineering, in preparation.

(h) Flugge, W., Viscoelasticity, Blaisdell, 1967.

(i) Freund, John E., Mathematical Statistics, Prentice-Hall, 1962.

(j) Bhatia, N.M., "Impact Damage Tolerance of Thick Graphite-Epoxy Laminates", NADC-79-38-60, Jan 1979.
See also:
Gause, L.W., "Low Speed, Hard Object Impact on Thick Graphite-Epoxy Plates", NADC-78051-60, May 1978.
McQuillen, E.J., Gause, L.W., and Llorens, R.E., "Low Velocity Transverse Normal Impact of Graphite Epoxy Composite Laminates", Journal of Composite Materials, Vol. 10, Jan 1976, p. 79.
See also NADC-75119-30, Jun 1974.

(k) Reifsnider, K.L., and Stinchcomb, W.W., "New Methods of Mechanical Materials by Vibrothermography", in Nondestructive Evaluation and Flaw Criticality for Composite Materials, ASTM STP 696, 1979

Table 1. AGA Thermovision System 680/102B Color Screen
Temperatures and Sensitivities

Camera Sensitivity (Full Scale Temp. Range)	Temperature Increase Above Black Setting, deg. C.									
	1	2	5	10	20	50	100	200	500	1000
Screen Color:										
Black	0	0	0	0	0	0	0	0	0	0
Dark Blue	0.1	0.2	0.5	1	2	5	10	20	50	100
Blue Green	0.2	0.4	1.0	2	4	10	20	40	100	200
Green	0.3	0.6	1.5	3	6	15	30	60	150	300
Light Blue	0.4	0.8	2.0	4	8	20	40	80	200	400
Purple	0.5	1.0	2.5	5	10	25	50	100	250	500
Lavender	0.6	1.2	3.0	6	12	30	60	120	300	600
Red	0.7	1.4	3.5	7	14	35	70	140	350	700
Orange	0.8	1.6	4.0	8	16	40	80	160	400	800
Yellow	0.9	1.8	4.5	9	18	45	90	180	450	900
White	1.0 and above	2.0 and above	5.0 and above	10 and above	20 and above	50 and above	100 and above	200 and above	500 and above	1000 and above

Table 2.   Aluminum Surface Finish Samples

SAMPLE	COLOR	PAINT THICKNESS (cm)
A	Black/White	.0038
B	Gray/White	.0038
C	Orange/White	.0038
D	Unpainted/White	.0051
E	White/White	.0051
F	White/White	.0051
G	White/White	.0064
H	White/White	.0038
I	White/White	.0038
J	White/White	.0038
K	White/White	.0038
L	White/White	.0064

Table 3. Fiber Composite Surface Finish Samples

SAMPLE	PAINT COLORS	PAINT CONFIGURATION
*Gr-A, K-A	White/White	**2W / 1W
Gr-B, K-B	Black/White	1B / 1W
Gr-C, K-C	Orange/White	1O / 1W
Gr-D, K-D	White	1W
Gr-E, K-E	White/Black	1W 1B
Gr-F, K-F	White/Black	1W 1B

*Gr=Unidirectional Graphite/Epoxy, K=Unidirectional Kevlar/Epoxy
**2=Two Coats, 1=One Coat, W=White Paint, O=Orange Paint, B=Black Paint

Table 4. Constants for Use in Determining Matrix Stresses Due to Transverse Normal Composite Stress, Eq.(6).

k \ ℓ	$C_{k\ell}^{\epsilon}$						d_k^{ϵ}
	1	2	3	4	5	6	
1	1	$1/V_f$	V_f^2	V_f	0	0	1
2	0	$-\dfrac{(3-4\nu_m)}{(3-2\nu_m)V_f}$	$-2V_f^2$	$\dfrac{V_f}{1-2\nu_m}$	0	0	0
3	1	1	1	1	-1	-1	0
4	0	$-\dfrac{(3-4\nu_m)}{(3-2\nu_m)V_f}$	-2	$\dfrac{1}{1-2\nu_m}$	0	$\dfrac{3-4\nu_f}{3-2\nu_f}$	0
5	1	$\dfrac{3}{3-2\nu_m}$	-3	$\dfrac{1}{1-2\nu_m}$	$-\gamma$	$-\dfrac{3\gamma}{3-2\nu_f}$	0
6	0	$-\dfrac{1}{3-2\nu_m}$	2	$-\dfrac{1}{1-2\nu_m}$	0	$\dfrac{\gamma}{3-2\nu_f}$	0

$$\gamma = G_f/G_m$$

60

Table 5. Model Calibration Specimen Dimensions and Material Properties
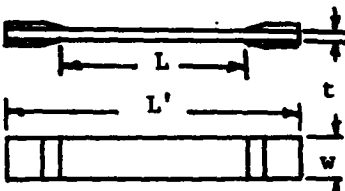
	Graphite/Epoxy	S2-Glass/Epoxy
SPECIMEN DIMENSIONS (mm):		
L'	200.	200.
L	150.	150.
w	19.1	25.4
t	1.32	0.98
FIBER PROPERTIES:		
Axial Young's Modulus (GPa)	234.	83.
Trans. Young's Modulus (GPa)	13.	83.
Axial Shear Modulus (GPa)	25.	22.
Axial Poisson Ratio ν_{12}	0.4	0.2
Trans. Poisson Ratio ν_{23}	0.3	0.3
MATRIX PROPERTIES:		
Young's Modulus (GPa)	3.7	3.9
Poisson Ratio	0.35	0.37
COMPOSITE PROPERTIES:		
[0] Layer:		
Axial Young's Modulus (GPa)	145	44.8
Trans. Young's Modulus (GPa)	9.6	11.7
Axial Shear Modulus (GPa)	4.8	3.9
Axial Poisson Ratio	0.3	0.3
Fiber Volume Fraction	0.62	0.53

Table 6. SGTF Calibration and Calculation Results – $[\pm 45]_s$ Graphite/Epoxy and S2-Glass/Epoxy

M T L	Cyclic Frequency ω, rad(Hz)	Tensile Stress Half Amplitude $\overline{\sigma}_x^{\,o}$, MPa	$\overline{S_{ij}^{o} S_{ij}^{o}}$ $(MPa)^2$	Energy Dissipation Rate/Cycle	
				Measured	Predicted*
				$\overline{D}_c$, N-m/m^{3}cycle	
GRAPHITE/EPOXY	176 (28)	5.09	4.9	132	123
		9.50	17.2	402	428
	217 (34.5)	5.09	4.9	216	147
		10.52	21.0	450	628
		10.18	19.7	734	588
		15.61	46.3	915	1384
	289 (46)	5.43	4.9	363	184
		11.20	23.8	1213	892
	361 (57.5)	5.43	5.6	488	243
		12.59	30.0	586	1300
		12.22	28.4	1765	1230
		24.61	115.0	5006	4990
	502 (80)	13.58	35.0	1839	1775
	A = 6.66 TPa/sec, B = 12.8 MPa-sec				
S2-GLASS/EPOXY	176 (28)	4.09	3.9	287	316
		7.84	14.5	867	1162
	217 (34.5)	4.78	5.4	582	479
		9.21	19.9	1201	1783
		7.50	13.2	1842	1184
		12.28	35.4	3044	3171
	289 (46)	4.78	5.4	723	.524
		9.55	21.4	3466	2096
	361 (57.5)	5.80	7.9	1023	783
		9.55	21.4	2372	2126
		11.94	33.5	3705	3322
		17.91	75.3	4281	7473
	A = 1.74 TPa/sec, B = 14.61 MPa-sec				

* From Empirical Equation $\overline{D}_c = \overline{S_{ij}^{o} S_{ij}^{o}}\ \omega / (A + B\omega^2)$

ω[rad/sec], $\overline{S_{ij}^{o} S_{ij}^{o}}$[(Pa)^2], A[Pa/sec], B[Pa-sec]

Table 7.   Heat Energy Dissipation Properties of Graphite/Epoxy
and S2-Glass/Epoxy Composites

Material	Max. Energy Dissipation Rate Density, $\dot{D}_{max}$ 10^{-8} S^{2*} N-m/m^{3}sec	$0.9\,\dot{D}_{max}$ 10^{-8} S^2 N-m/m^{3}sec	Cyclic Frequency for $0.9\dot{D}_{max}$ ω_{90} rad/sec(Hz)	Energy Dissipation Rate Density at 35 Hz $\dot{D}_{35}$ 10^{-8} S^2 N-m/m^{3}sec
Graphite /Epoxy	1.24	1.12	2162(344)	0.11
S2-Glass /Epoxy	1.09	0.98	1034(165)	0.31

$*S^2 = \overline{S^o_{ij}S^o_{ij}}$, $(Pa)^2$

Table 8. Composite Thermoelastic Properties Used in Calculating
          Surface Temperatures of [0/±45/90] Specimens with 6 mm
          Through-Holes.

	Graphite/Epoxy	S2 Glass/Epoxy
UNIDIRECTIONAL COMPOSITE PROPERTIES		
Elastic Properties - See Table 5		
Thermal Properties:		
Axial Thermal Conduct. (W/m^{o}C)	80.	0.7
Trans. Thermal Conduct. (W/m^{o}C)	0.5	0.3
[0/±45/90] LAMINATE PROPERTIES		
Elastic Properties:		
Young's Modulus (GPa)	55.	22.
Poisson's Ratio	0.31	0.31
Thermal Properties:		
In-plane Thermal Conduct. (W/m^{o}C)	40.	0.5
Trans. Thermal Conduct. (W/m^{o}C)	0.5	0.3
Specific Heat (J/kg^{o}C)	920	960
Density (kg/m^3)	1140	1880

(a)
A1
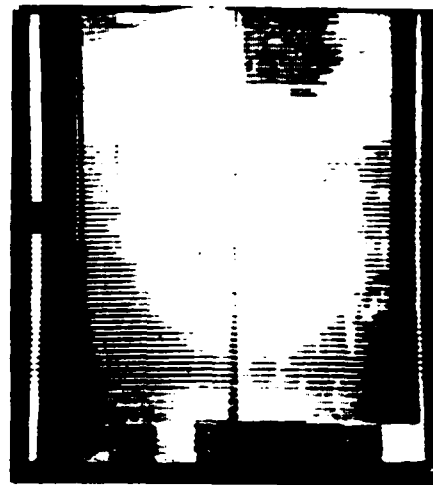
(b)
A2
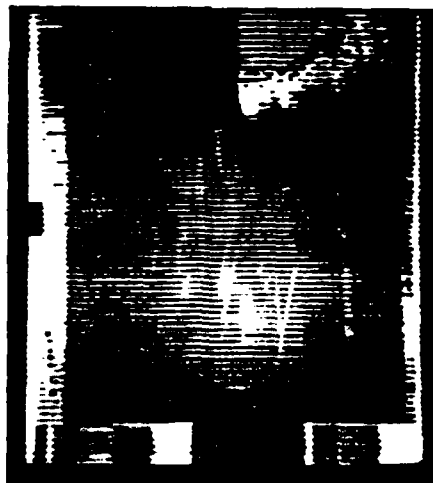
(c)
A4

SAMPLE A

Figure 1. Thermovideograph of Black/White Navy Aviation Paint on
Aluminum Plate. Black on Left and White On Right of All
Three Photos. (a) and (b) Show Emissivity Differences of
Black and White Paint. (c) Shows Light Bulb Reflection
At Upper Right. Note Streaks Due to Paint Nonuniformity.

(a)
C1

(b)
C4

SAMPLE C

Figure 2. Thermovideographs Of White/Orange Paint on Aluminum.
(a) Shows Color Effects and Thickness Variations, (b)
Shows Light Bulb Reflection. White Is On Left, Orange
Is On Right of Each Photo.

66
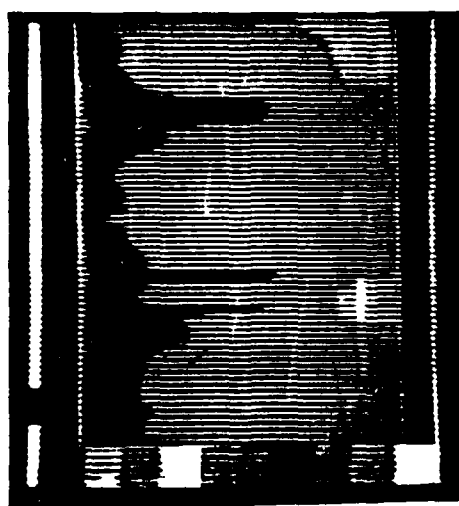
(a)
E1

(b)
E5

SAMPLE E

Figure 3. Thermovideographs of White Paint on Aluminum.
(a) Effects of Paint Thickness Variations,
(b) Reflection From Light Bulb.

67
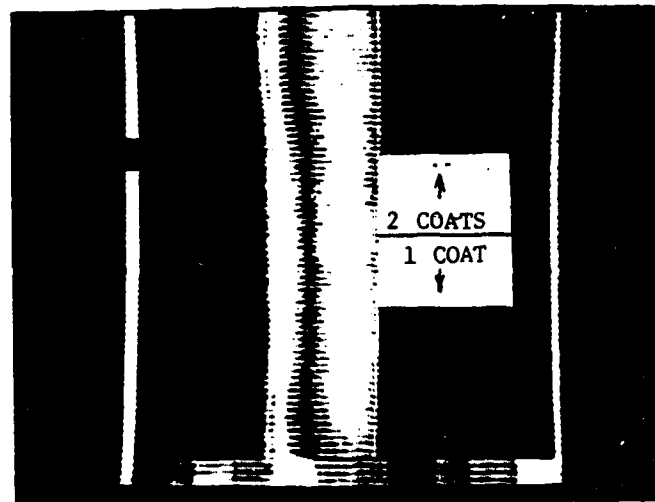
(A) Graphite/Epoxy (Sample Gr-A)
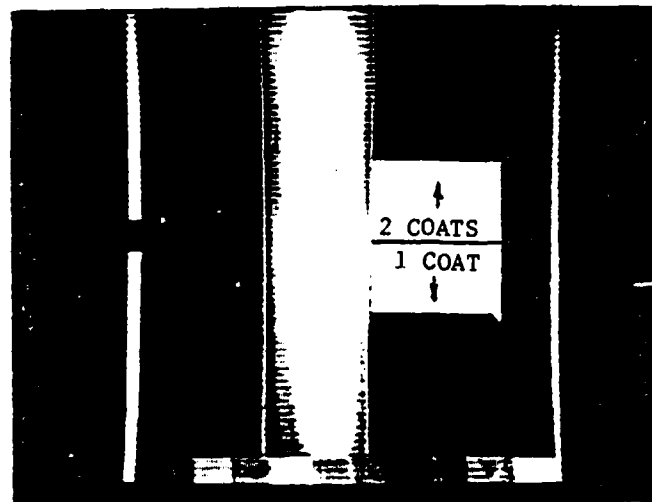
(B) Kevlar 49/Epoxy (Sample K-A)

Figure 4. Thermovideographs of Composite Plates with Single and Double
Coats of White Navy Aviation Paint.
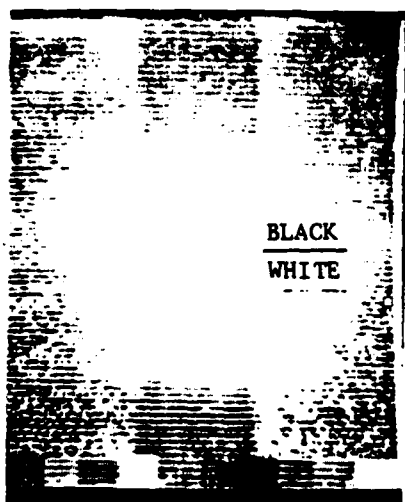
(a) K-B, Room Temperature
(Typical of all R.T. Samples)
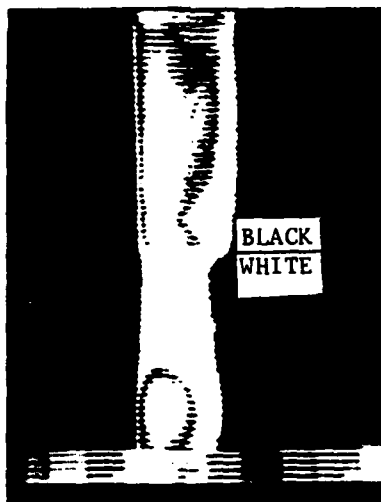
(b) K-B, Heated 60s.,
Cooled 30s.
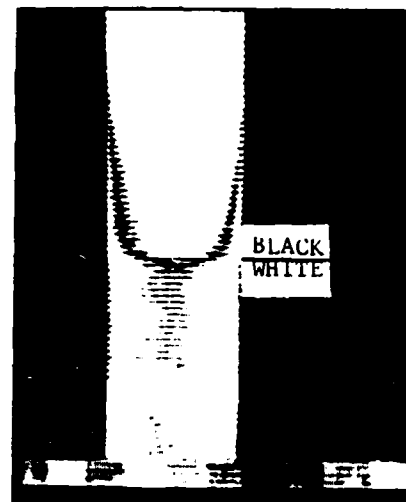
(c) Gr-B, Heated 30s.,
Cooled 30s.
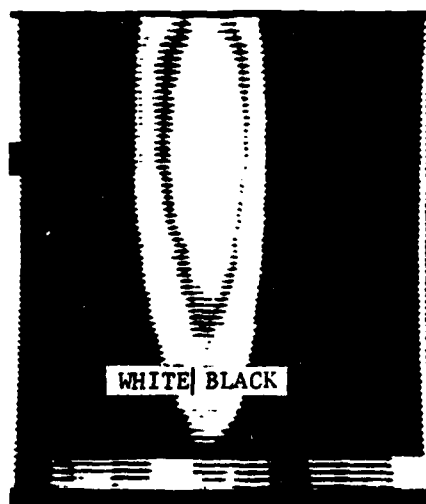
(d) K-E, Heated 30s., Cooled 120s.
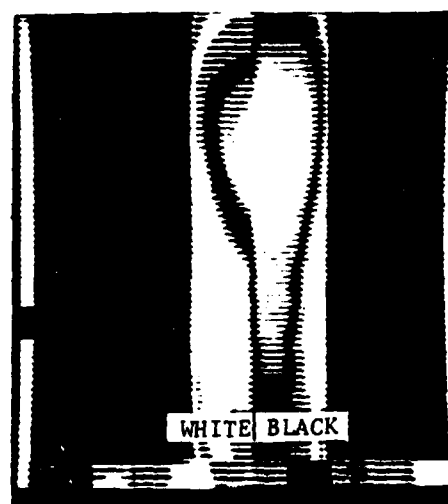
(e) Gr-E, Heated 20s., Cooled 30s.

Figure 5.   Thermovideographs of Single Coats of Black and White Navy
Aviation Paint on Composite Plates.
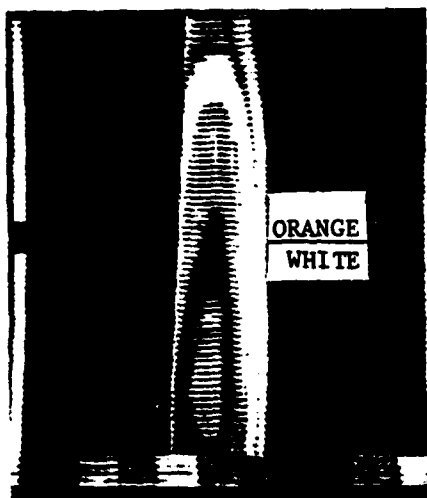
(a) K-C, Heated 40s., Cooled 70s.
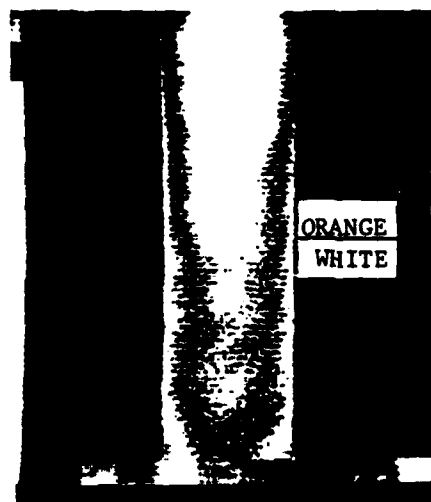
(b) Gr-C, Heated 30s., Cooled 120s.
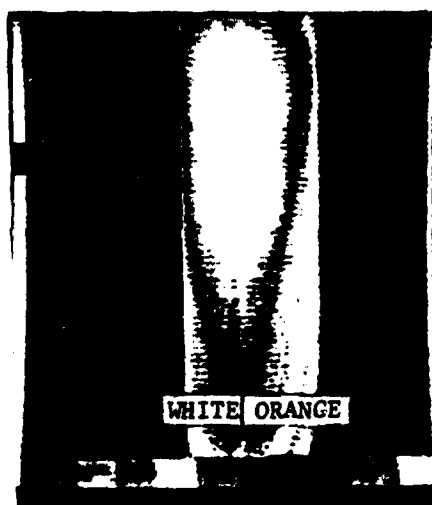
(c) K-F, Heated 30s., Cooled 150s.
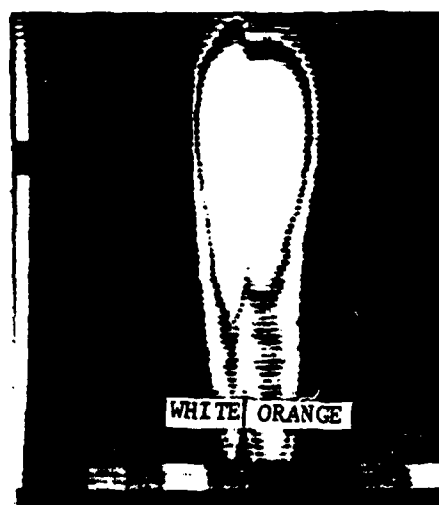
(d) Gr-F, Heated 30s., Cooled 25s.

Figure 6.   Thermovideographs of Single Coats of Orange and White Navy
Aviation Paint on Composite Plates.
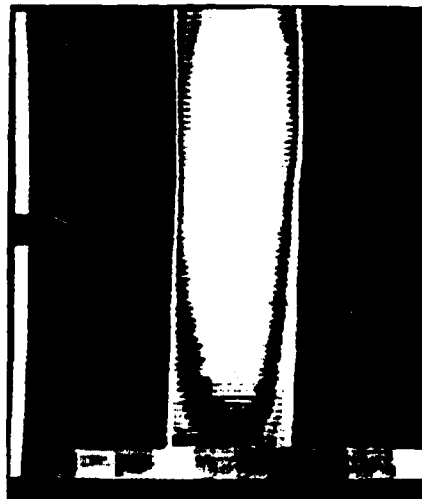
(a) K-D, Heated 40s., Cooled 180s.
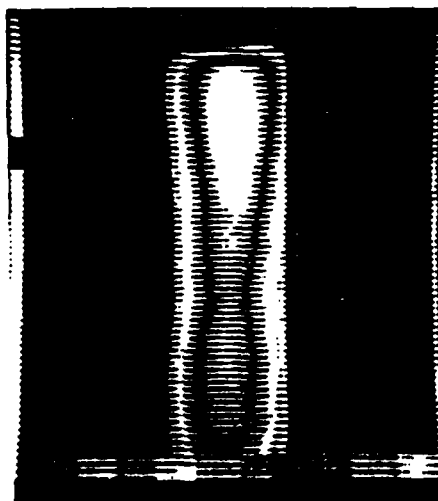
Heated 30s., Cooled 90s.   Heated 35s., Cooled 240s.
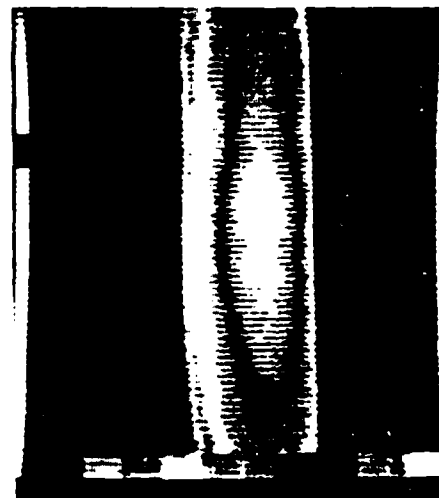
(b) Gr-D, Non-Uniformities are Due to Heat Application

Figure 7.   Thermovideographs of Single Coat of White Navy Aviation
            Paint on Composite Plates.
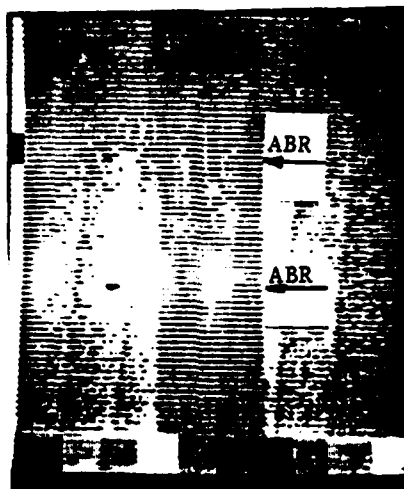
(a) Room Temperature
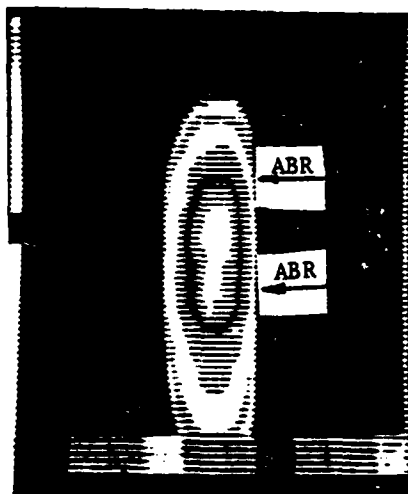
(b) Heated 60s., Cooled 30s.
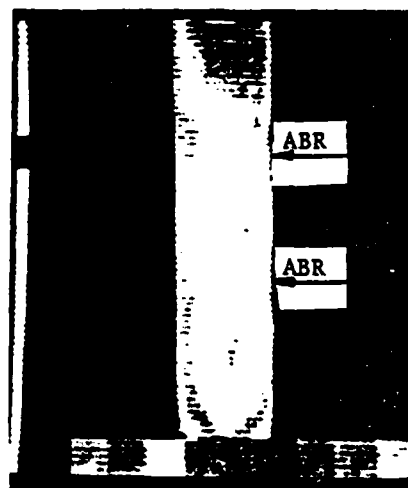
(c) Heated 60s., Cooled 420s.

Figure 8.   Thermovideographs of Sample Gr-D With Clean Abrasions on
White Paint.
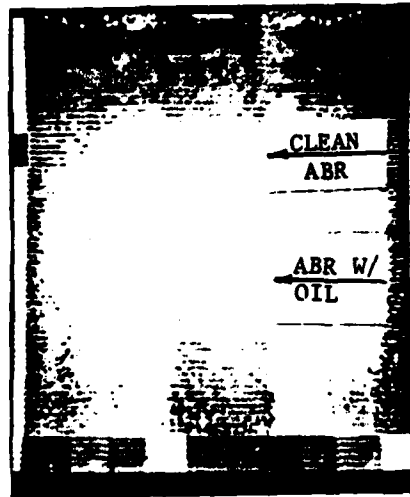
(a) Room Temperature
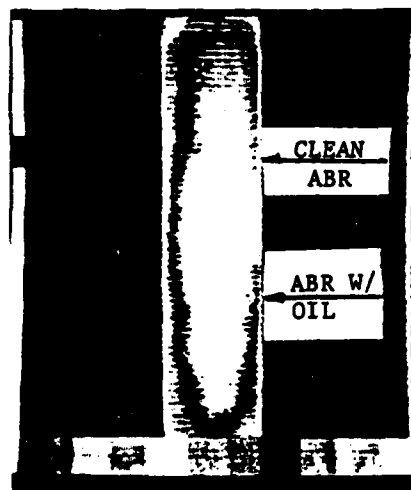
(b) Heated 60s., Cooled 223s.
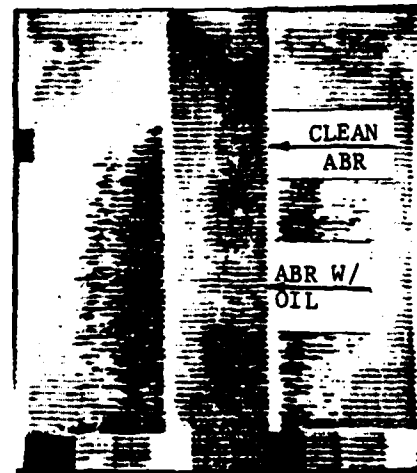
(c) Heated 60s., Cooled 390s.

Figure 9. Sample Gr-D with Clean Abrasion and Abrasion Covered with Coat of Clean Motor Oil.

73
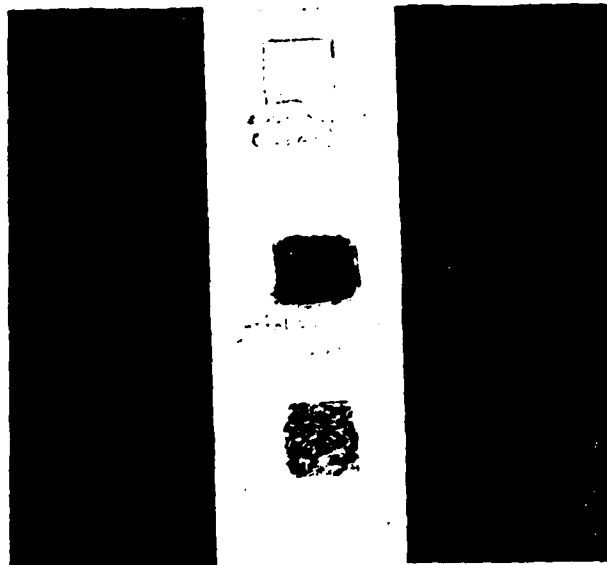
(a) Sample Head-On Showing Anomaly Locations
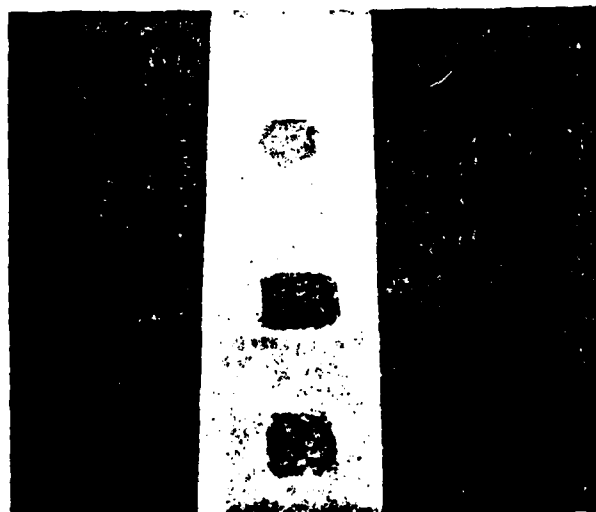
(b) Camera at 15° Angle Showing Light Reflection
From Glossy Paint Except in Abraded Area at
Top of Sample

Figure 10. Gr-D White Painted Sample Containing Clean Abrasion,
Abrasion with Heavy Coat of Soiled Grease, and Light
Coat of Soiled Grease on Glossy Surface.

(a) Room Temperature
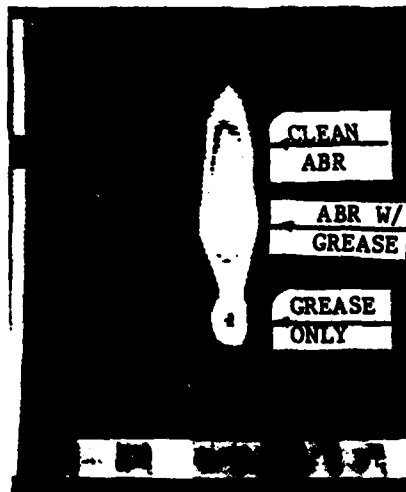
(b) Heated 60s., Cooled 30s.

Figure 11. Thermovideograph of Sample Containing Abrasions and Soiled
Grease on Navy Aviation Paint (Shown in Figure 10).

GRAPHITE EPOXY (.238 CM THK)
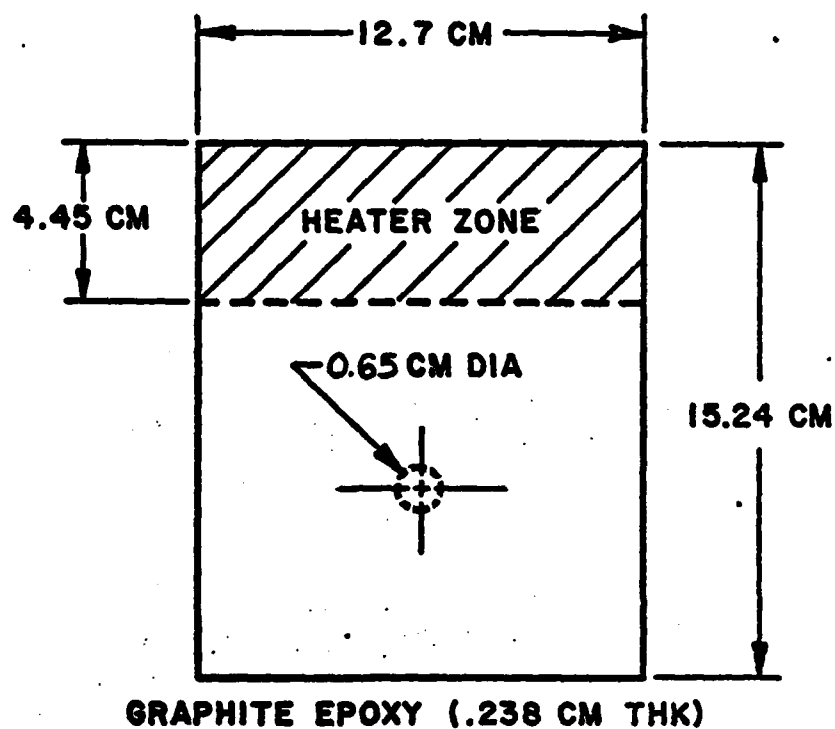
Figure 12. Schematic of Unidirectional Graphite/Epoxy Plate Containing
0.65-cm-Dia Partial-Through-Hole Used in Local Field
Application Method Evaluation.
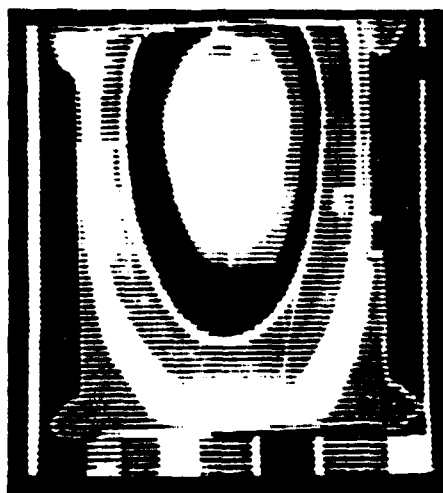
(a)
U1
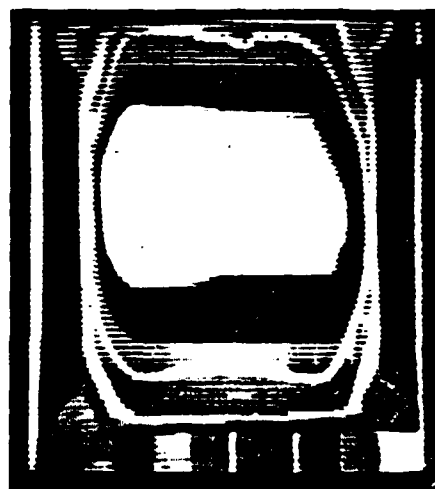
(b)
U2
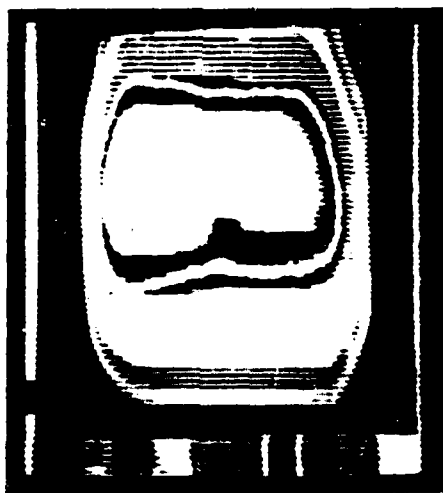
(c)
U3

HEAT-GUN APPLIED INPUT

Figure 13. Graphite/Epoxy Sample of Figure 12 Heated with Heat Gun.
(a) Vertical Heat Input. (b) Horizontal Heat Input.
(c) Vertical and Horizontal Heat Input. Note Perturbed
Isotherms In Middle Due to Partial-Through-Hole.

77
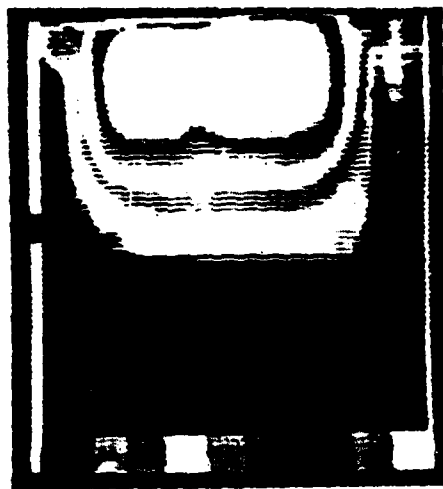
(a)
T1
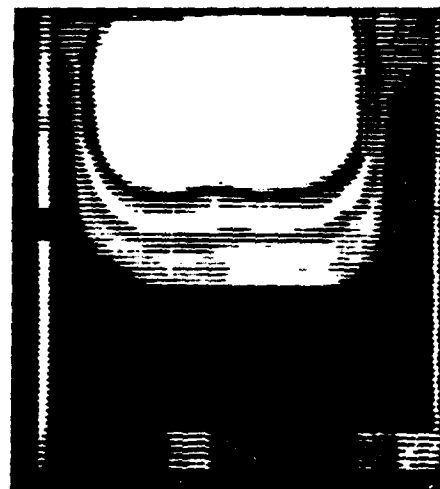
(b)
T3
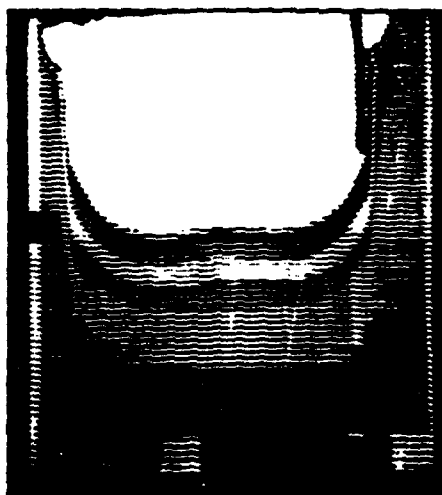
(c)
T5

HEATER APPLIED INPUTS

Figure 14. Graphite/Epoxy Sample of Figure 12 with Heat Applied By Surface Strip Heaters. (a) 1 Watt, (b) 4 Watt, and (c) 10 Watt Inputs.
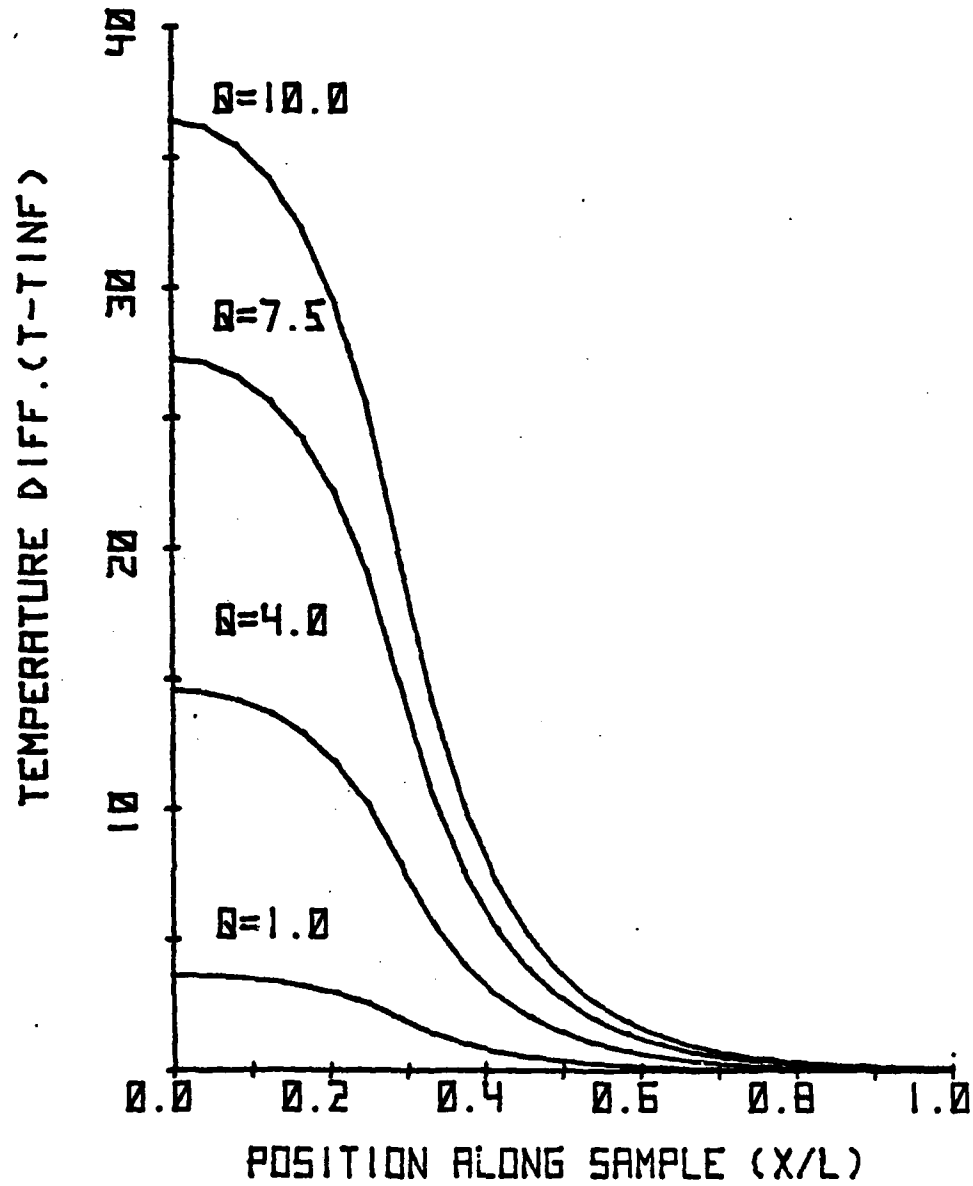
Figure 15. Theoretical Temperature Profile for Graphite/Epoxy Sample
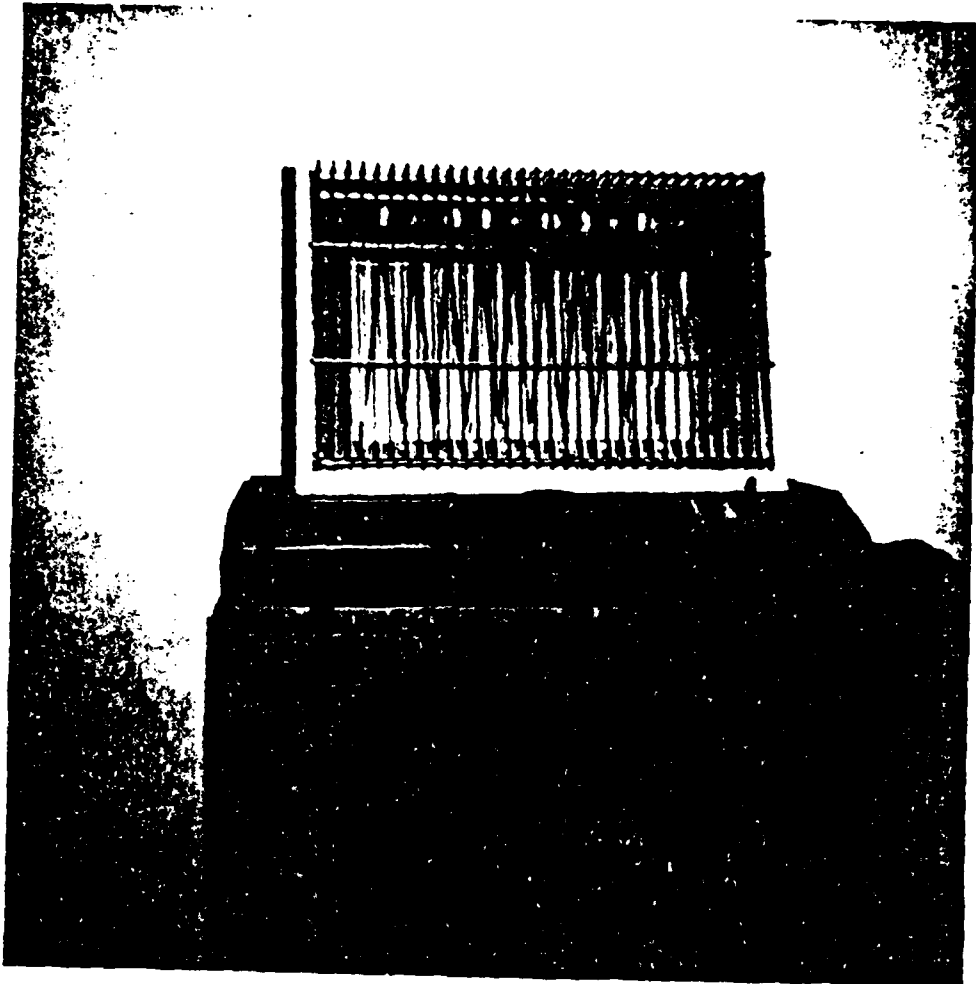
Figure 16. Photograph of 1320 W. Space Heater
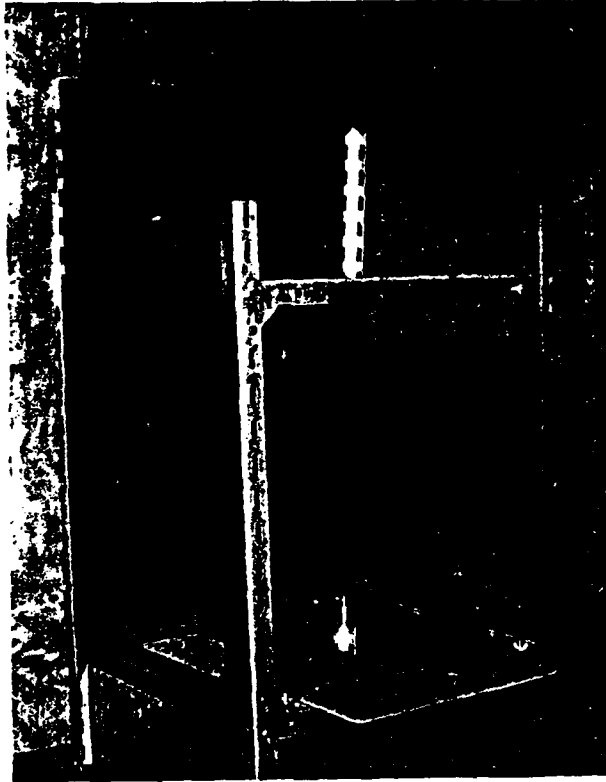
Figure 17.   EATF Sample Mounting and Test Fixture.

190.5	190.6	190.7	190.6	190.5
190.6	190.9	191.4	190.9	190.6
190.7	191.4	193.2	191.4	190.7
190.6	190.9	191.4	190.9	190.6
190.5	190.6	190.7	190.6	190.5

⊢— 25.4mm —⊣

190.3	190.4	190.4	190.4	190.3
190.4	190.5	190.7	190.5	190.4
190.4	190.7	191.3	190.7	190.4
190.4	190.5	190.7	190.5	190.4
190.3	190.4	190.4	190.4	190.3
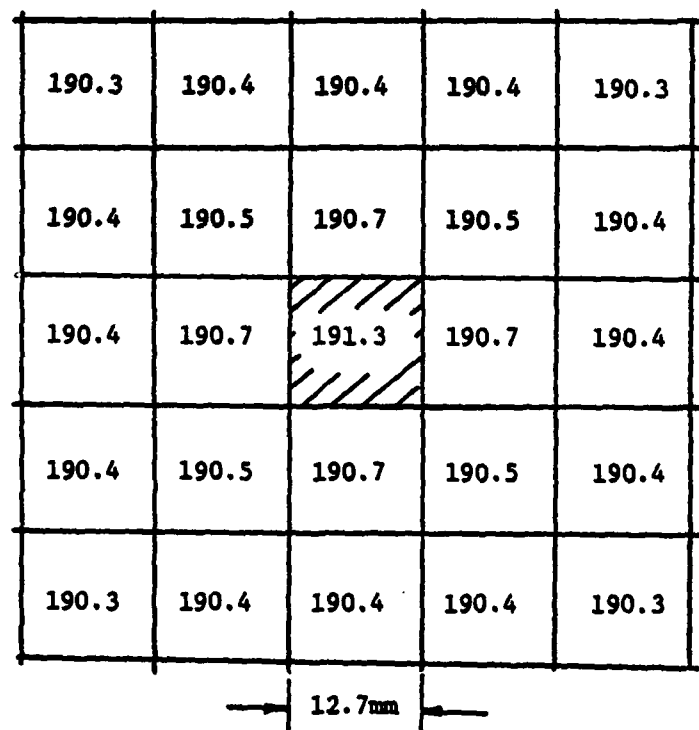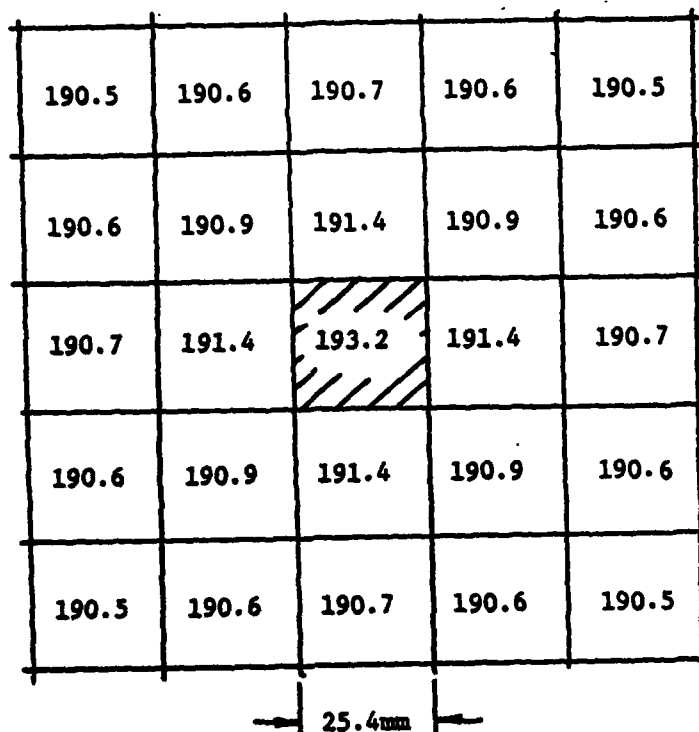
⊢— 12.7mm —⊣

Figure 18. Theoretical Surface Temperature Results of 25.4 and 12.7 mm
Square Delaminations at Mid-Plane of 32-Ply Graphite/Epoxy
Panel.
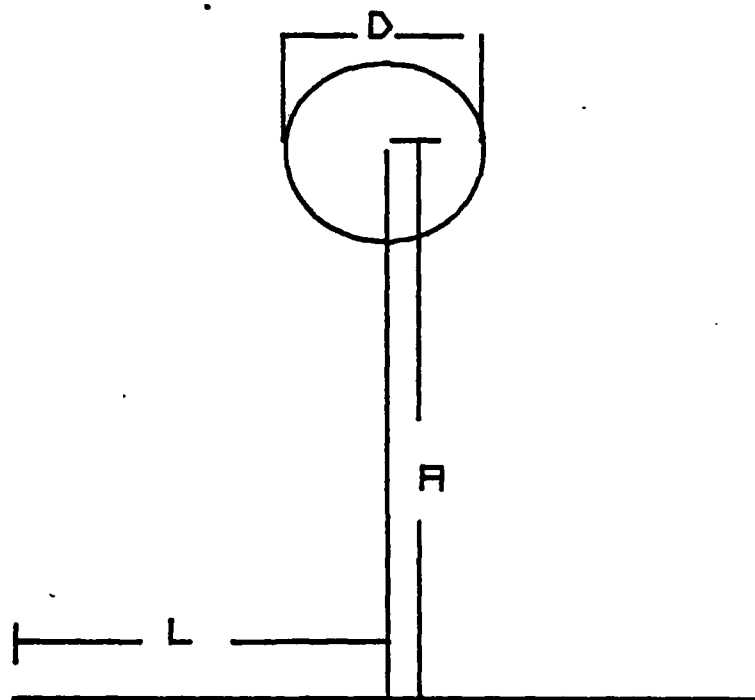
Figure 19.   Radiant Heat Source Design Geometry.
             D = Heat Source Dia., A = Normal Distance to Specimen Surface,
             L = Specimen Half-Width
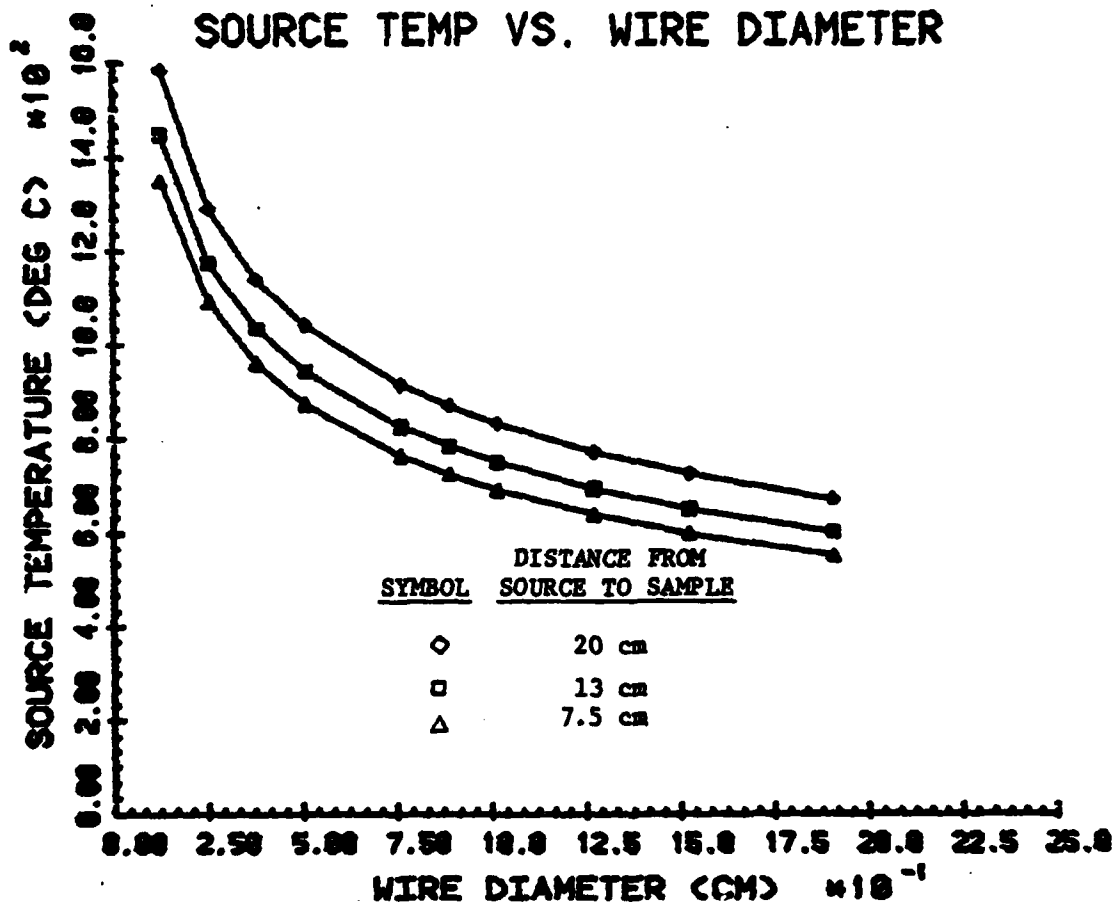
Figure 20. Source Temperature Versus Wire Diameter For Single Source Radiant Heater.
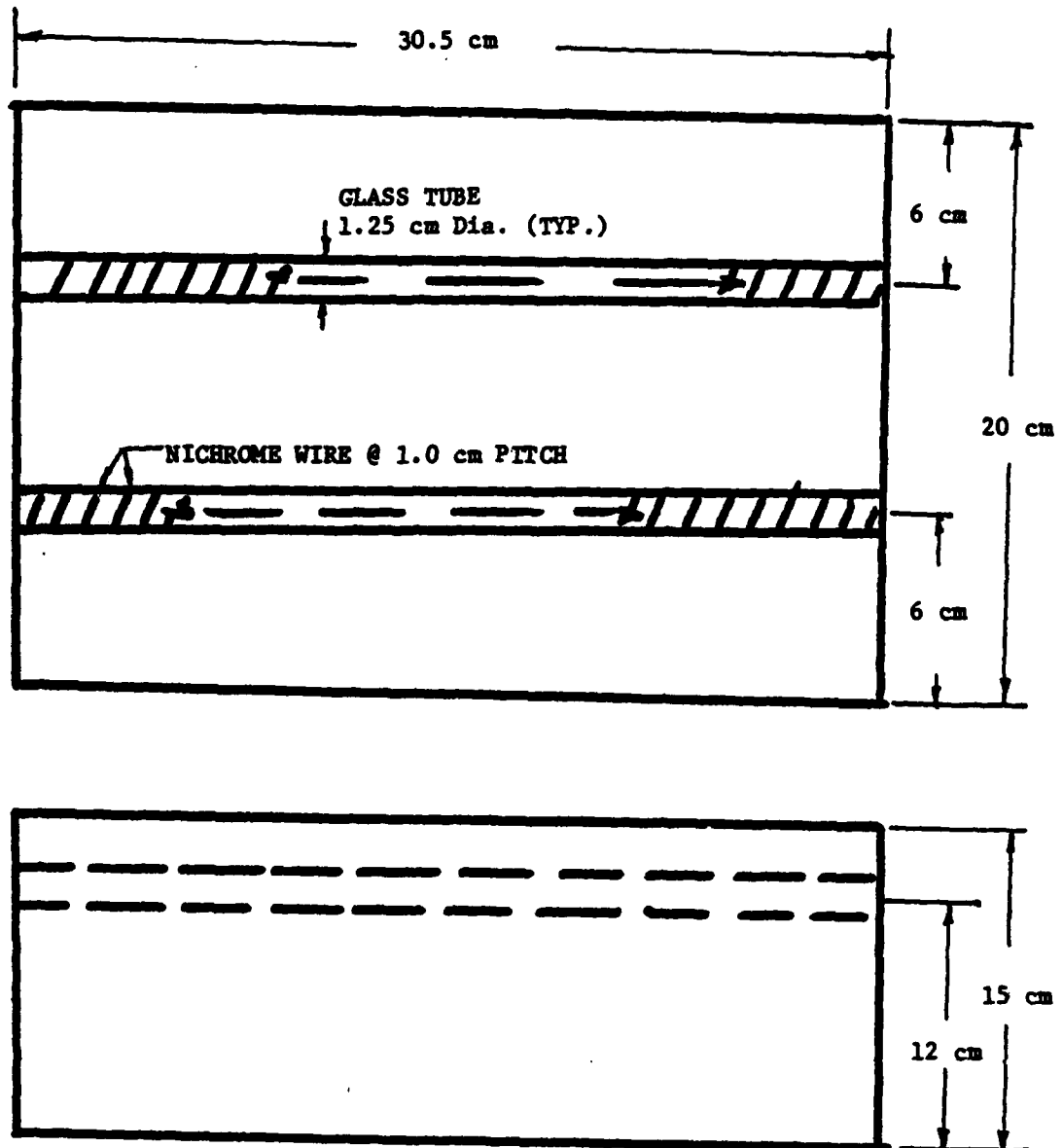
Figure 21. Final Design Geometry For High Powered Heater.

Figure 22. Radiant Heat Source Designed and Built For EATF Studies.
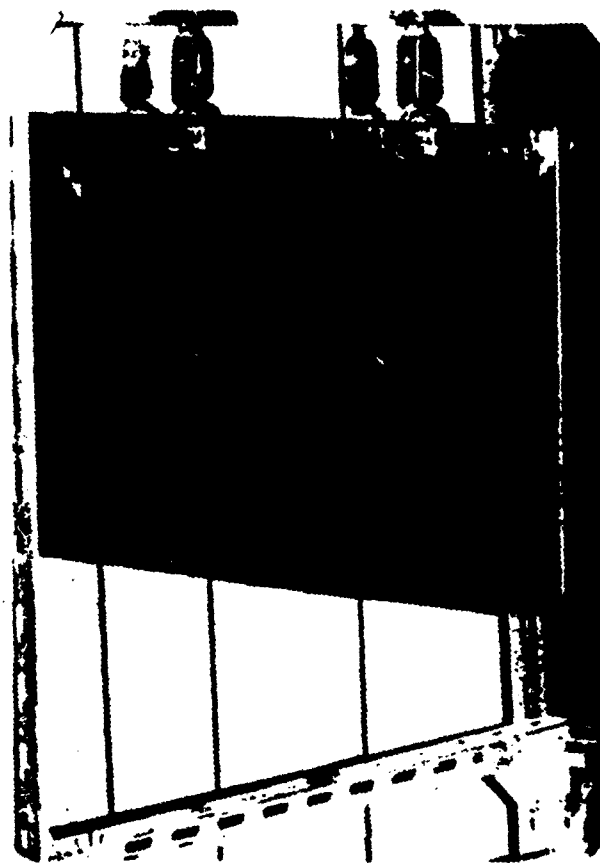
Figure 23. Vertical Mounting Arrangement of Graphite/Epoxy Panel
With Defects.
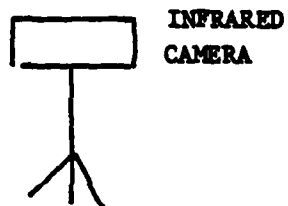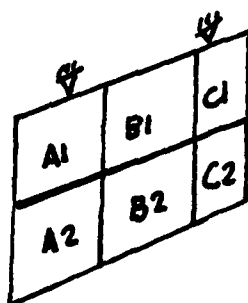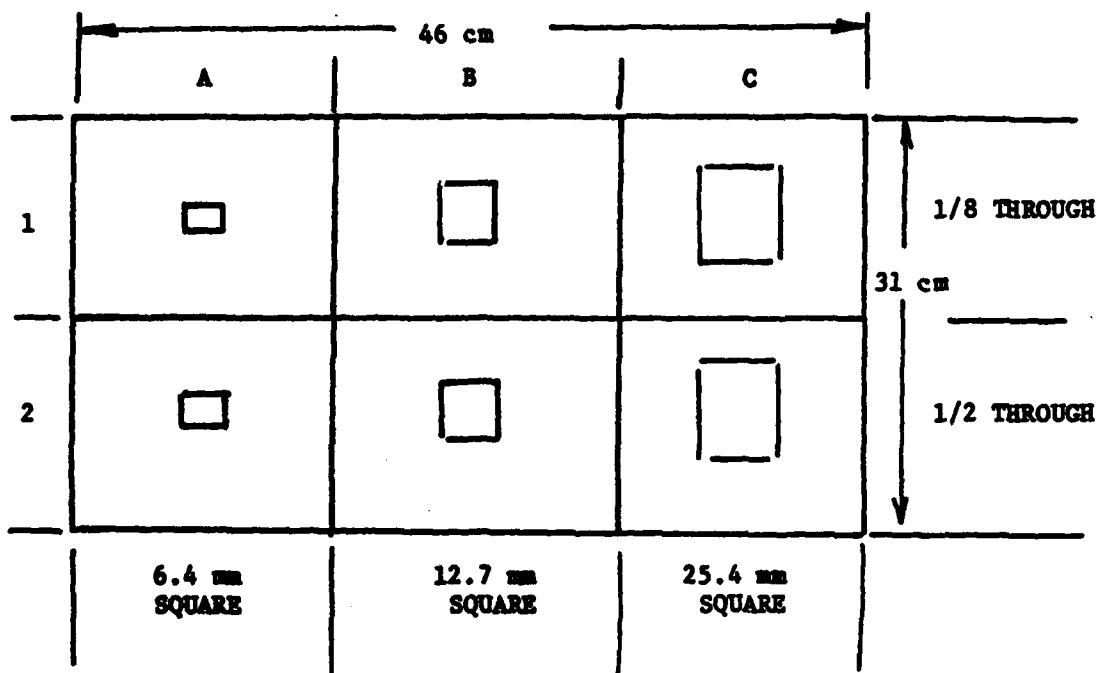
Figure 24. Infrared Camera Arrangement and Gr/Ep Test Panel Flaw Designation.
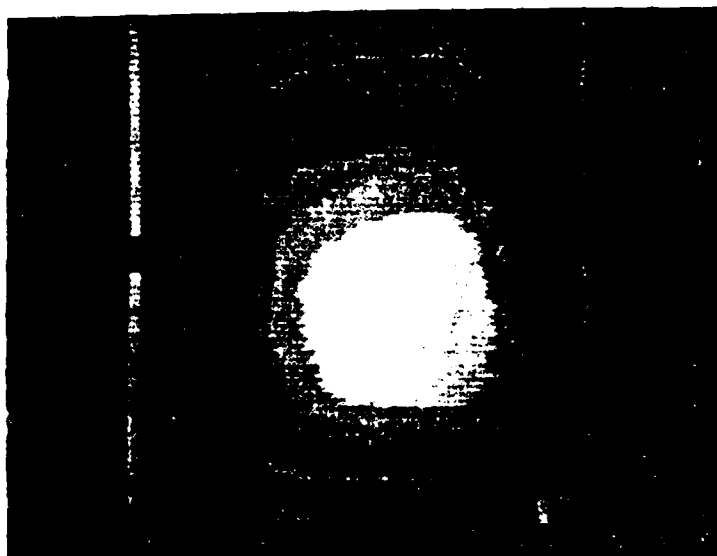
Figure 25.   Thermovideograph of 8-Ply Graphite/Epoxy Panel Containing
Delaminations 1 Ply and 4 Plies Down From the Surface.
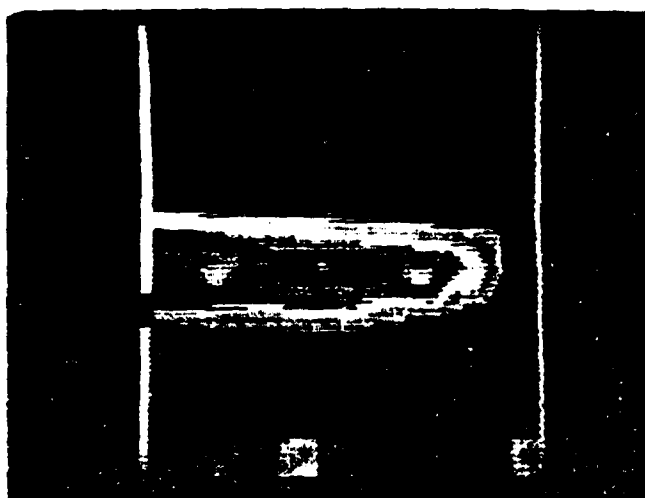
Figure 26. Thermovideograph of Flaws B2 and C2 In 32-Ply Graphite/Epoxy Panel, 60 Seconds After Cooling.
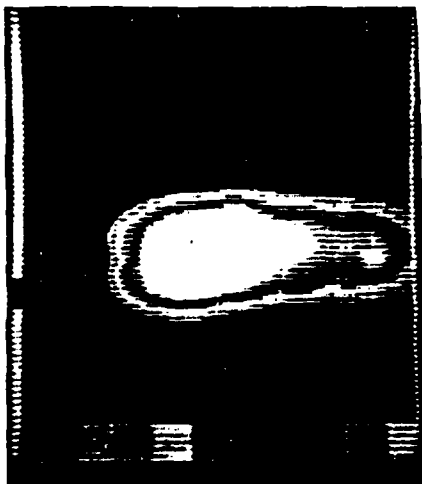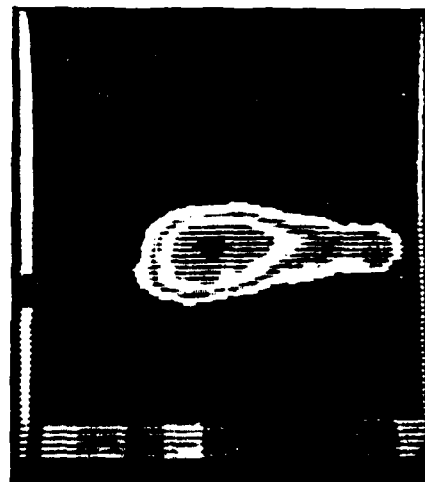
Figure 27.   Thermovideographs of Flaws A2 and B2 In 32-Ply Graphite/Epoxy
Panel.
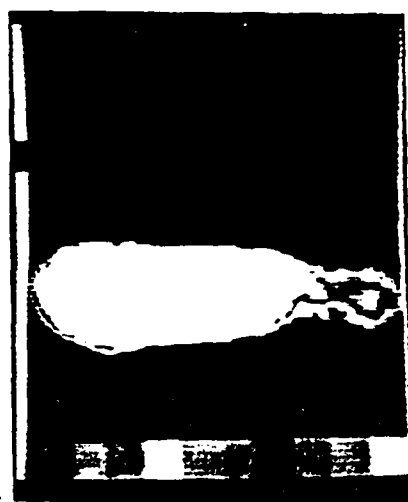
(a)
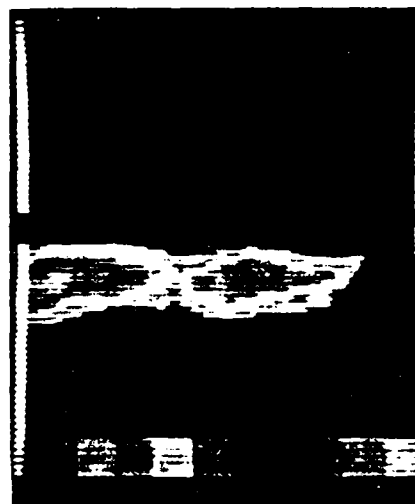
(b)

C2	B2	A2
C1	B1	A1

(c)
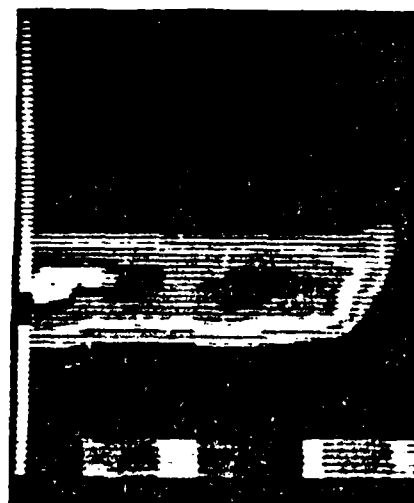
(d)

Figure 28. Thermovideographs of Flaws B1 and C1 Located 4 Plies Down in
32-Ply Graphite/Epoxy Sample. Each Photo Represents An Attempt
At Illuminating Both Flaws Simultaneously.

(a)

(b)

(c)
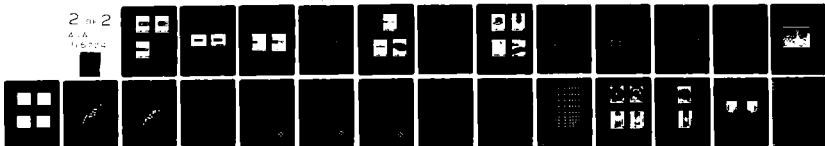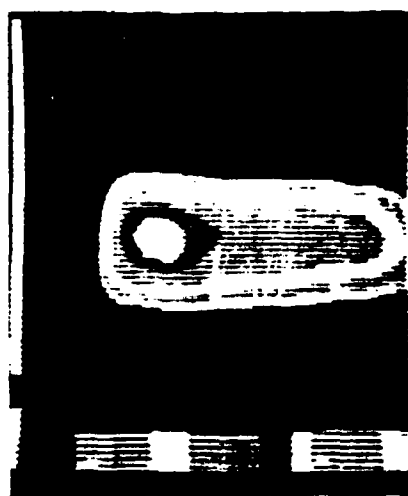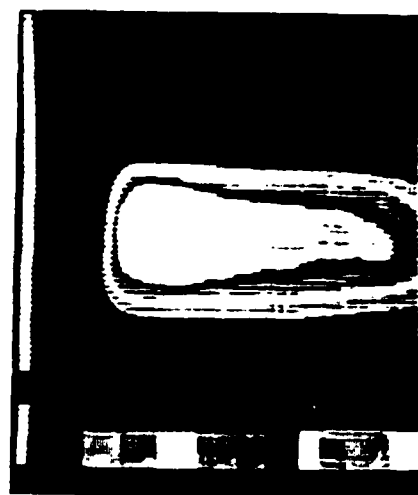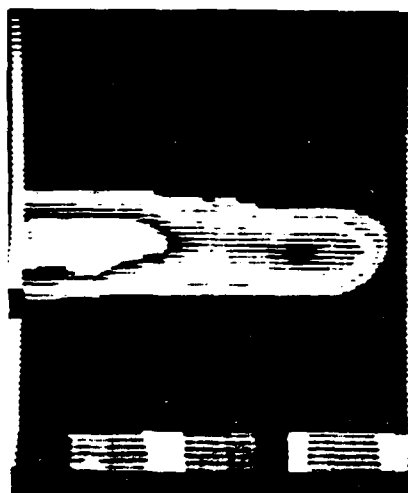
C1	B1	A1
C2	B2	A2

(a) AND (b)

C1	B1	A1
C2	B2	A2

(c)

Figure 29. Thermovideographs of Flaws A2, B2, and C2 Located Half Through 32-Ply Graphite/Epoxy Panel. (a) and (b) Show Flaws C2 (Right) and B2 (Left). (c) Flaws B2 and A2.

A2	B2	C2
A1	B1	C1
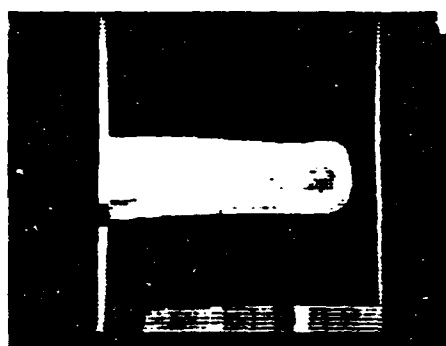
(A)
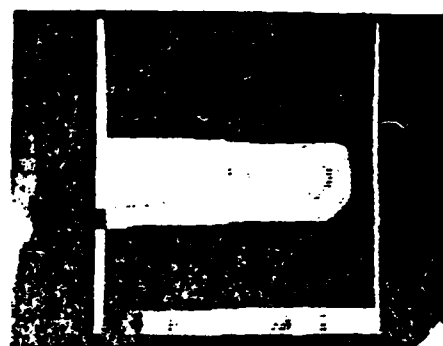
(B)

Figure 30. Thermovideographs of Flaws Al and Cl Located 28 Plies Down in 32-Ply Graphite/Epoxy Panel. (a) and (b) Are Two Different Attempts At Outlining Both Flaws.

94
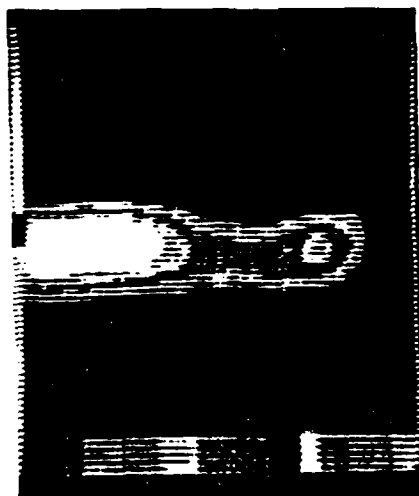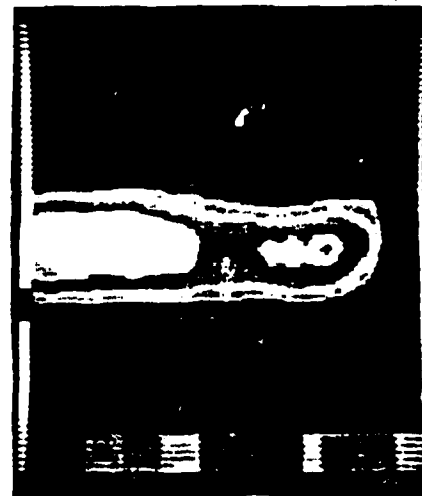
Figure 31.   Thermovideographs of Flaws B1 and C1 Located 28 Plies Down
From Front Surface In 32-Ply Graphite/Epoxy Panel.   (a)
10 deg. C Sensitivity.   (b) 5 deg. C Sensitivity.

NAEC-92-157
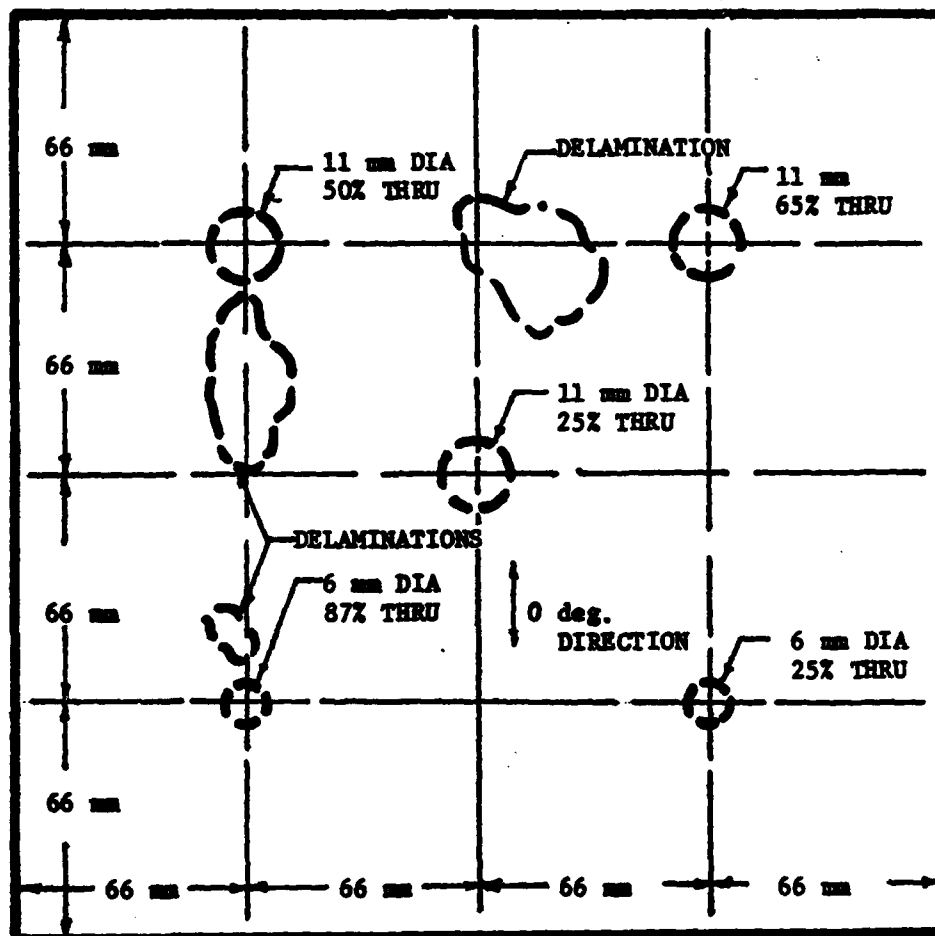
Figure 32.   Defect Map of Anisotropic 32-Ply $[0_2/\pm45]_s$ Gr/Ep Panel
As Seen From Blind Side.

96
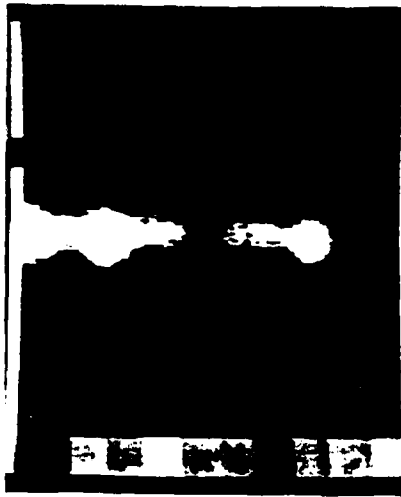
(a) 6mm 87% (LEFT), 11mm 65% (RIGHT)
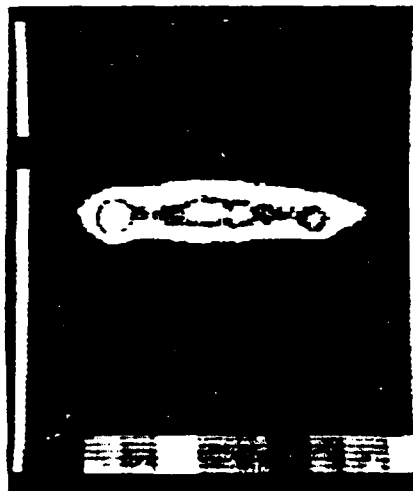
(b) 11mm 65% (LEFT), 11mm 50% (RIGHT)
Delamination (CENTER), 2°C Sens.
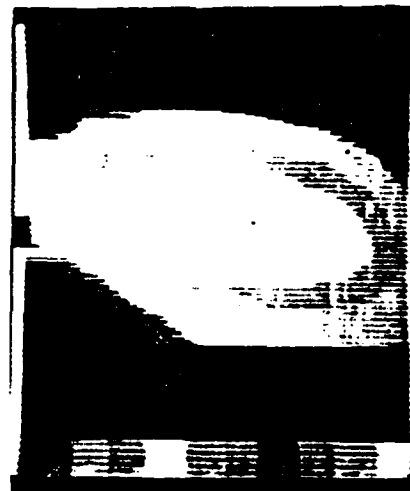
(c) Same as (b), 5°C Sens.

Figure 33. Thermovideographs of Blind Side of Anisotropic $[0_2/\pm45]$ Gr/Ep
Panel With Partial-Through-Holes and Delaminations. Percents
are % Through From Back Side.

97
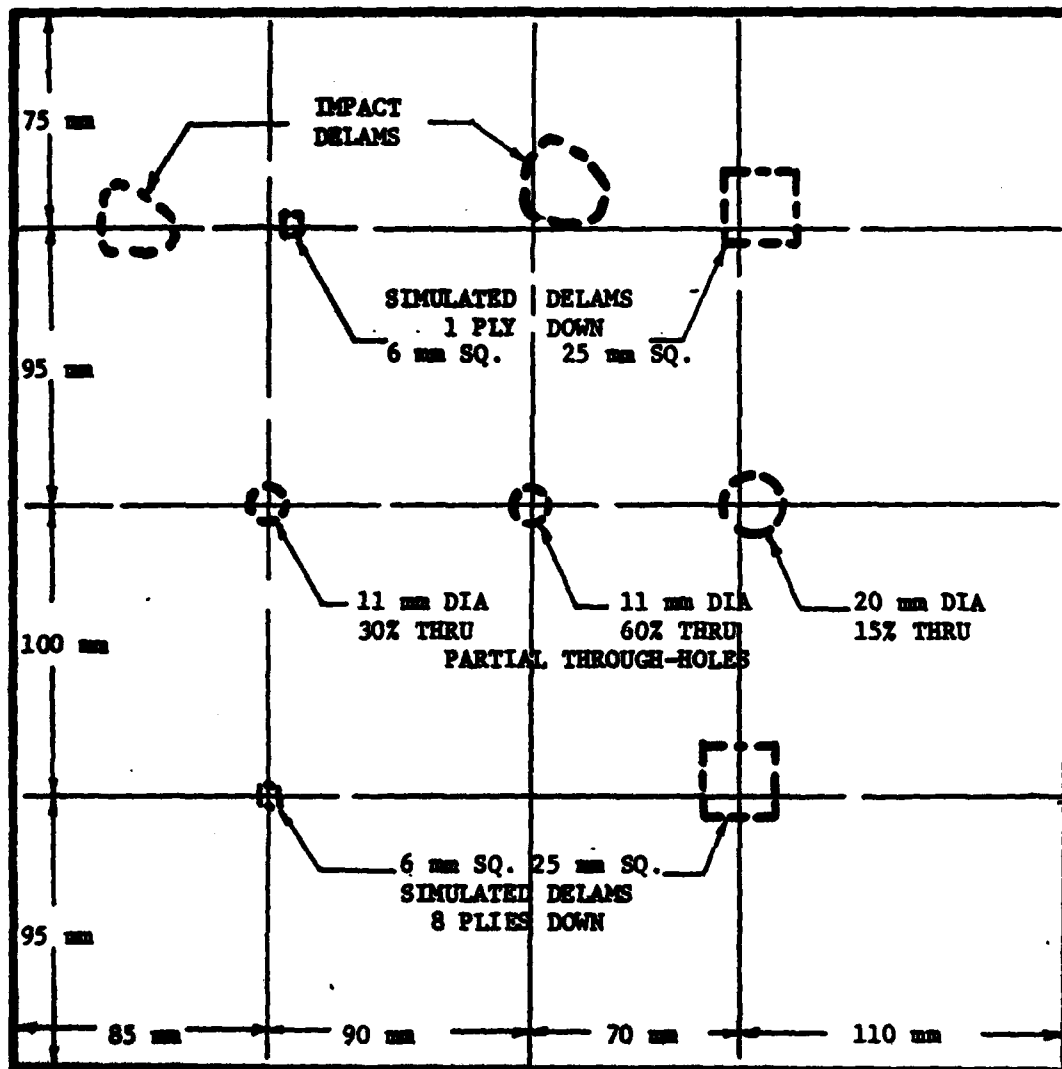
Figure 34. Defect Map of 16-Ply $[0/\pm 45/90]_s$ S2-Glass/Epoxy Panel As Seen From Blind Side.

(a) 20mm 15% (LEFT), 11mm 60% (RIGHT)   (b) Same as (a) but COOLED 360s.
25mm DELAM, 1 Ply Down (LOWER L.);
HEATED 20s., COOLED 10s.
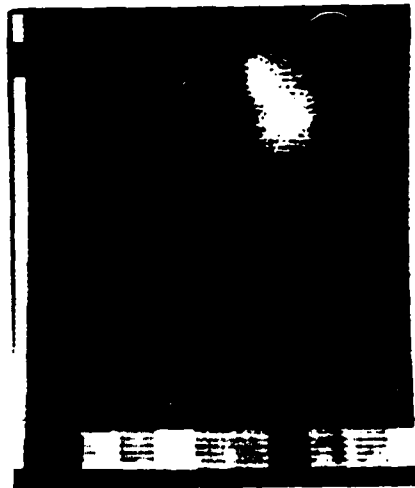
(c) 25mm DELAM, HALF THRU,   (d) LEFT-TO-RIGHT: 20mm 15%,
HEATED 30s., COOLED 10s.   11mm 60%, 11mm 30% PTH,
HEATED 10s., COOLED 10s.

Figure 35. Thermovideograph of Partial-Through-Holes (PTH) and Delaminations
(DELAM) in 16-Ply [0/±45/90]$_s$ S2-Glass/Epoxy Panel. Percentages
are % Through From Back Surface.
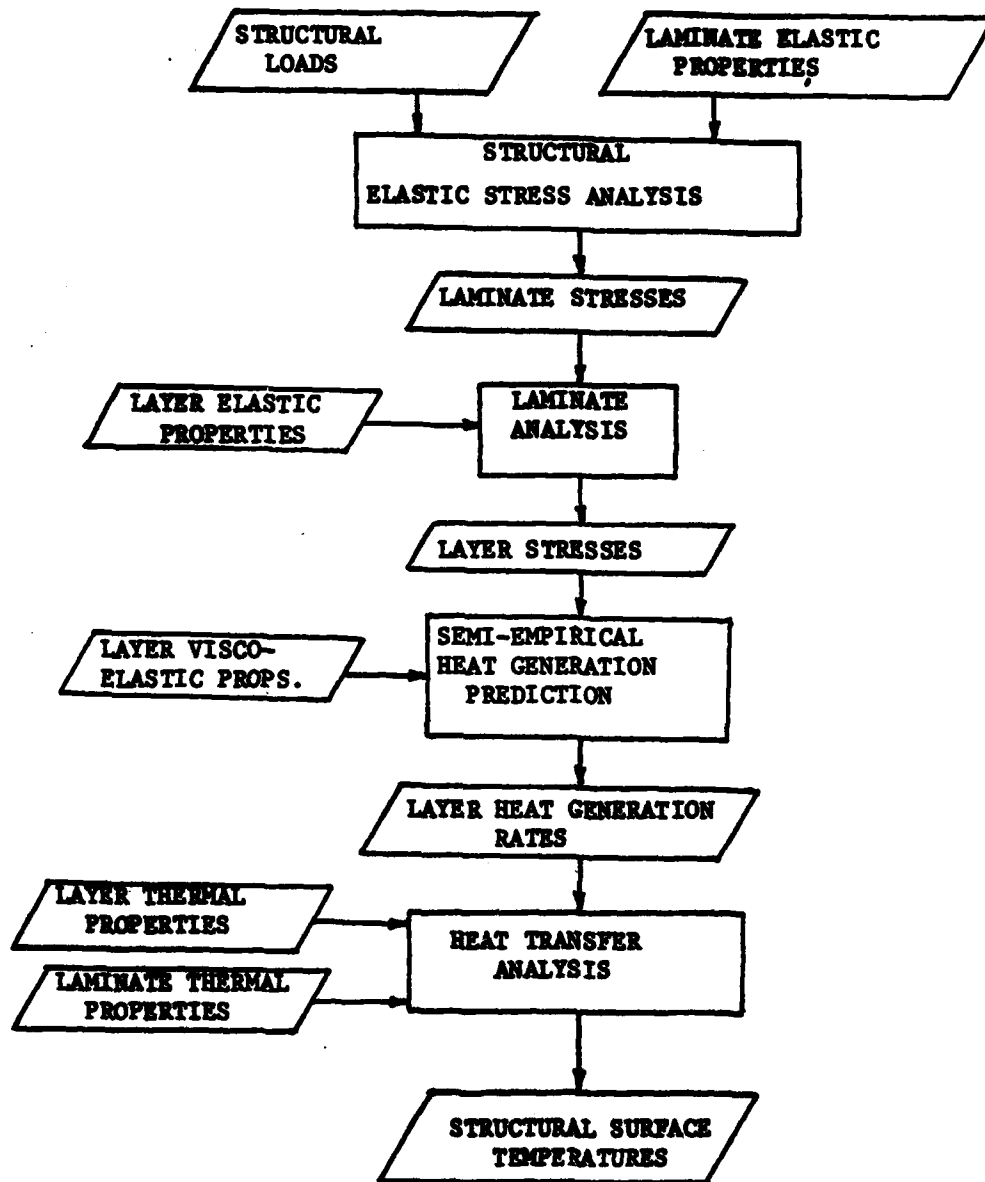
Figure 36. Procedure For Calculating The Temperature Distribution In A
Composite Laminated Structure Under Cyclic Loading.
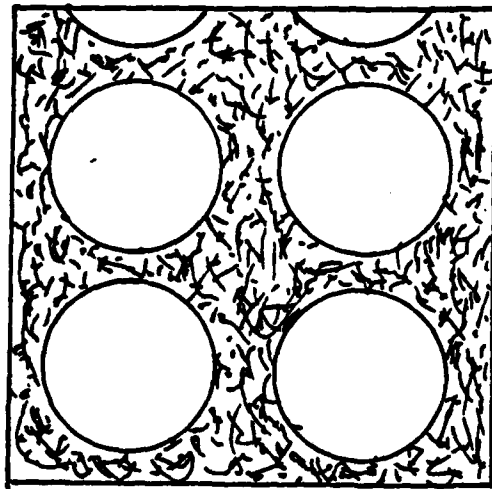
(a) RECTANGULAR ARRAY
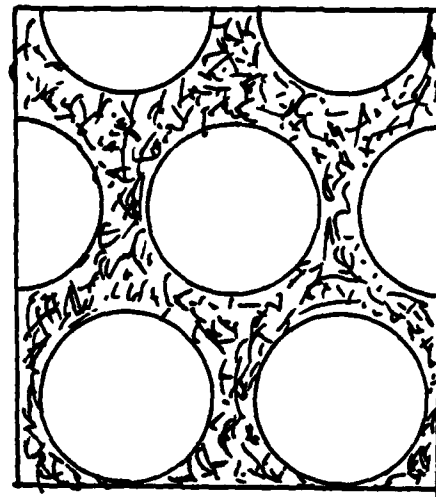
(b) HEXAGONAL ARRAY
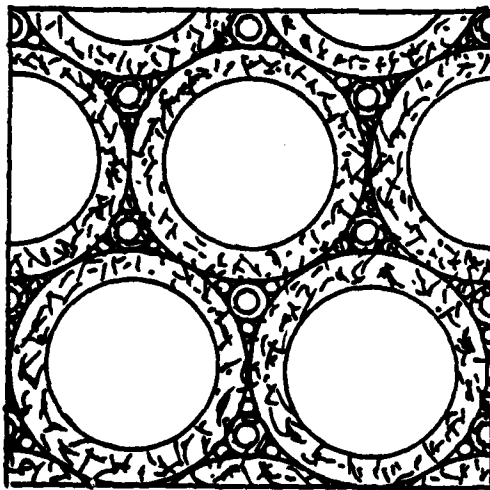
(c) COMPOSITE CYLINDER ASSEMBLAGE
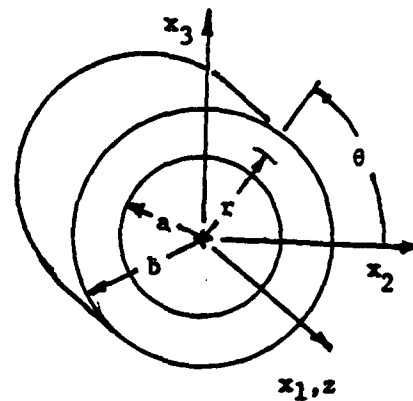
(d) COMPOSITE CYLINDER GEOMETRY AND POLAR COORDINATE SYSTEM

KEY FOR (a),(b),(c): ○ ← FIBER   MATRIX ← ▨

Figure 37. Deterministic Phase Geometries For Unidirectional Fiber Composites.

NAEC-92-157
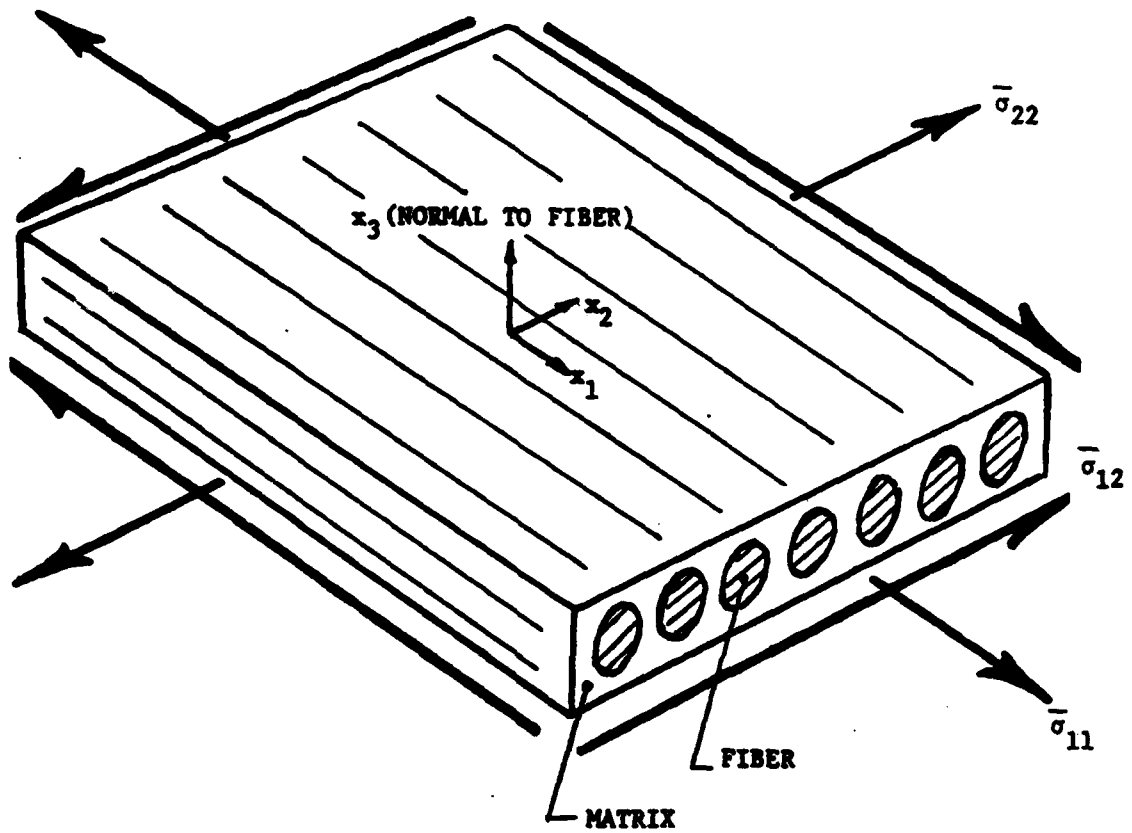
Figure 38.   Unidirectional Fiber Composite Coordinate System and
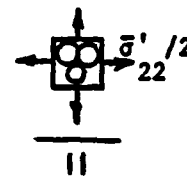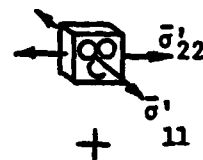Average Layer Stresses.

102

(a) TRANSVERSE SHEAR
    (UPPER BOUND)

$\bar{\sigma}'_{22}/2$

(b) XFORM TO AXES
    @ $\pi/4$:

$\bar{\sigma}'_{22}/2$

$\bar{\sigma}'_{22}/2$

+
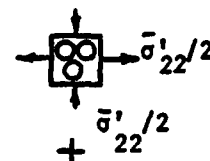
(c) ADD PLANE ISOTROPIC STRAINING:

$\bar{\sigma}'_{22}/2$

||

(d) GET PLANE TRANSV. STRAINING:

$\bar{\sigma}'_{22}$

σ'_{11}

+

(e) ADD AXIAL COMPR. STRAINING:

$\bar{\sigma}'_{11}$

||

(f) TRANSVERSE NORMAL STRESS:

$\bar{\sigma}_{22}$

Figure 39. Method of Determining Phase Stresses Due to Layer
           Transverse Normal Stress Using Superposition of
           Transverse Shear, Plane Isotropic Straining, and
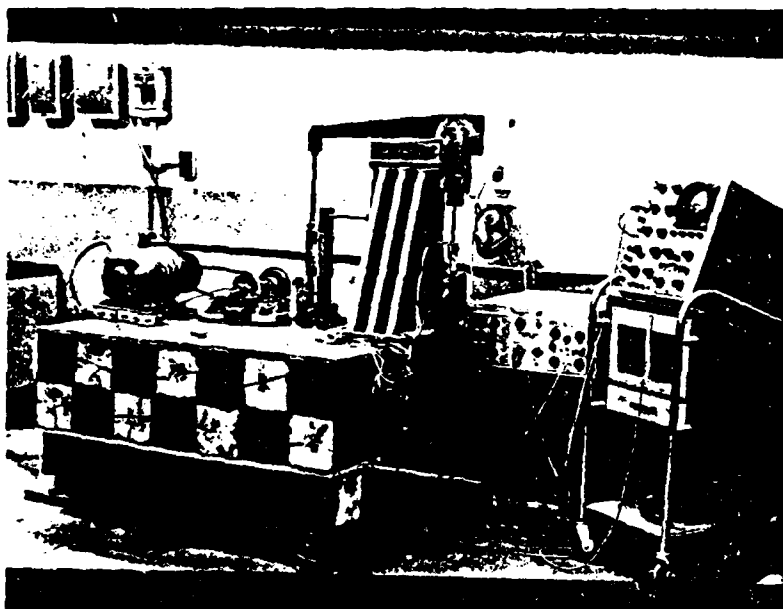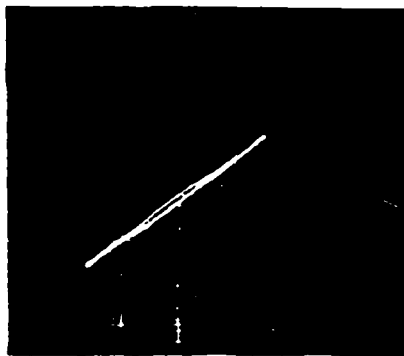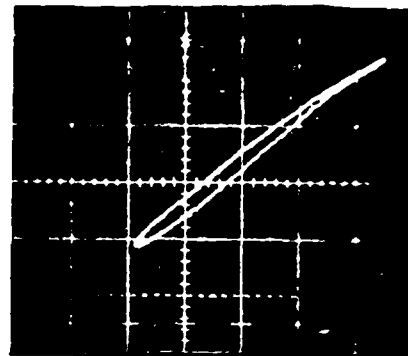   Axial Compressive Straining.

103

Figure 40. Stress-Generated Thermal Field Test Apparatus.

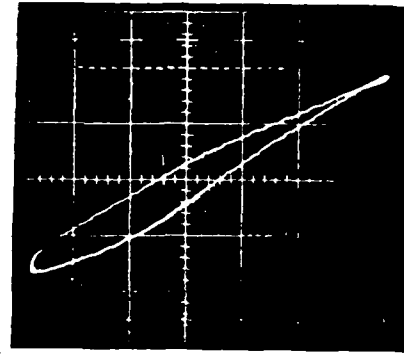$\omega = 28\text{Hz},\ \sigma_x{}^o = 7.84\text{MPa}$ $\omega = 57.5\text{Hz},\ \sigma_x{}^o = 11.94\text{MPa}$

(a) [±45] S2-Glass/Epoxy

$\omega = 28\text{Hz},\ \sigma_x{}^o = 9.50\text{MPa}$ $\omega = 57.5\text{Hz},\ \sigma_x{}^o = 12.22\text{MPa}$

(b) [±45] Graphite/Epoxy

Figure 41.   Typical Hysteresis Loops Obtained During Energy Dissipation Calibration Tests of Graphite/Epoxy and S2-Glass/Epoxy Composites.
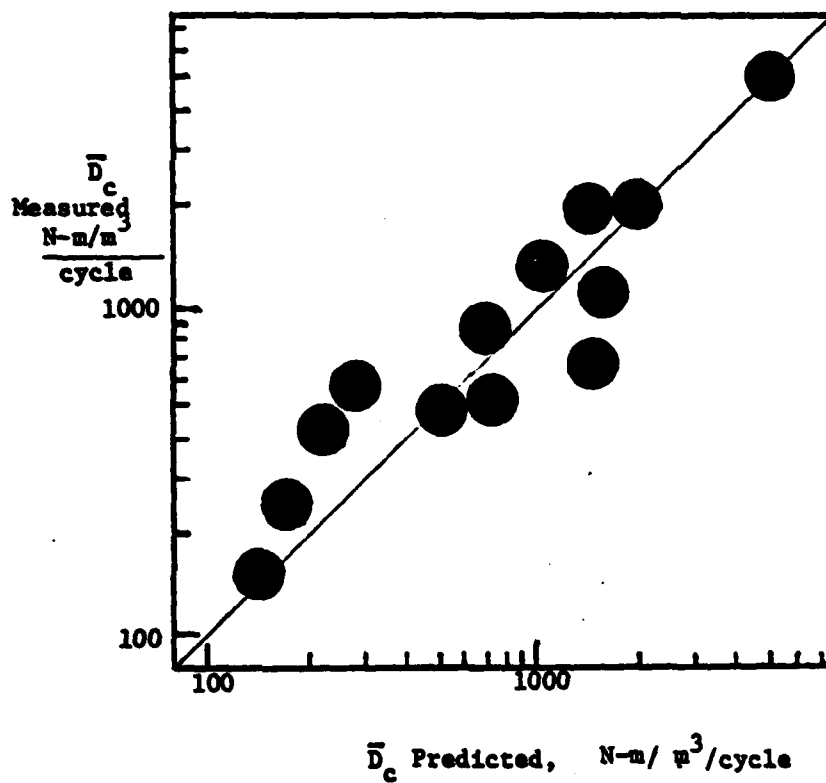
Figure 42. Energy Dissipated per Cycle - Celion 6000/Narmco 5213
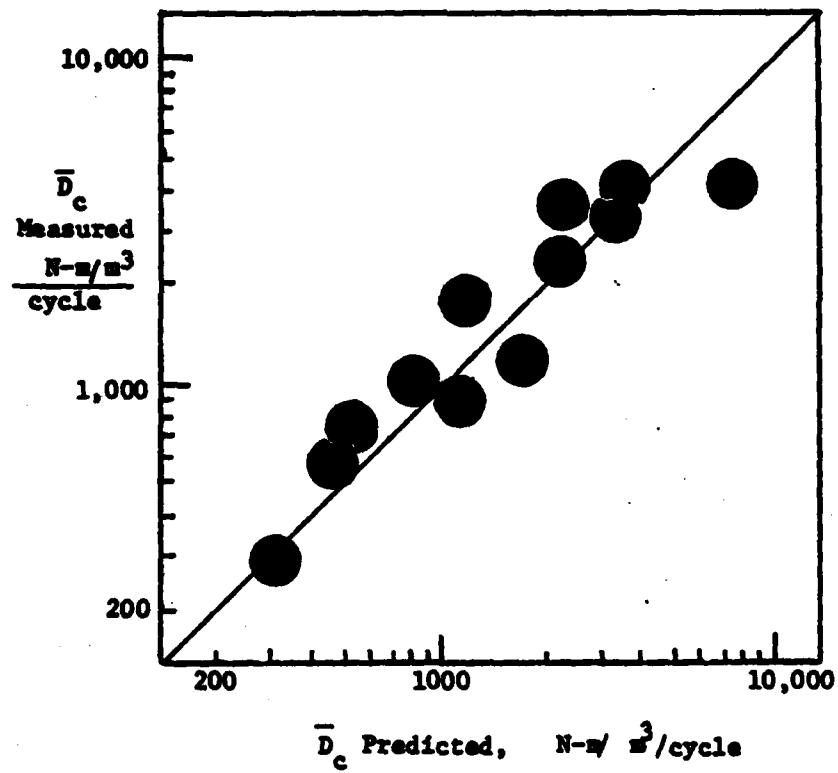Graphite/Epoxy Composite

Figure 43. Energy Dissipated per Cycle - 3M SP-250-S2 S2-Glass/
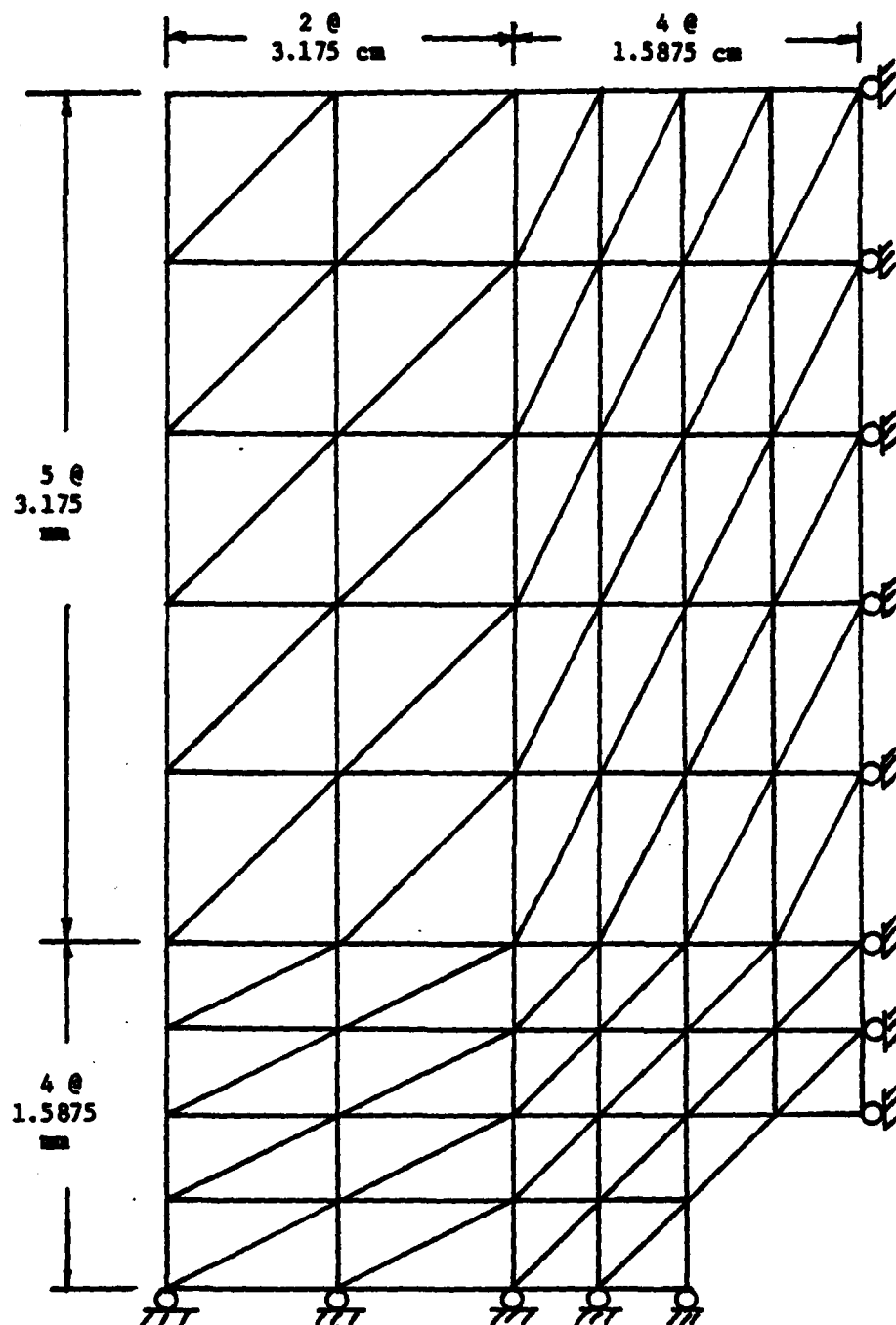Epoxy Composite

Figure 44. Finite Element Grid For 25.4-mm-Wide Sample Containing
6.35-mm-Dia Through-Hole. Only One Quarter of Specimen
Is Needed Due to Double Symmetry.

1 MPa

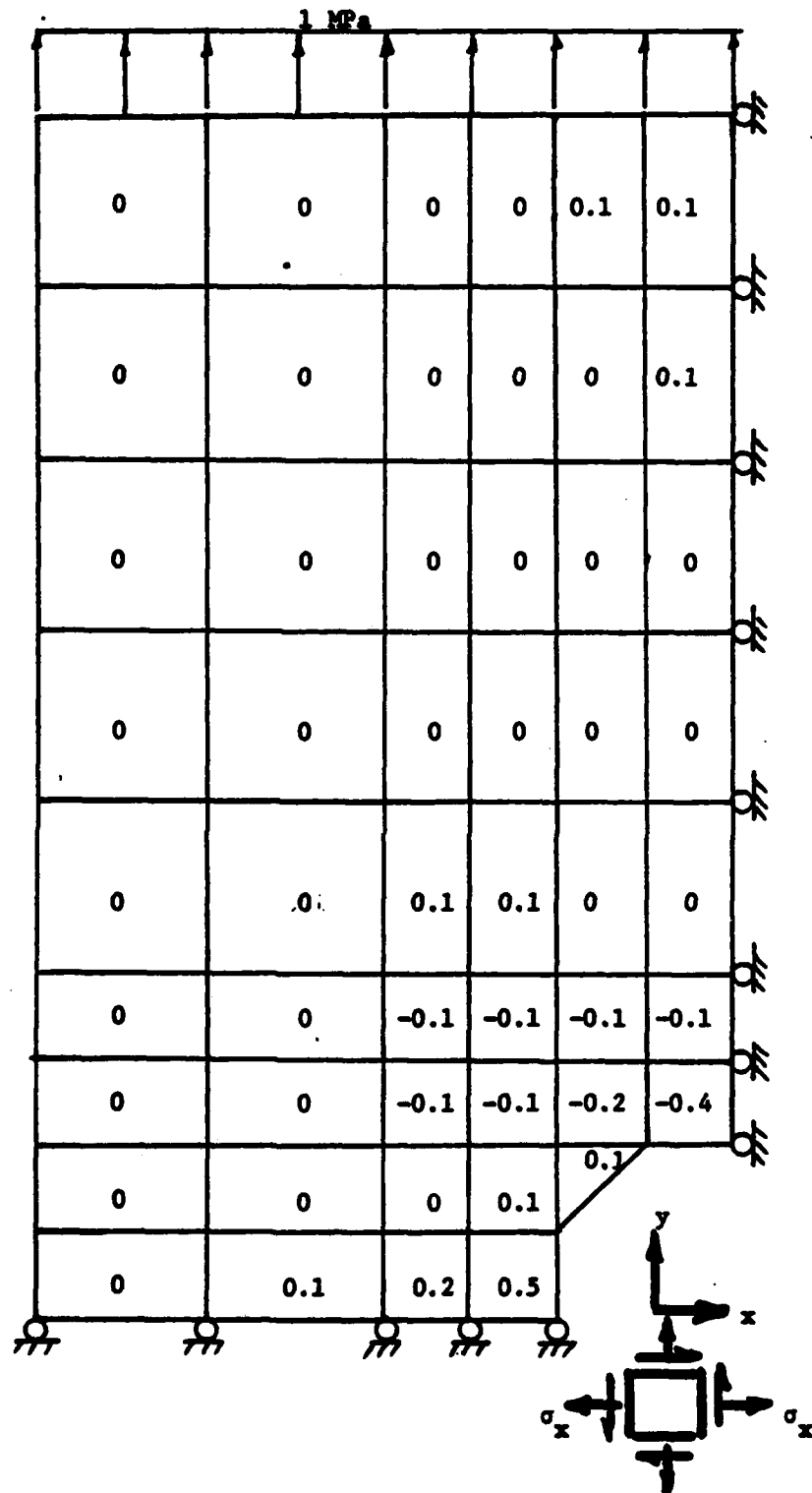| 0 | 0 | 0 | 0 | 0.1 | 0.1 |
0	0	0	0	0	0.1
0	0	0	0	0	0
0	0	0	0	0	0
0	.0	0.1	0.1	0	0
0	0	-0.1	-0.1	-0.1	-0.1
0	0	-0.1	-0.1	-0.2	-0.4
0	0	0	0.1	0.1	
0	0.1	0.2	0.5		

σ_x σ_x

Figure 45a. Finite Element Results - Horizontal Normal Stress, σ_x All Stresses in MPa.
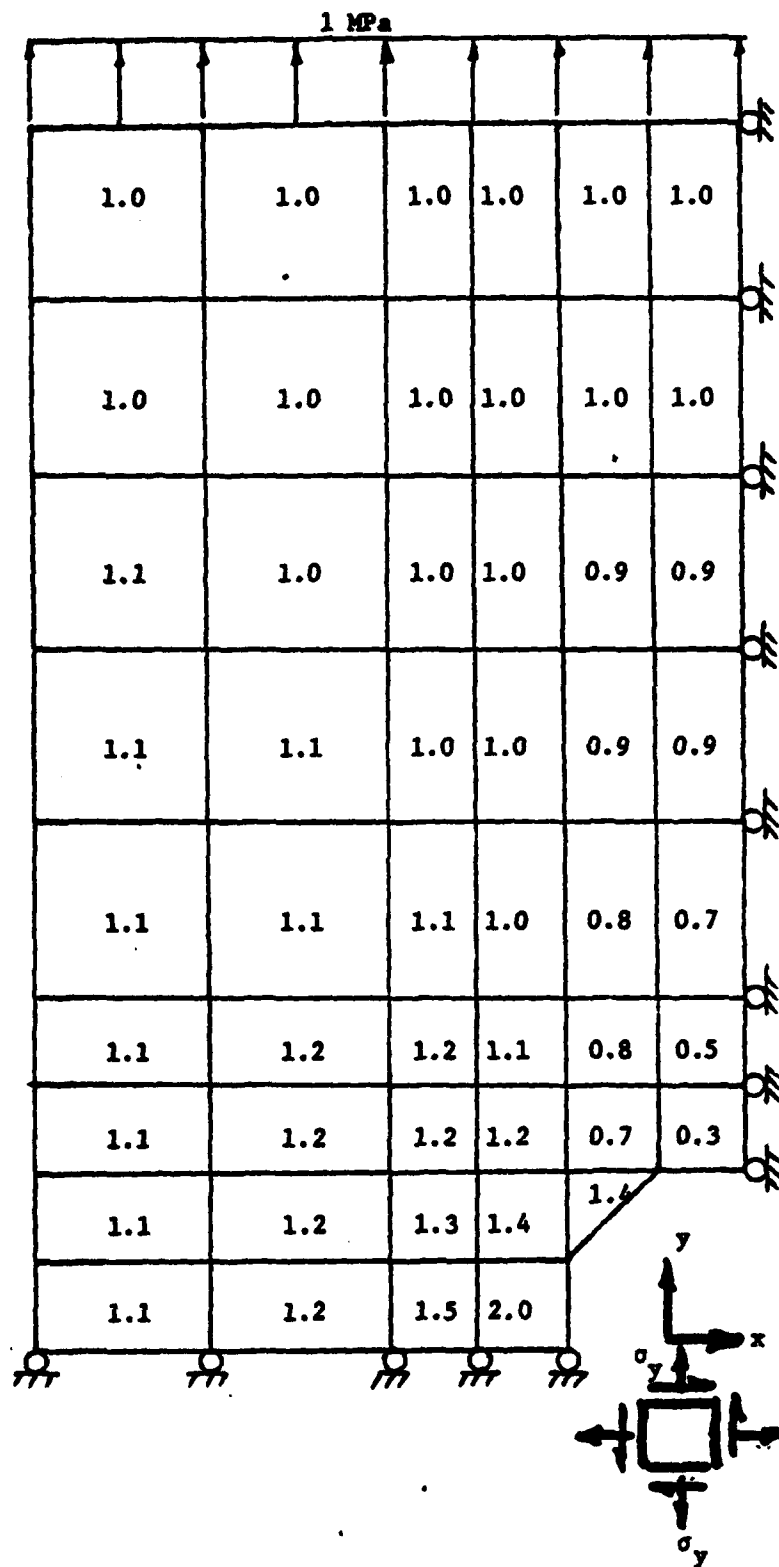
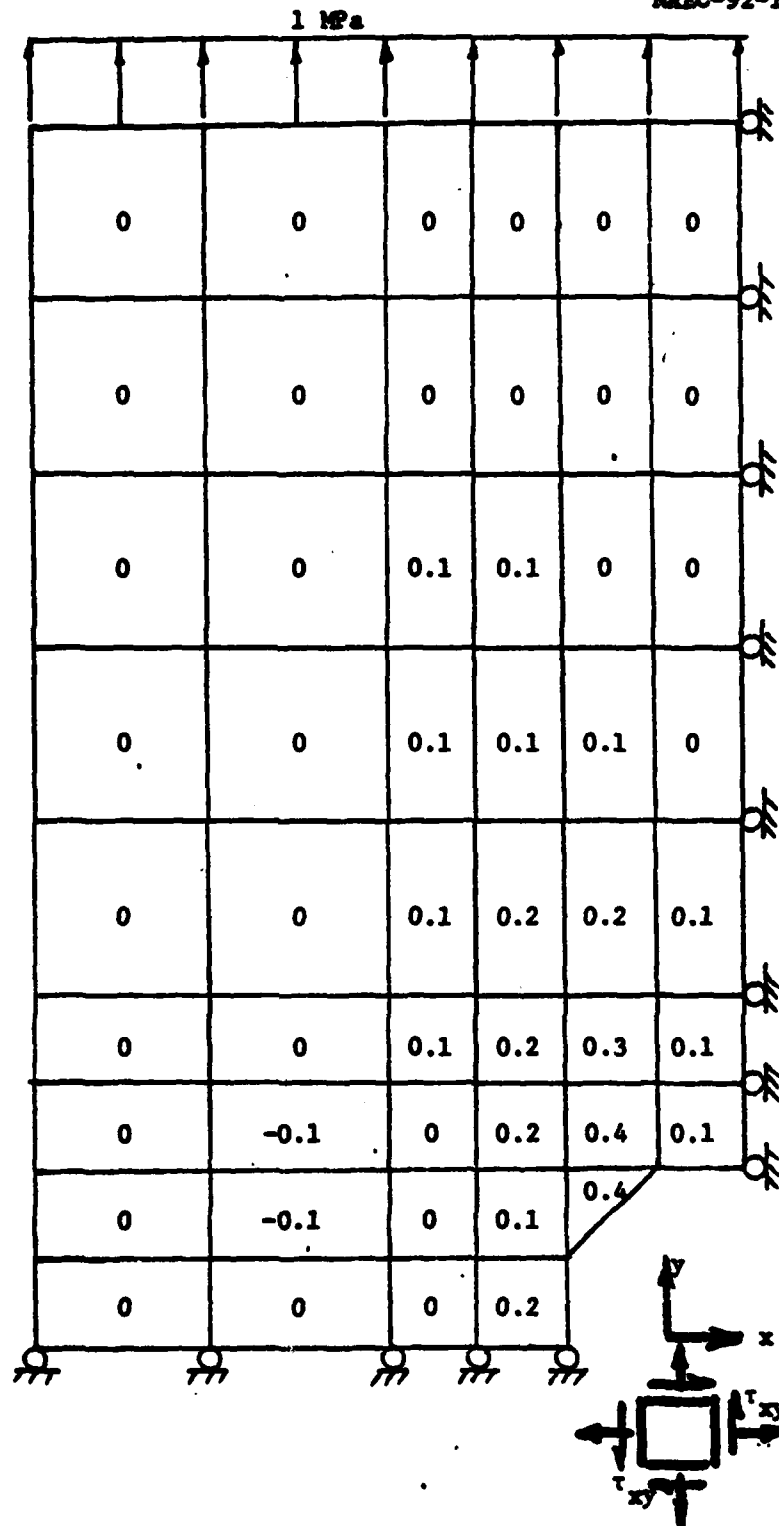Figure 45b. Finite Element Results - Vertical Normal Stress, σ_y
All Stresses in MPa.

1 MPa

0	0	0	0	0	0
0	0	0	0	0	0
0	0	0.1	0.1	0	0
0	0	0.1	0.1	0.1	0
0	0	0.1	0.2	0.2	0.1
0	0	0.1	0.2	0.3	0.1
0	-0.1	0	0.2	0.4	0.1
0	-0.1	0	0.1	0.4	
0	0	0	0.2		

y

x

τ_{xy}

τ_{xy}

Figure 45c.   Finite Element Results - Shear Stress, τ_{xy}
All Stresses In MPa.

111

Figure 46a. Heating Rate Density Analysis Results For Graphite/Epoxy kW/m^3.

17.1	17.1	17.1	17.1	15.2	15.2
17.1	17.1	17.1	17.1	17.1	15.2
20.7	17.1	17.1	16.0	13.8	13.8
20.7	20.7	18.2	16.3	14.1	13.8
20.7	20.7	20.9	18.5	13.8	9.1
20.7	24.8	24.8	22.9	16.0	5.5
20.7	24.0	27.8	27.0	17.9	6.1
20.7	24.5	29.8	32.5	38.6	
20.7	23.4	32.5	60.1		

Figure 46b. Heating Rate Density Analysis Results For S2-Glass/Epoxy kW/m³.

INSULATED

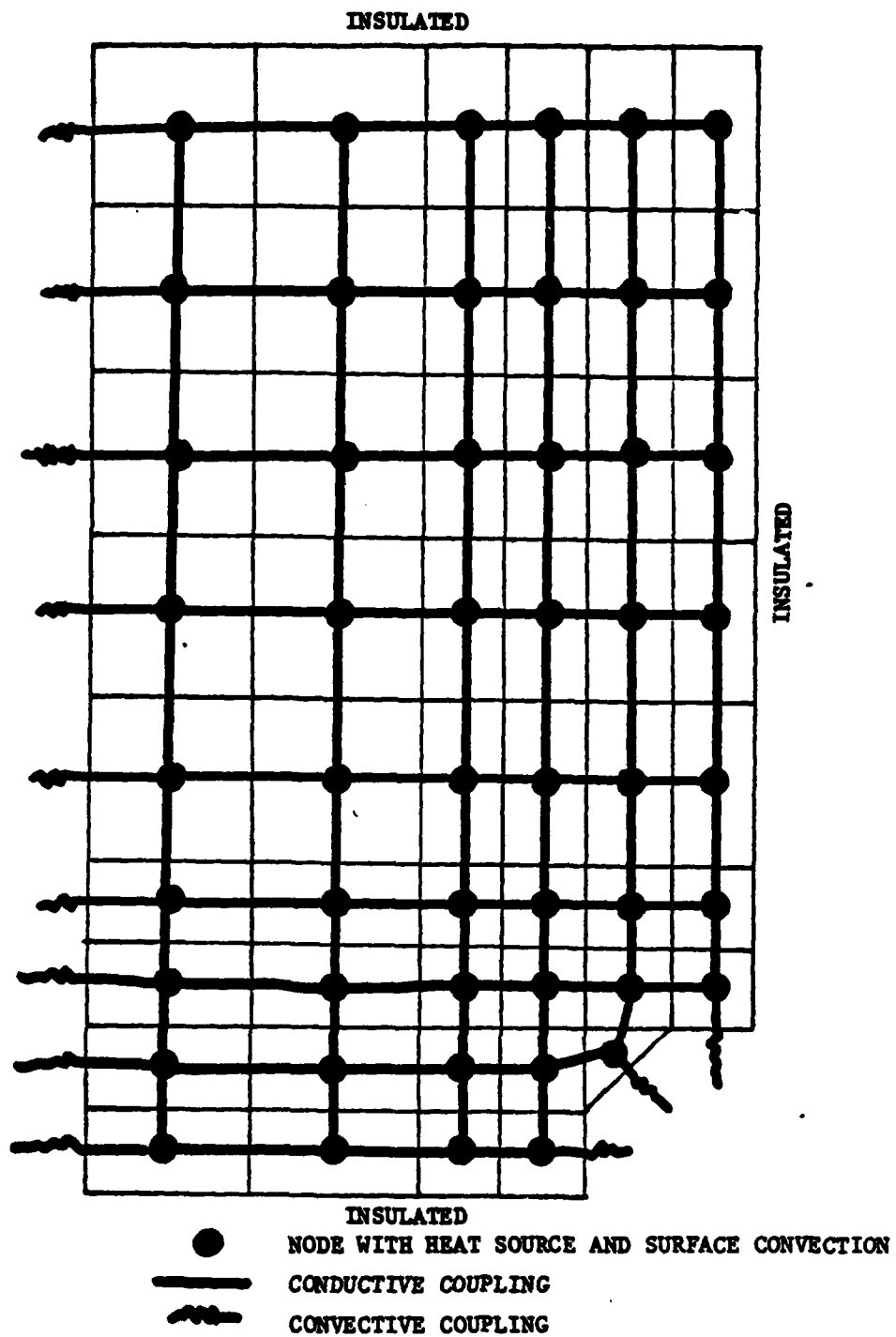NODE WITH HEAT SOURCE AND SURFACE CONVECTION
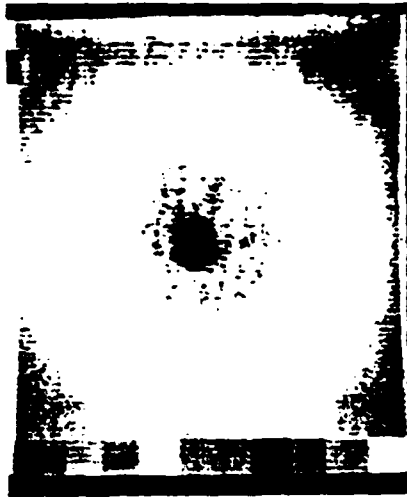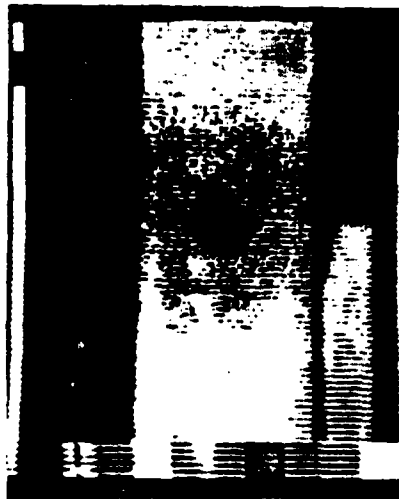
CONDUCTIVE COUPLING

CONVECTIVE COUPLING

Figure 47. Nodal Pattern Used In Numerical Heat Transfer Analysis of Cycled Gr/Ep and S2-G1/Ep Samples.

114

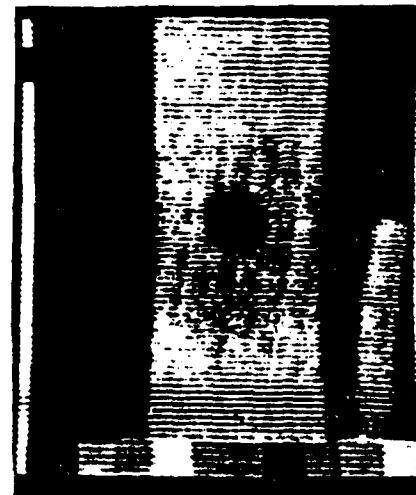(a) S2-Glass/Epoxy - No Cycles   (b) S2-Glass/Epoxy @ 30 min.

(a) Graphite/Epoxy - No Cycles   (b) Graphite/Epoxy @ 30 min.

Figure 48. Thermovideographs of [0/±45/90] Composite Specimens With 6-mm Through-Hole Under Cyclic Tension.

(a) S2-Glass/Epoxy

(b) Graphite/Epoxy

Figure 49. Thermovideographs of [0/±45/90] Composite Specimens
Containing Through-Holes and Delaminations Under Cyclic
Tension.

Before Axial Split   After Axial Split

Figure 50.   Thermovideographs of [0] Graphite/Epoxy Sample Under
             Cyclic Tension Showing Frictional Heat.

117

DISTRIBUTION LIST

NAVAIRENGCEN

1114 (2)
1115
92A3 (20)
92A1C
92A4
92713
91B1
9011

NAVAIRDEVCEN 60633 (2)
NAVAIRPROPCEN PE43
AFML/LLP
AMMRC DRXMR-MQ
NASA LANGLEY MS188E
NAVSHIP R&D CENTER (2803)

NAVAIRSYSCOM

AIR-340E (3)
AIR-552B
AIR-5523 (3)
AIR-4114 (2)
AIR-5203 (2)
AIR-00D4 (2)
AIR-55132A

DTIC (12)

REVISION LIST

REVISION	PAGES AFFECTED	DATE OF REVISION